Papers from
the

SUMMER UNDERGRADUATE RESEARCH FELLOWSHIP PROGRAM IN OCEANOGRAPHY

at

THE UNIVERSITY OF RHODE ISLAND
Graduate School of Oceanography
and
Department of Ocean Engineering

NARRAGANSETT, RHODE ISLAND

June - August 2002

This program was funded by Grant OCE-9912236 from the National Science Foundation.

GSO Technical Report No. 2003-1

PARTICIPANTS IN THE 2002 SUMMER UNDERGRADUATE RESEARCH FELLOWSHIP PROGRAM IN OCEANOGRAPHY

FELLOWS

Mark Barthelemy	University of New Orleans, New Orleans. LA
John Blum	University of Michigan, Ann Arbor, MI
Jason Breves	Roger Williams University, Bristol, RI
Jennifer Dionne	Washington University, St. Louis, MO
Bethany Marsh	Colorado College, Colorado Springs, CO
Andrea Mullen	University of Akron, Akron, OH
Jeffrey Gall	Cornell University, Ithaca, NY
Emily Grason	Bowdoin College, Brunswick, ME
John Malkovich	Gustavus Adolphus College, St. Peter, MN
Johanna Mathieu	Massachusetts Institute Technology, Cambridge, MA
Brian Sullivan	Westminster College, New Wilmington, PA

ADVISORS

Peter Cornillon
Kathryn Ford
Isaac Ginis
Alfred Hanson
Tetsu Hara
John King
Lucie Maranda
Robert Pockalny
Yang Shen
Jennifer Specker
David Ullman

MENTORS

William DeLeo
Peter Egli
Clifford Heil
Anthony Kirincich
Qingtao Song
Michael Sutherland
Biju Thomas
Phil Veillette
Rich Viso
Ting Yang

PROGRAM ASSISTANTS

Kelly Kriner, Kim Carey & Rhonda Kenny

PREFACE

This report presents the papers written by the nine of eleven participants in the 2002 Summer Undergraduate Research Fellowships in Oceanography (SURFO) program at the Graduate School of Oceanography (GSO), University of Rhode Island (URI). This past summer represented the 17th year in which the program has been coordinated and extended through the several disciplines in oceanography and ocean engineering at URI's Narragansett Bay Campus. The 2002 program was arguably one of the most successful in recent history with at least two students publishing their work in nationally recognized refereed journals. In addition, 4 of the students presented their work at national meetings, including Fall AGU, ASLO and GSA. The ASLO presentation received the outstanding REU paper at the meeting in Salt Lake City, Utah.

During the fall of 2001 advertisements were sent to physics, chemistry, biology and geology departments, including faculty advisors at a number of minority colleges. Letters announcing the program were sent to all Society of Physics Students and college advisors. Flyers and overheads were provided to colleagues presenting invited talks at various undergraduate institutions. The SURFO web site has continued to be updated and more useful links describing possible research programs at GSO/URI have been added. We received 78 applications for the program, and about two-thirds of these applicants used the electronic application form. This trend of increasing electronic applications has continued since the SURFO web site was initially established in 1997. Ten students were selected for the program with a breakdown by oceanographic discipline as follows: 4 Geological, 4 Physical, 2 Chemical, 1 Biological. For the first time in over ten years, the number of male participants (7) outnumbered the number of female participants (4). One of these participants was also from an underrepresented group.

The program began with an orientation session and a tour of the GSO campus and facilities. For the 11 weeks of the summer program, each fellow worked on a research project under the supervision of a faculty mentor and a graduate student mentor. The range of research included: 1) instrument development for chemical analysis of seawater; 2) numerical and physical modeling of hurricane-ocean interactions, ocean front development, and near-surface turbulence; 3) analyses of sediment geochemistry, lacustrine paleomagnetics, seismic waveform, and estuarine plankton; and 4) development of a methods to quantify the physiological response of native species to invasive species.

Fellows attended a total of 18 biweekly seminars (1-1.5 hour-long) during which faculty members and local environmental entrepeneurs gave informal presentations on a range of oceanographic disciplines. These presentations ranged from basic oceanographic topics to new and evolving fields of oceanography. We also offered lectures on scientific writing and how to create effective oral and poster presentations. We continued an informal round-table meeting with several faculty members, graduate students and SURFOs to discuss how to get into graduate school and what will be expected of them. We also instituted a similar round-table format to discuss possible careers in oceanography. Our exit questionnaires revealed that students found these seminars interesting and very useful, and the exposure to a wide range of disciplines/research topics helped students identify additional areas of interest. Other undergraduates (NOT affiliated with the SURFO program) working at EPA or NOAA labs on the Bay Campus and even graduate students at GSO also attend many of these seminars.

Finally, in addition to preparing their written reports, each SURFO gave a 15-minute presentation at the end of the program to summarize her/his results. The SURFOs found the report writing and oral presentation intimidating initially, but they all agreed that it was a worthwhile experience that helped them summarize and realize the scope of their summer projects. We also instituted a new 15-minute presentation during the fourth week of the program during which SURFO students presented the scope of their summer project. Included in the summer events was our annual day of kayaking on the Narrow River, led by Bob Sand, to investigate the flora and fauna of an estuary. A subset of SURFOs also

participated in a series of field days funded by other projects where water sampling and fish trawls were made at several locations in Narragansett Bay and Rhode Island Sound. We also continued with our tradition of having an informal noontime barbecue for the SURFOs on the veranda at the Horn Lab. This provided the SURFOs with a taste of graduate-student life in an informal setting where they were able to meet with GSO faculty, graduate students and staff. The annual SURFOs vs ADVISORS softball game was a tie in extra innings (just like the MLB All-Star Game), but this allowed the advisors to continue their undefeated streak.

One measure of success of our program is if fellows continue on with graduate studies in science and, specifically, in oceanography or ocean engineering. The exit questionnaire indicates that all 11 of the 11 students definitely plan to continue on with graduate studies in science/engineering. Of these, 7 said they are seriously considering oceanography.

The participants in the 2002 SURFO program are grateful to the National Science Foundation for its support of the program through grant OCE-9912236. Kathryn Ford (USSAC-ODP) and Yang Shen (OCE-9906902) also provided supplemental NSF funding for undergraduate research for Andrea Mullen and John Blum, respectively. The SURFO participants and I would like to thank all of those individuals at URI who contributed to the program's success including those who advised the students and who gave SURFO seminar presentations. In addition, our thanks to Rhonda Kenny and Kim Carey for their assistance in the preparation of this report as well as the administrative, financial and recruitment tasks. Finally, we would like to thank Kelly Kriner who served as a graduate coordinator for the program, Friends of Oceanography for providing seminar refreshments, and Bob Sand for running the kayak trip.

Robert A. Pockalny
SURFO Site Director

TABLE OF CONTENTS

A Regional Analysis of Multibeam Backscatter Data from the Southwest Pacific

Mark Barthelemy[1] and Rob Pockalny

Graduate School of Oceanography, University of Rhode Island, Narragansett, RI, USA.

Abstract. Multibeam backscatter data collected with SEA BEAM 2000 in the southwest Pacific basin have been used to determine the spatial and temporal variability of backscatter energy from various physiographic provinces. The backscatter data were divided into 3-, 6- and 24-hour increments to determine the characteristic across-track backscatter distribution for each time period. The mean , Y-intercept and slope were calculated for each time increment and then plotted on the regional bathymetry to identify spatial or temporal patterns. Several factors appear to be responsible for regional variations in backscatter strength in the portion of the southwest Pacific surveyed by COOK04MV, including, systematic and morphologic sources. The systematic variations are associated with the general decay in signal strength away from the nadir and the apparent DC-shift in backscatter strength associated with gain adjustments during data collection. The primary morphologic source appears to be associated with sediment thickness variations; however, correlations with depth and latitude may also be involved. An interesting relationship between the orientation of seafloor fabric, ship's heading, and backscatter strength suggests an additional correction may be required to better assess the regional character of backscatter strength.

1. Introduction

The majority of multibeam sonar surveys conducted in the open ocean have been concentrated along the mid-ocean ridge system. Sediment thickness in this environment is typically very low (< 10 m) and multibeam backscatter data are able to image the original seafloor fabric. On older oceanic crust, sediment thickness generally increases with crustal age to the point that the original seafloor fabric is no longer resolved. In the southwest Pacific basin (Fig. 1), anomalously thin sediments (<50 m) have been observed overlying crust of the mid- Cretaceous age (84 to 120 Ma) [Pockalny et al., 2002]. Preliminary analyses of the backscatter and bathymetry data indicate the original seafloor fabric is visible in this region. We present the results of a detailed analysis of the backscatter data collected during the COOK04 cruise aboard the R/V Melville to determine if regional patterns or trends in backscatter characteristics exist (Fig 1).

2. Background

A detailed tectonic history of the southwest Pacific basin is difficult to determine due to the lack of correlatable seafloor magnetic anomalies associated with the uniform polarity of the mid-Cretaceous-aged oceanic crust in the region. Recent geophysical surveys in the area [Larson et al., 2002; Pockalny et al., 2002], however, have used regional bathymetry and gravity data to document the relocation and southeastward migration of a ridge-ridge-ridge RRR triple junction trace (Fig. 1). In this scenario, the triple junction relocated from a position just westward of the Nova-Canton Trough at 120 Ma to the center of the Manihiki Plateau, created as result of a volcanic plume event about 119-121 Ma. Seafloor spreading along the newly relocated Pacific-Farallon, Farallon-Phoenix, and Pacific-Phoenix spreading centers produced a NW-SE trending lineament that represents the triple junction trace of the Pacific-Farallon and Pacific-Phoenix ridges. The continued southeastward migration of the RRR triple junction is verified by the magnetic bight of magnetic anomaly 34 (~ 84 Ma).

The crust on the western side of the triple junction was created by the ENE-trending, Pacific-Phoenix ridge at an ultra fast-spreading ridge (~18 cm/yr, full rate) [Larson et al., 2002]. Similarly trending abyssal hills are observed and have low relief that is typical of faster spreading ridges. The crust on the eastern side of the triple junction was created by the NNW-SSE trending, slow-intermediate spreading (~2-7 cm/yr) Pacific-Farallon ridge. Abyssal hills trending NNW with slightly greater relief are observed and are indicative of intermediate spreading rates. Seamount chains cross the region with a NNW-SSE trend with the age of volcanism decreasing toward the NNW [Koppers et al., 2001]. As a result of this more recent volcanism, the crust in this region has been reheated and the regional topography associated with the volcanic chain have been elevated or thermally reset. There are also several E-W trending fracture zones on the eastern side of the triple junction trace that appear to intersect the fracture

[1]Now at the University of New Orleans, New Orleans, Louisiana, USA

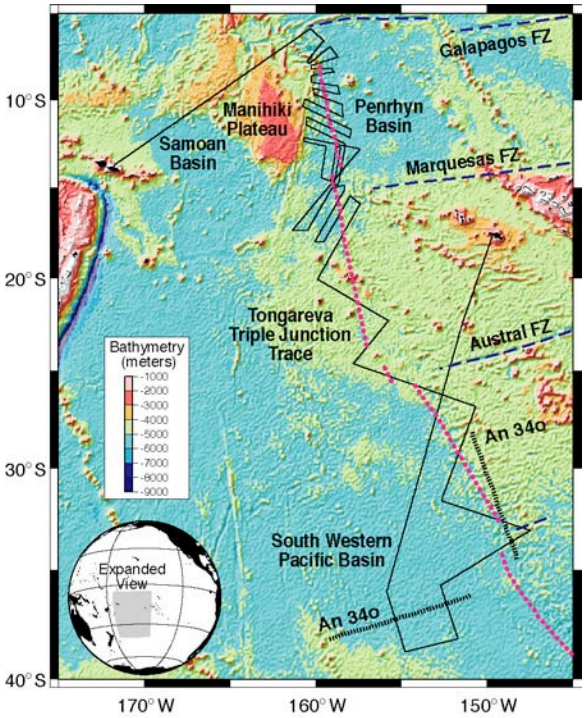

Figure 1. Predicted topography [Smith and Sandwell, 1997] overlain with the location of COOK04MV cruisetrack and key geographic features. Numbered and color coded regions correspond to sample swath data shown below.

zones at "kinks" in the triple junction trace. These fracture zones include the Galapogos, Marqueses, and Austral fracture zones and are characterized by very rough topography oriented normal to the abyssal hill fabric.

3. Data

The multibeam data used for this study were collected aboard the R/V Melville (Cook04MV) from November 11, 2000 to December 22, 2000 in the southwest Pacific basin (Fig.1). The primary survey area (5˚S - 40˚S, 140˚W - 165˚W) criss-crossed Pandora's Escarpment located to the west and southwest of Tahiti and to the east and southeast of the Manihiki Plateau. The multibeam data were collected with the hull-mounted SEA BEAM 2000 system, which is a 12 kHz, deep-water sonar with 121 beams and 2.0 degree by 2.0-degree resolution [L-3 Communication, 2000]. This system covers an angular range of –60 to 60 degrees from the vertical. The coverage area or swath width on the seafloor is dependent on bathymetry with the across-track dimensions equal to ~ 3 times the water depth. The horizontal footprint produced by a single beam is about 150 x 150 m underneath the ship.

Multibeam sonar systems provide fan-shaped coverage of the seafloor similar to sidescan sonar. Similar to side-scan systems, multibeam sonar uses transducers to convert electric energy into vibration energy (sound). The converted energy is projected into the water until it encounters an interface with different acoustic impedance. At that point, the sound pulse is reflected and a fraction of the energy is returned to the transducers on the ship. Since the outgoing sound has a certain frequency, wavelength, and duration the transducers are able to scale and digitize the returning energy. The newly digitized data is processed into either bathymetry data or backscatter data. Bathymetry data is processed as a function of two-way travel time while backscatter data is recorded as a function of the magnitude of the energy that is returned for a given beam angle.

There are several factors that have an affect on the character of the recorded backscatter multibeam data, including: frequency of outgoing energy, water depth, water properties, and seafloor properties. There is a general relationship between frequency of a sonar system and the resolution and subsurface penetration. Higher frequency systems yield higher resolution bathymetric measurements, but the rate of attenuation of the energy is faster than comparable low frequency systems. The 12 kHz system used by SEA BEAM 2000 provides both adequate resolution and energy transmission. This system even continues to transmit energy up to 5 m into sediment. A greater water depth will increase the travel-time of the sound in water and will result in greater attenuation of the energy. Post-processing of the backscatter data in conjunction with the measured bathymetry generally correct for the bathymetric effects. The properties of the water column, mainly the temperature-depth profile, will also affect the path of outgoing energy. Expendable bathythermographs (XBTs) are typically deployed twice a day to correct for refraction patterns. Perhaps the most important factor affecting the character of the backscatter data are the physical properties of the seafloor. Seafloor with higher acoustic impedance (e.g., basaltic basement) will reflect more energy than regions with lower acoustic impedance (e.g., sediments). In addition, topographic slopes facing the ship will reflect more energy back toward the ship than slopes facing away.

For this study, we assume that most of the geometrical factors (e.g., water depth and refracted paths) have been removed during prior data post-processing. Therefore variations in backscatter energy are primarily the result of varying seafloor characteristics.

4. Methods

The analysis of the multibeam backscatter data involved using MB-System [Caress and Chayes, 1993] and Generic Mapping Tools (GMT) software [Wessel and Smith, 1998] and proceeded in several steps. The first step was to plot the original backscatter data in mapview to observe regional variations and to identify anomalous characteristics or artifacts in the data. Page-sized plots at a scale of 4"/degree were made using the MBmosaic utility from the MB-Systems software which were then hand-mosaicked for a complete view of the Cook04MV survey area. The plots revealed a distinct across-track distribution with the greatest amount of

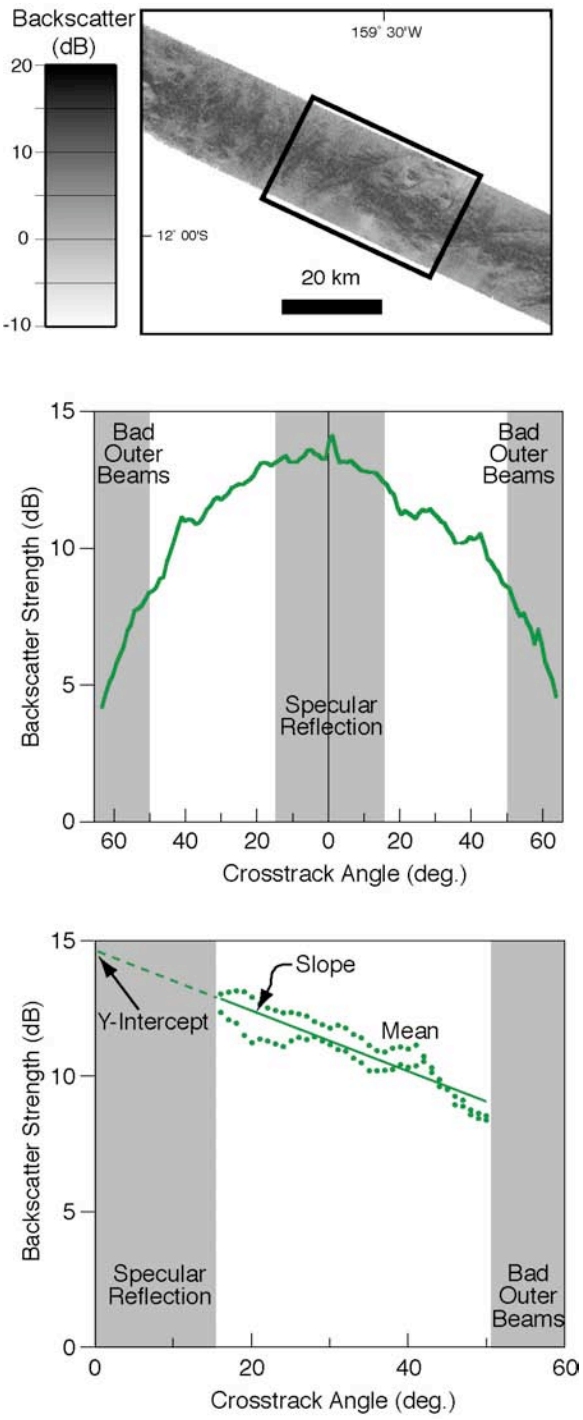

Figure 2. Swath of of SEABEAM 2000 backcatter data (top), a time-integrated across-track distribution of backscatter strength (center), and the various parameters used for the regional analysis of backscatter data (bottom).

backscatter energy located directly beneath the ship and decaying outward away from the center beam (Fig. 2). These plots also identified distinct steps in backscatter strength that correlated with adjustments in the gain values recorded in the science log. The most prevalent step occurred halfway through the cruise, which made it

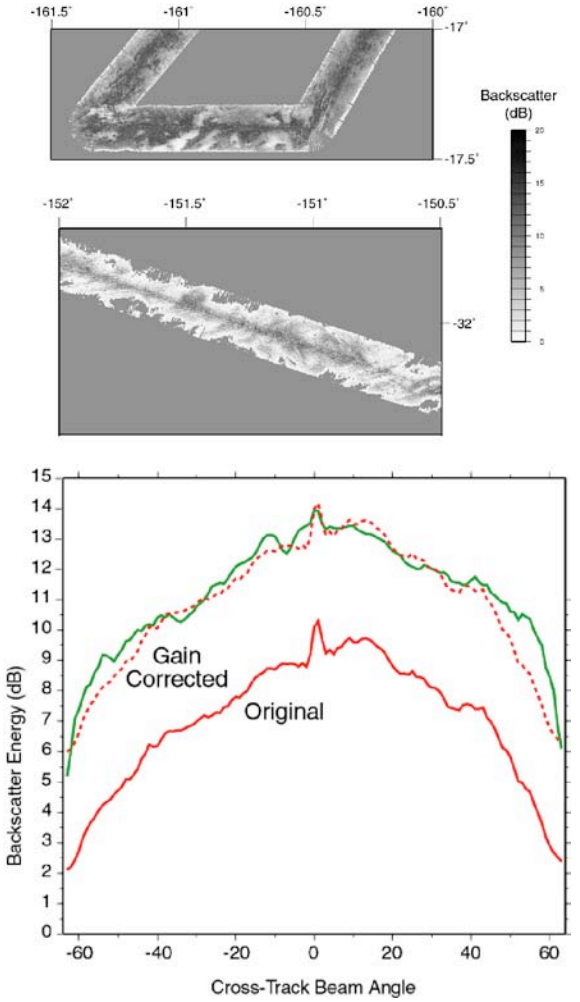

Figure 3. An example of the difference in backscatter strength before and after the gain adjustment of November 16, 2000 at 1800 GMT. A DC-shift in backscatter strength was used to correct for this gain adjustment.

difficult to identify any larger scale regional changes in backscatter distributions. These gain changes were adjusted by increasing or DC-shifting the backscatter values by 3 dB after 1800 GMT on November 26, 2000. An example of this gain adjustment is shown in Figure 3.

The second step involved using the MBbackangle utility from the MB-Systems software to calculate time-averaged, across-track backscatter profiles for user-defined sections of the data. Initially, the data were divided into 42, 24-hour segments to characterize the coarse regional patterns in backscatter strength. In general, these across-track profiles displayed an inverted parabolic shape that documented the previously observed trend of stronger backscatter strength directly under the ship (Fig. 2). Comparison of the individual profiles did not exhibit any obvious regional patterns in backscatter character.

The third step involved identifying parameters that would adequately characterize the backscatter profile for

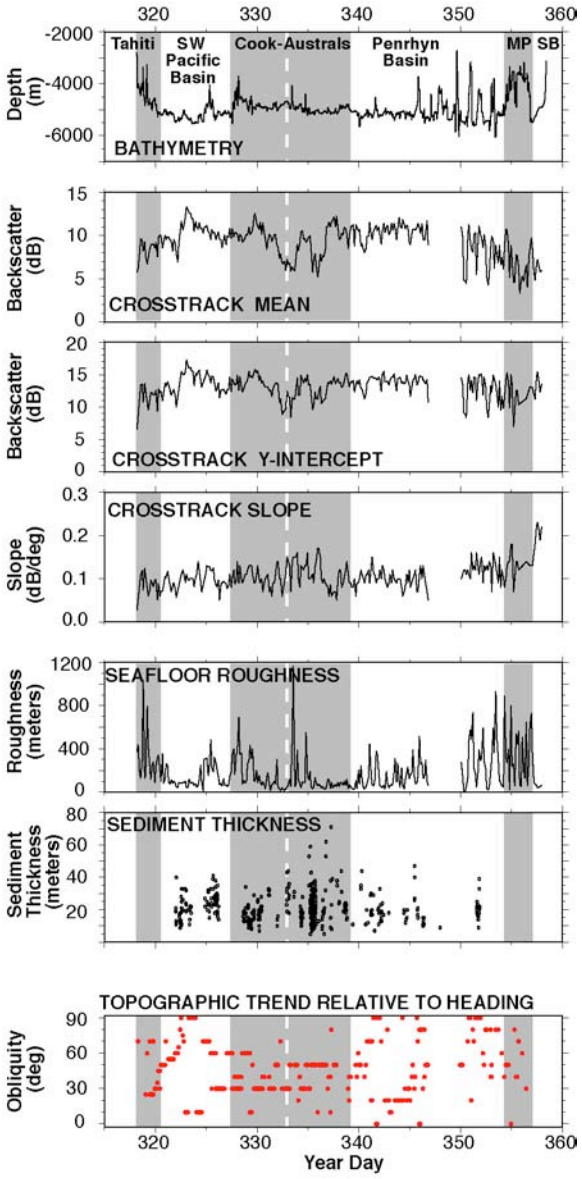

Figure 4. Series of along-track measured backscatter values (mean, y-intercept and slope) and various morphologic and physiographic characteristics. None of these parameters alone appear to correlate with the observed changes in backscatter strength.

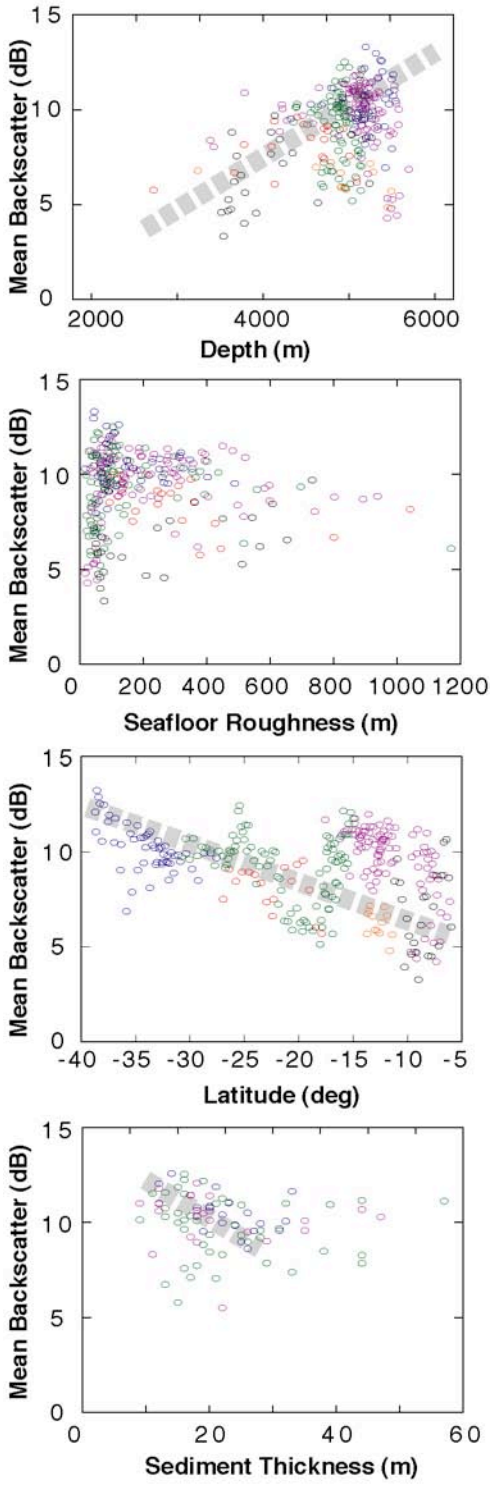

Figure 5. Series of graphs illustrating the correlations between mean backscatter and various parameters.

a given time period and allow for easy spatial and temporal comparison. First, the across-track backscatter values for the port and starboard beams were combined and the values corresponding to specular reflection (< 15˚ from nadir) and the bad outer beams (> 50˚ from nadir) were removed (Fig. 2). The mean backscatter strength of the remaining values was then calculated. A best-fit line was also applied and the Y-intercept and slope were recorded. Plots of time-averaged, along-track changes in mean backscatter, Y-intercept and slopes were plotted and compared to factors such as depth, seafloor roughness, sediment thickness and orientation of seafloor fabric (Fig. 4). Cross-correlations were made between each of the calculated backscatter parameters and the measured regional physiographic/morphologic parameters. The results of these correlations are very similar the mean, Y-intercept and slope values, so only the results of the mean backscatter are discussed in the observations.

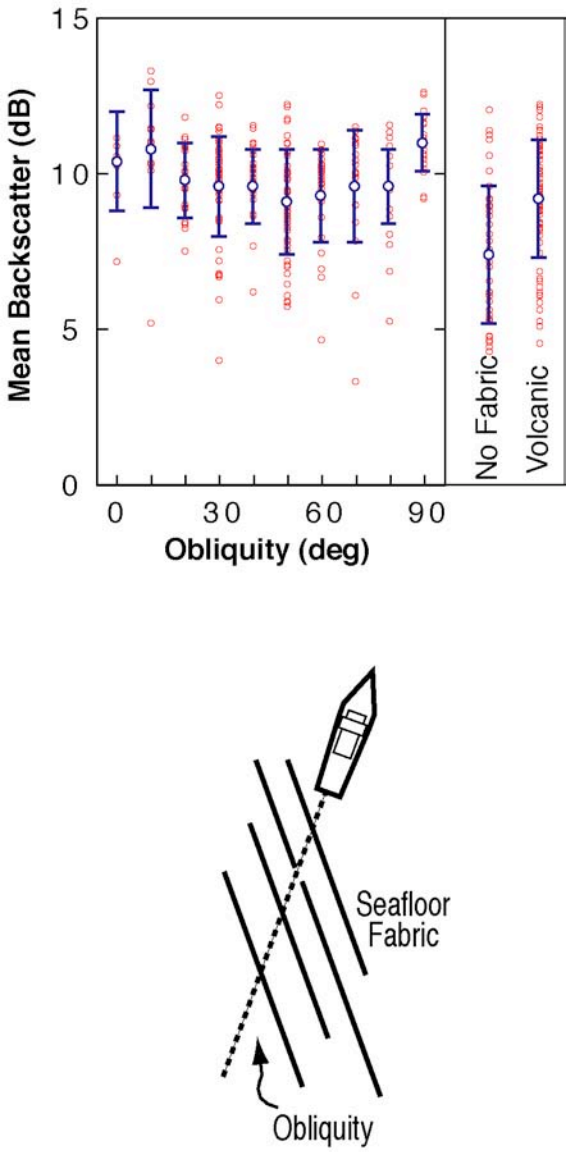

Figure 6. Graph (top) and graphic (bottom) illustrating the change of mean backscatter strength as a function of seafloor fabric orientation and morphology.

5. Observations

The primary observations of this study suggest a positive correlation of backscatter strength with depth and an inverse correlation with latitude and sediment thickness (Fig. 5). An interesting correlation is also observed withthe orientation of seafloor fabric, where larger average backscatter values are obtained for fabric oriented normal or parallel to the ship's heading (Fig. 6). There does not appear to be a significant correlation with seafloor roughness in the region surveyed.

The positive correlation of backscatter strength with bathymetry (Fig. 5) seems counterintuitive considering that backscatter strength is likely to be more attenuated the farther it has to travel in the water column. These data have already been corrected for water depth, so the observed correlation likely indicates the presence of lower reflectivity or thicker sediments at shallower depths. The majority of the Manihiki Plateau presently has a mean depth of less than 4000 m, which is shallower than the typical calcium compensation depth for the Pacific.

The inverse correlation of backscatter strength with sediment thickness is observed for sediment thicknesses less than 40m (Fig. 5). The maximum backscatter strength decreases steadily with increasing sediment thickness and then becomes more erratic for sediment thicknesses greater than 40 m. This correlation is somewhat surprising since the 12 kHz signal likely penetrates the upper 5 m of sediment before becoming attenuated. This correlation may be a result of a decreased seafloor roughness that is associated with sediment thickness greater than 40 m [Bird and Pockalny, 1994]. An analysis of seafloor roughness (Fig. 5), defined as the standard deviation of bathymetry within the appropriate bathymetric swath, does not exhibit a similar correlation with backscatter strength. Therefore, an alternative explanation for the correlation with sediment thickness is required and may be related to the limitations of using 3.5 kHz data to estimate sediment thickness.

An overall decrease in backscatter strength as the survey region approaches the equator is also observed (Fig. 5). Exceptions to this trend are associated with the heavily sedimented Manihiki Plateau and Samoa Basins. This overall trend also correlates with the age of the crust, which increases in age toward the equator. This would suggest a similar correlation with sediment thickness, as discussed in the previous paragraphs.

One of the most surprising observations from this study is the interesting correlation of backscatter strength relative to the orientation of the trend of the seafloor fabric (Fig. 6). The largest mean backscatter values are associated with survey lines oriented parallel or normal to the regional seafloor fabric. The lowest backscatter values are associated with seafloor fabric oriented at 45° to the ship's heading or with seafloor ornamented with numerous small seamounts.

6. Conclusions

Several factors appear to be responsible for regional variations in backscatter strength in the portion of the southwest Pacific surveyed by COOK04MV, including, systematic and morphologic sources. The systematic variations are associated with the general decay in signal strength away from the nadir and the apparent DC-shift in backscatter strength associated with gain adjustments during data collection.

The primary morphologic source appears to be associated with sediment thickness variations; however, correlations with depth and latitude may also be involved. An interesting relationship between the orientation of seafloor fabric, ship's heading, and backscatter strength suggests an additional correction may be required to better assess the regional character of backscatter strength.

Acknowledgments. I am especially grateful to Rob Pockalny for giving me the opportunity to do research here. I would also like to thank Rich Viso for being available whenever I needed any help. And, last but not least, I would like to send a special thanks to everyone else at GSO for being supportive and making this a pleasant atmosphere to spend my summer.

References

Bird, R., and R. Pockalny, Late Cretaceous and Cenozoic seafloor and oceanic basement roughness: Spreading rate, crustal age and sediment thickness correlations: Earth Planet. Sci. Lett., 123, 239-254, 1994

Caress, D.W., and D.N. Chayes, MB-System Version 3, Open source software distributed from the L-DEO ftp site, 1993.

Koppers, A. A., J. Phipps Morgan, J. W. Morgan, and H. Staudigel, Earth Planet. Sci. Lett., 185, 237-252, 2001.

Larson, R. L., R. Pockalny, R. Viso, E. Erba, L. Abrams, B. Luyendyk, J. Stock, R. Clayton, Mid-Cretaceous tectonic evolution of the Tongareva triple junction in the southwestern Pacific basin, Geology, 30, 67-70, 2002

L-3 Communications Sea Beam Instruments " Milestones: Sea Beam Instruments" http://www.seabeam.com/mileston, 2000.

Pockalny, R., R. Larson, and R. Viso, Bathymetry and gravity data across a mid-Cretaceous triple junction trace in the southwest Pacific basin: Geophysical Research Letters, 29, 7-1 – 7-4, 2002.

Smith, W. H. F. and D. T. Sandwell, Science, 277, 1956-1962, 1997.

Wessel, P., and W. H. F. Smith, 1998, New, improved version of the Generic Mapping Tools Released, EOS Trans. AGU, 79, 579, 1998

Mark Barthelemy. Department of Geology & Geophysics, University of New Orleans, New Orleans, LA, 70148. (mbarthel2002@yahoo.com).

Robert Pockalny. Graduate School of Oceanography, University of Rhode Island, Narragansett, RI, 02882, USA.

Mantle seismic discontinuity structure beneath southern Africa

John Blum[1] and Yang Shen

Graduate School of Oceanography, University of Rhode Island, Narragansett, RI, USA.

Abstract. Temporary broadband seismic networks in southern Africa record the conversion of P-waves to S-waves in the mantle beneath the stations. The P to S conversion points are geographically binned, and the radial receiver functions in each bin are stacked to observe lateral variations in the mantle discontinuity structure. The stacked traces reveal the mantle transition zone is ~ 5–20 km thicker than normal beneath the Kaapvaal and Zimbabwe cratons, normal beneath the Bushveld province, and thinner than normal beneath the Namaqua-Natal Mobile and Cape Fold belts. The thicker-than-normal transition zone beneath the expansive cratons suggests that the upper mantle is not anomalously warm, and that the hypothesized thermal plume beneath southern Africa is confined to the lower mantle. The thick transition zone also supports the notion of a cold continental root penetrating the transition zone beneath the Archaean cratons, more than 100 km deeper than previously suggested. A water enriched upper mantle near 400-km depth – consistent with theories of craton formation -- may additionally elevate the 410-km discontinuity, accounting for the thicker transition zone. Although local anomalies are present, the case for a widespread, subhorizontal seismic discontinuity beneath the transition zone to a depth of ~ 1500 km is marginal. We consistently detect a distinct, negative amplitude phase preceding the 660-km discontinuity, a feature that may represent a chemical layer above the 660-km discontinuity.

1. Introduction

Mantle seismic discontinuities -- characterized by rapid variations in seismic velocity -- are widely accepted to exist in the upper mantle near 410- and 660-km depth. The 410- and 660-km discontinuities are identified as phase transitions from α-olivine to β-spinel (wadsleyite) and from β-spinel (ringwoodite) to $(Mg,Fe)SiO_3$-perovskite plus (Mg,Fe)O-magnesiowüstite [Liu, 1979; Bina, 1991], respectively. Other seismic discontinuities have been identified in the mid-mantle at depths of 900-1700 km in subduction zone regions [Kawakatsu and Niu, 1994; Kaneshima and Helffrich, 1998], near 1050 km beneath the Hawaiian and Iceland hotspots [Shen et. al., submitted], and near 1200 km beneath the African rift [Le Stunff et al., 1995].

The causes of the mid-mantle seismic discontinuities are not known. Two possible explanations are changes in the chemical composition of the mantle [Davaille, 1999; Kellogg et al., 1999] and mineral phase transitions [Bina, 1998]. Recent evidence against a mineral phase transition of the normal mantle includes the absence of significant P-wave to S-wave (P_dS) conversions in the mid-mantle beneath Iceland -- except within the hot and narrow plume [Shen et al., submitted]. Other studies have noted an absence of consistent scattering in the search for mid-mantle seismic boundaries [Vidale et al., 2001; Castle and van der Hilst, 2001]. Although the observed mid-mantle discontinuities are a feature consistent with geodynamical models having compositional stratification in the lower mantle [Kellogg et al., 1999; Davaille, 1999; van der Hilst and Kárason, 1999; Tackley, 2000], it is not known whether the mid-mantle seismic discontinuities are common globally, or are unique to regions of upwelling and downwelling within the mantle. Whereas a global phase transition or compositional boundary is not laterally constrained, a discontinuity associated with the thermal structure of a mantle plume is spatially restricted. A broad and continuous search for mid-mantle seismic discontinuities in regions of mantle upwelling is necessary in order to assess the role of temperature on these discontinuities, and to determine if the discontinuities are compositional, mineralogical, or thermal in origin.

Beneath southern Africa, a region of presumed mantle upwelling, seismic evidence suggests a complex mantle structure. Global tomographic studies have revealed the presence of a large, low seismic velocity anomaly deep within the mantle [van der Hilst et al., 1997; Grand et al., 1997; Zhao, 2001; Ni et al., 2002]. The prominent, plume-like velocity anomaly is greater than 1000 km wide [Zhao, 2001; Ni et al., 2002] and rises upwards over 1000 km from the core-mantle-boundary (CMB) [van der Hilst et al., 1997; Grand et al., 1997, Ni et al., 2002]. The plume may extend from the CMB beneath southern Africa to the surface near the east African hotspot [Zhao, 2001]. The high, uplifted topography of Africa has been attributed to the upwelling of an anomalously hot mantle [Lithgow-Bertelloni et al., 1998]. A mid-mantle discontinuity has been identified at 1200 km beneath the African rift (~ 10°S) from the stacking of P'P' precursors [Le Stunff et al., 1995]. Furthermore, Ishii and Tromp [1999] analyzed free-oscillation data and found that denser than average material coincides with the low velocity anomaly above the CMB. The anomalous density-velocity relationship suggests chemical layering deep beneath South Africa. Whether the compositional anomaly extends to shallower mantle may have important implications for the dynamics of the mantle.

[1]Now at Department of Physics, University of Michigan, Ann Arbor, MI, 48109, USA.

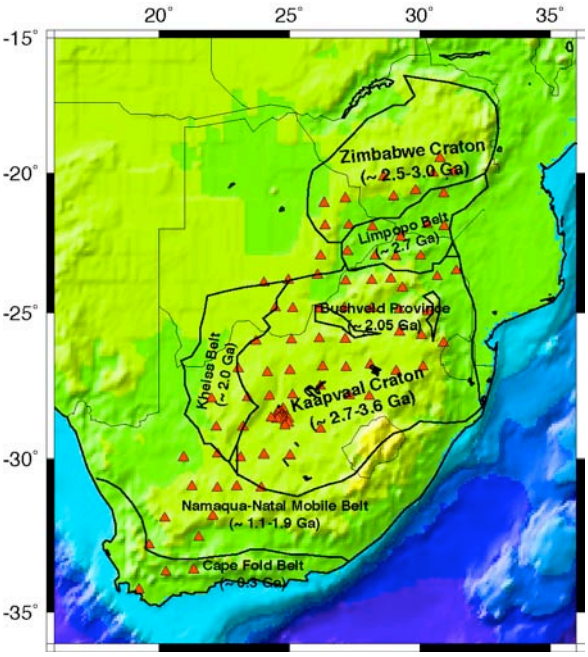

Figure 1. Map displaying the seismic station locations and the principal geologic terrains in the study area. Digital broadband seismometers are denoted by triangles, and were deployed at 113 sites from April 1997 to July 1999. The array extends SSW-NNE from the Cape Fold Belt to the Zimbabwe craton.

The southern African lithosphere encompasses extensive Archaean cratons (Fig 1.). It has been suggested that deep continental roots may influence the upper mantle to depths of at least 300 km, and possibly greater than 410 km [Gu et al., 1998]. Recent broadband seismic experiments in southern African have revealed upper mantle seismic structure, including the presence of high velocity mantle roots extending to depths of at least 300 km beneath the Archaean Zimbabwe and Kaapvaal cratons [James et al., 2001; James and Fouch, 2002]. In this paper, we present the analysis of converted P_dS phases whose seismic rays pierce the upper 1500 km mantle beneath southern Africa, and consider the implications of mantle discontinuity structure in the presence of the upwelling lower-mantle plume and continental root.

2. Methods

2.1. Data set

We use teleseismic body waves recorded by two temporary seismic networks consisting of 113 sites across southern Africa. The digital broadband networks operated from April 1997 to July 1999, and from December 1998 to July 1999 [James et al., 2001; James and Fouch, 2002]; they extend from Cape Town, South Africa to regions of Masvingo, Zimbabwe, and Botswana (Fig 1). Only events of magnitude 5.5 and greater were examined. The waveforms were sliced between 80 s before the P-wave arrival and 5 s before the PP arrival. Noise levels were defined as the standard deviation of the radial values in the 80 s window preceding the P-wave arrival. Filtered waveforms having noise levels less than 0.1 times the amplitude of the direct P-wave on the vertical component were selected for analysis. A total of 3300 seismograms representing 283 earthquakes were chosen.

2.2 Calculation of radial receiver functions

After the waveforms were selected and sliced, the vertical P-wave components were deconvoluted from the radial components to produce the radial receiver functions: a scaled version of the radial component with the PP arrival removed [Langston, 1979; Ammon, 1991]. The deconvolution was completed using the Clayton and Wiggins water level method of deconvolution [Clayton and Wiggins, 1976].

2.3 Stacking of receiver functions

The P_dS conversions result in an S-wave with energy small compared to the incident P-wave, yielding a low-quality signal. In order to improve the quality of the signal, the study area was split into an array of overlapping circular bins spanning the seismic stations. Adjacent bins have a 2/3 overlap. The receiver functions of P_dS paths piercing the same bin at a given depth in the mantle were gathered and stacked [Dueker and Sheehan, 1997; Shen et al., 1998] using an nth root (n=2) stacking process [Kanasewich, et al., 1973]. The non-linear stacking process enhances coherent phases and suppresses random noise. Only bins with a minimum of 64 traces in the transition zone are further analyzed. A bootstrap resampling method was used to determine the arrival times of the stacked traces [Efron and Gong, 1983]. 25 resamples of each stack were calculated, and P_dS arrival times were measured for each bootstrap. The best values and their errors were obtained from the mean and standard deviation of the replicated distributions, respectively.

3. Results

3.1 Mantle discontinuities

The resulting stacked traces reveal the mantle discontinuity structure beneath southern Africa. Figure 2 displays the stacked results of all receiver functions gathered in a circular bin of radius 2˚, located at the center of the array (26˚S, 26˚W). The phases at times of ~ 42 s and ~ 66 s mark the 410- and 660-km discontinuities (P410s and P660s), respectively. Marginal phases exist near 103 s and 122 s. A distinct, negative amplitude phase precedes P660s. In order to examine the lateral variations of the phases beneath southern Africa, receiver functions were stacked along NWW-SEE and SSW-NNE transects (Fig. 3a). The transects display clear P410s and P660s arrivals, as well as a consistent negative arrival at about 60 s. Although local anomalies are present in the mid-mantle, the case for a widespread, subhorizontal seismic discontinuity to a depth of ~ 1500 km is marginal.

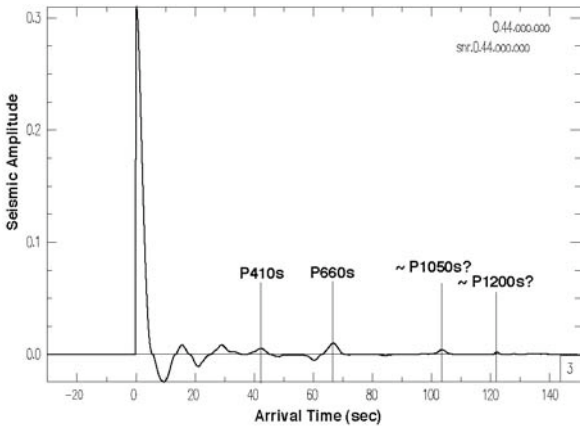

Figure 2. Stacked receiver functions for a circular bin of 2˚ radius at the center of the array (26˚E,26˚S). The distinct phases at arrival times of ~42 s and ~66 s represent the P to S conversions of the 410- and 660-km discontinuities, respectively. A negative arrival near 60 s precedes the P660s conversion.

3.2 Mantle transition zone thickness

The transition zone thickness -- represented by the differential time between the P660s and P410s arrivals -- was calculated according to the observed arrival times in the stack traces. Figure 3b shows a map view displaying the difference between the observed P660s-P410s differential times and the predicted iasp91 values [Kennett and Engdahl, 1991]. The map view indicates a thicker than normal transition zone at the Zimbabwe and Kaapvaal cratons. A transition zone of normal value appears between the two cratons, coinciding surfacially with the Bushveld province. A thinner than normal transition zone exists at the Namaqua-Natal Belt and Cape Fold Belt. E-W and N-S transects of the stacked receiver functions (Fig. 3c) reproduce the thickness variations shown in the color map view. The traces are aligned at the observed P410s arrival time. It is not known if the transition zone thickness variations are produced by a shallower 410-km discontinuity, or a deeper 660-km discontinuity, compared to normal; only the transition zone thickness is well determined.

4. Discussion

The failure to detect a widespread, subhorizontal discontinuity in the mid-mantle does not exclude the possibility of the presence of a discontinuity beneath the transition zone. The stacking method we employed systematically searches for subhorizontal discontinuities over a broad area. A mid-mantle discontinuity having significant topographic relief will be sparsely detected using this method, and only appear in local, subhorizontal patches. Additionally, the absence of a broad discontinuity beneath the transition zone, accompanied by local detections, may indicate weak P_dS conversions, thereby making a discontinuity difficult to detect.

The upper mantle discontinuity structure appears unaffected by the lower-mantle low-velocity anomaly. The positive and negative Clayperon slopes of the 410-km and 660-km discontinuities, respectively, would dictate a thinning of the transition zone in the presence of thermal upwelling. Similarly, a cold, thermal anomaly penetrating the transition zone would thicken the transition zone [Revenaugh and Jordan, 1991]. Although the transition zone thickness is normal beneath the Bushveld province, and thinner than normal beneath the Namaqua-Natal and Cape Fold Belts, the thicker than normal transition zone beneath the expansive Zimbabwe and Kaapvaal cratons suggests the upper mantle is not anomalously warm. The signature of the hypothesized thermal plume is thereby confined to the lower mantle. This inference confirms the result of an earlier study by Gao et al. [2002], who reported the mantle transition zone thickness across a single SW-NE transect to be of normal value.

The transition zone thickness variations with respect to distinct geologic provinces imply a relationship between the surfacial terrains and mantle structure. Our results geographically coincide with recent P-wave and S-wave imaging of the upper mantle beneath southern Africa [James et al., 2001; James and Fouch, 2002]. The P-wave and S-wave images show patches of high seismic velocities extending to depths of 300 km and greater beneath the Zimbabwe and Kaapvaal cratons. This is evidence of a tectospheric structure rooted deep beneath the continent. Since the high velocities of deep tectospheric structures are generally associated with low geotherms [Jordan, 1975], the thicker than normal transition zones, combined with the presence of deep continental roots, suggest that the cold continental keels may penetrate the transition zone beneath the cratons. This notion is augmented by the fact that the oldest and coldest region of the Kaapvaal craton, and also the deepest continental keel, is in the east. The thickest transition zone is also observed beneath the eastern part of the Kaapvaal craton.

Since the depths of the 410- and 660-km discontinuities are not well determined, it is difficult to constrain the effect of the low geotherm associated with the deep tectospheric roots. We suggest that the influence is unlikely to extend to the 660-km discontinuity. Not only do the P- and S-wave velocity anomalies poorly extend to this depth, but travel time inversion also tends to smear velocity anomalies along dominant ray paths. As a result, anomalies beneath regions of best ray density (200-400 km depth) [James and Fouch, 2002] may appear greater than the actual values. The implication is that the inferred low geotherm is more likely to have a pronounced effect on the 410-km discontinuity than the 660-km transition, and an elevated 410-km discontinuity results in the thicker transition zone.

A low geotherm, however, is not required to produce the thicker than normal transition zone; other possible mechanisms such as compositional variations can also induce the thickness. For example, an iron enriched mantle would produce a shallower and broader 410-km discontinuity [Katsura and Ito, 1989]. The bulk of the mantle beneath the cratons, however, is highly depleted [James and Fouch, 2002]. Similarly, regions of rich

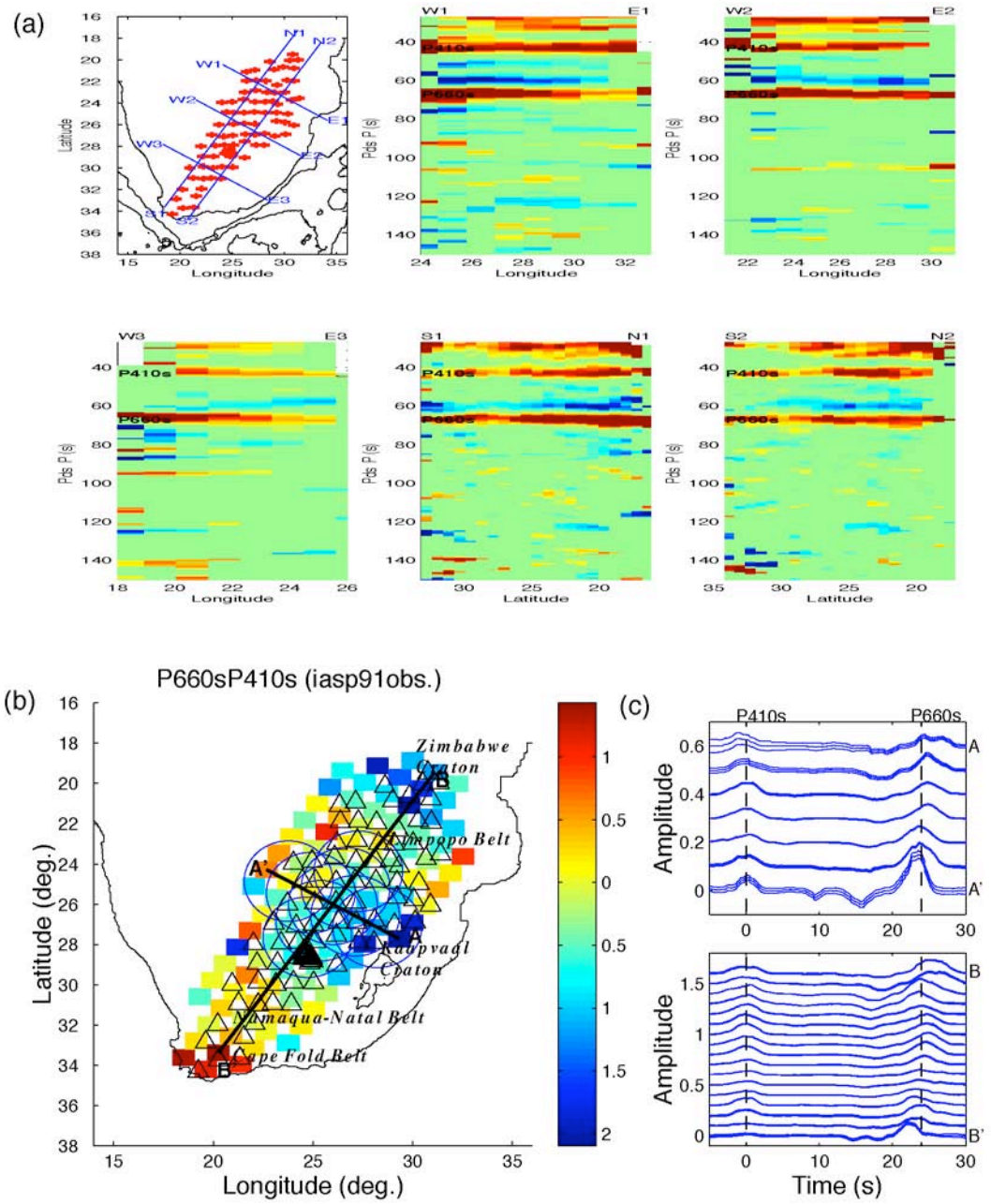

Figure 3. (a) Receiver functions gathered in 2˚ radius circular bins are stacked along NWW-SEE and SSW-NNE transects. The stacked traces display clear P410s and P660s converted phases. The negative arrival preceding the P660s phase is a consistent feature beneath southern Africa. P_dS conversions are present beneath the transition zone to a time of 150 s after the incident P arrival, but are not indicative of a widespread, subhorizontal discontinuity within the mid-mantle. (b) The map view displays the difference between the observed P660s-P410s differential times and the predicted iasp91 values. The color scale is in units of seconds, and blue colors denote significantly greater than normal P660s-P410s differential times and mark a thicker than normal mantle transition zone. Yellows and red denote a normal to thinner transition zone. Thicker transition zones exist beneath the Zimbabwe and Kaapvaal cratons. A normal transition zone is found beneath the Bushveld province just south of the Limpopo Belt. Thinner than normal transition zones exist beneath the Namaqua-Natal and Cape Fold Belts. (c) Waveform receiver functions are stacked along the transects A-A' and B-B'. The bootstrap calculated arrival times of the traces are aligned at the iasp91 predicted P410s arrival time. The dashed lines indicate the iasp91 predicted P410s and P660s arrival times, respectively. Only the differential times, and thus the transition zone thickness, are well determined.

H_2O content within the α-β transition would stabilize β-spinel, resulting in a shallower and broader 410-km discontinuity compared to regions of normal value. A mantle with 500 ppm H_2O, for example, is calculated to have an 8 km shallower α-β transition than a normal source with 200 ppm H_2O [Wood, 1995]. Unlike iron, the notion of a water enriched transition zone is consistent with our knowledge of the Archaean cratons. The cratonic lithosphere is believed to have developed as a series ofrapid magmatic and tectonic processes in the presence of subduction zones [de Wit et al., 1992; Parman et al., 2000]. Subducting lithosphere has been shown to release H_2O into the mantle between 300 and 500 km depth [Nolet and Zielhuis, 1994], and petrological results have indicated that Archaean South African komatites were substantially enriched in water [Carlson et al., 2000]. It is therefore reasonable to suppose that the early subductions released significant water into the upper mantle beneath the cratons. One method to test for a H_2O enriched transition zone would be to examine the sharpness of the α-β transformation. Given the 0.5 to 2.0 s (~ 5-20 km) thicker than normal transition zone beneath the cratons, however, it is unlikely that a H_2O enriched α-β transformation alone accounts for the thickness variations. Most likely, both a cold thermal anomaly and significant H_2O are present.

Other terrains such as the Bushveld province, and the Namaqua-Natal and Cape Fold Belts, are distinguished by lower seismic velocities. The Bushveld province, located in the northern Kaapvaal craton and encompassing the Bushveld Complex westward, is suggested to have been refertilized (iron enriched) during a massive volcanic event near 2.05 Ga [James and Fouch, 2002]. While iron-enrichment produces lower seismic velocities -- a feature observed in the P- and S-wave inversions -- it should also elevate the 410-km discontinuity. The normal transition zone structure, however, implies either the presence of a shallower 660-km discontinuity, thermal insulation of the region from the continental keels due to iron enrichment, or other compositional effects to normalize the transition zone.

The thinner than normal transition zone beneath the Namaqua-Natal and Cape Fold belts coincide with a relatively thin lithosphere [James et al., 2001]. Additionally, tomographic studies have indicated a negative P-wave velocity anomaly near or within the transition zone beneath the Cape-Fold Belt near the Vema intraplate hotspot (16˚E,32˚S) [James and Fouch, 2002; Zhao 2001], suggesting the hot thermal structure to thin the transition zone. The difference in P660s-P410s differential time between the belts and cratons approaches 3.0 ± 0.5 s. This corresponds to an ~ 30 km thinner transition zone beneath the Cape-Fold Belt than the nearby cratons, significantly greater than the 10 km reported by Gao et al. [2002]. This is consistent with the notion of a cold, continental keel penetrating the transition zone beneath the cratons, and the absence of the tectospheric feature beneath post-Archaean regions.

The negative arrival preceding P660s warrants further discussion. Previous studies have noted negative arrivals between P410s and P660s at Iceland and the southern East Pacific Rise [Shen et al., 1998], and also beneath southern Africa [Gao et al., 2002]. Although the distinct feature has not been exhaustively studied, the negative arrival near 60 s is consistent with a slow to fast velocity contrast above the 660 km discontinuity. Such a contrast may indicate a distinct chemical layer exists between 500 and 600 km.

5. Conclusions

P_dS converted phases beneath southern Africa clearly demonstrate the 410- and 660-km discontinuities. Although local anomalies occur, the search for a broad, subhorizontal discontinuity in the mid-mantle beneath the transition zone appears marginal. Transition zone thickness variations coincide with distinct geologic terrains. Thicker than normal transition zones appear beneath the Zimbabwe and Kaapvaal cratons, normal beneath the Bushveld province, and thinner than normal beneath the Namaqua-Natal and Cape Fold belts. The thick transition zone beneath the core of the continent -- the old, cool cratons -- suggests that the plume anomaly inferred from low-velocities in the lower mantle is confined to the lower mantle. The thick transition zone also supports the notion of a continental keel penetrating the 410-km discontinuity. H_2O enrichment of the transition zone may also account for the thick transition zone. These findings support models of craton formation, and implicate that tectospheric keels may be more deeply rooted in the mantle than previously suggested. A deep continental root also explains the near fixed African plate, 'anchoring' the continent to the mantle. The distinct negative arrival before P660s remains unknown, but is suggested for future study to represent a distinct chemical layer between 500 and 600 km depth.

Acknowledgments. We would like to thank Rob Pockalny for graphics assistance, and Jennifer Georgen for helpful reviews of this manuscript. Roger Larson, Ting Yang, and Rich Viso deserve additional acknowledgement for their comments and suggestions. This work was supported by the US NSF.

References

Ammon, C.J., The isolation of receiver effects from teleseismic P waveforms, *Bull. Seism. Soc. Am., 81,* 2504--2510, 1991.

Bina, C.R., Mantle discontinuities, *Rev. Geophys., 29,* 783--793, 1991.

Bina, C.R., Lower mantle mineralogy and the geophysical perspective, *Rev. Mineral, 37,* 205--239, 1998.

Carlson, R.W., F.R. Boyd, S.B. Shirey, P.E. Janney, T.L. Grove, S.A. Bowring, M.D. Schmitz, J.C. Dann, D.R. Bell, J.J. Gurney, S.H. Richardson, M. Tredoux, A.H. Menzies, D.G. Pearson, R.J. Hart, A.H. Wilson, and D. Moser, Continental growth, preservations and modification in southern Africa, *GSA Today, 10,* 1--7, 2000.

Castle, J.C. and R.D. van der Hilst, Searching for seismic scattering off mantle interfaces between 800 km and 2000 km depth, *J. Geophys. Res.,* in press, 2001.

Clayton, R. W., and R. A. Wiggins, Source shape estimation and deconvolution of teleseismic body waves, *Geophys. J. R. Astron. Soc., 47,* 151--177, 1976.

Davaille, A., Simulataneous generation of hotspots and superswells by convection in a heterogeneous planetary mantle, *Nature, 402,* 756--760, 1999.

de Wit, M.J., C. Roering, R.J. Hart, R.A. Armstron, C.E.J. de Ronde, R.W.E. Green, M. Tredoux, E. Peberdy, and R.A. Hart, Formation of an Archaean continent, *Nature, 357,* 553-562, 1992.

Dueker, K.G., and A.F. Sheehan, Mantle discontinuity structure beneath the colorado Rocky Mountains and High Plains, *J. Geophys. Res.,103,* 7153--7169, 1998.

Efron, B. and G. Gong, A leisure look at the bootstrap, the jackknife, and cross-validation, *Amer. Stat., 37,* 36--48, 1983.

Gao, S. S., P. G. Silver, K. H. Liu, and the Kaapvaal Seismic Group, Mantle discontinuities beneath Southern Africa, *Geophys. Res. Lett., 29,* 1291-1294, 2002.

Gu, Y., A. M. Dziewonski, and C. B. Agee, Global de-correlation of the topography of transition zone discontinuities, *Earth Planet. Sci. Lett., 157,* 57--67, 1998.

Grand, S.P., R.D. van der Hilst, and S. Widiyantoro, Global seismic tomography: a snapshot of convection in the Earth, *GSA Today, 7 (4),* 1--7, 1997.

Ishii, M. and J. Tromp, Normal-mode and free-air gravity constraints on lateral variations in velocity and density of Earth's mantle, *Science, 285,* 1231--1236, 1999.

James, D. E., M. J. Fouch, J. C. VanDecar, S van der Lee, and Kaapvaal Seismic Group, Tectospheric structure beneath southern Africa, *Geophys. Res. Lett., 28,* 2485--2488, 2001.

James, D.E., and M.J. Fouch, Formation and evolution of Archaean cratons: insights from southern Africa, *Geological Society of Roy. Astron. Soc. special publication: Early Earth*, 2002.

Jordan, T. H., The continental tectosphere, *Rev. Geophys., 13,* 1--12, 1975.

Kanasewich, E.R., C.D. Hemmings, and T. Alpaslan, Nth-root stack nonlinear multichannel filter, *Geophysics, 38,* 327--338, 1973.

Kaneshima, S. and G. Helffrich, Detection of lower mantle scatterers northeast of the Marianna subduction zone using short-period array data, *J. Geophys. Res., 103,* 4825--4838, 1998.

Katsura, T. and E. Ito, The system Mg_2SiO_4-Fe_2SiO_4 at high pressures and high temperatures. Precise determinations of stabilities of olivine, modified spinerl, and spinel, *J. Geophys. Res., 94,* 15663--15670, 1989.

Kawakatsu, H. and F. Niu, Seismic evidence for a 920-km discontinuity in the mantle, *Nature, 371,* 301--305, 1994.

Kellogg, L.H., B.H. Hager, and R.D. van der Hilst, Compositional stratification in the deep mantle, *Science, 283,* 1881--1884, 1999.

Kennett, B. L. N. and E. R. Engdahl, Travel times for global earthquake location and phase identification, *Geophys. J. Int., 105,* 429--466, 1991.

Langston, C.A., Structure under Mount Rainer, Washington, inferred from teleseismic body wave, *J. Geophys. Res., 84,* 4749--4762, 1979.

Le Stunff, Y., C.W. Wicks Jr., and B. Romanowicz, P'P' precursors under Africa: evidence for mid-mantle reflectors, *Science, 270,* 74--77, 1995.

Lithgow-Bertelloni, C., and P.G. Silver, Dynamic topography plate driving forces and the African superswell, *Nature, 395,* 269--273, 1998.

Liu, L.-G., *The Earth: its origin, structure and evolution,* 177--202, ed. McElhinny, M.W., Academic Press, San Diego, Calif., 1979.

Ni, S., E. Tan., M. Gurnis., and D. Helmberger, Sharp sides to the African superplume, *Science, 296,* 1850--1852, 2002.

Nolet, G. and A. Zielhuis, Low S velocities under the Tornquist-Teisseyre zone; evidence for water injection into the transtion zone by subduction, *J. Geophy. Res., 99,* 15813--15820, 1994.

Parman, S.W., J.C. Dann, and T.L. Grove, The production of Barberton komatiites in an Archean subduction zone, *Geophys. Res. Lett., 28,* 2513--2516, 2001.

Revenaugh, J. and T. H. Jordan, Mantle layering from ScS reverberations; 2, The transition zone, *J. Geophys. Res., 96,* 19,763--19780, 1991.

Shen, Y., A. F. Sheehan, K. G. Dueker, C. de Groot-Hedlin, and H. Gilbert, Mantle discontinuity structure beneath the southern East Pacific Rise from P-to-S converted phases, *Science, 280,* 1232--1235, 1998.

Shen, Y., S. Solomon, C. Bjarnason, Th. I., and C.J. Wolfe, Seismic evidence for a lower-mantle origin of the Iceland plume, *Nature, 395,* 62--65, 1998.

Shen, Y., C.J. Wolfe, and S.C. Solomon., Seismological evidence for a mid-mantle discontinuity beneath Hawaii and Iceland, *submitted to Nature,* 2002.

Tackley, P.J., Mantle convection and plate tectonics: toward an integrated physical and chemical theory, *Science, 288,* 2002--2007, 2000.

van der Hilst, R.D., S. Widiyantoro, and E.R. Engdahl, Evidence for deep mantle circulation from global tomography, *Nature, 386,* 578--584, 1997.

van der Hilst, R.D. and H. Kárason, Compositional heterogeneity in the bottom 1000 kilometers of Earth's mantle: toward a hybrid convection model, *Science, 283,* 1885--1888, 1999.

Vidale, J.E., G. Schubert, and P.S. Earle, Unsuccessful initial search for a midmantle chemical boundary with seismic arrays, *Geophys. Res. Lett., 28,* 859--862, 2001.

Wood, B. J., The effect of H_2O on the 410-kilometer seismic discontinuity, *Science, 268,* 74--76, 1995.

Zhao, Dapeng, Seismic structure and origin of hotspots and mantle plumes, *Earth Planet. Sci. Lett., 192,* 251-265, 2001.

John Blum. Department of Physics, University of Michigan, Ann Arbor, MI, 48109, USA. (johnblum@umich.edu).

Yang Shen. Graduate School of Oceanography, University of Rhode Island, Narragansett, RI, 02882, USA.

Acute Cortisol Stress Response of Juvenile Winter Flounder (*Pseudopleuronectes americanus*, Linnaeus) to Predation

Jason P. Breves and Jennifer L. Specker

Graduate School of Oceanography, University of Rhode Island, Narragansett, Rhode Island

Abstract. Wild stocks of winter flounder (*Pseudopleuronectes americanus*) in the Northwestern Atlantic have been depleted via fishing pressure to an extent that has warranted increasingly stronger fishing regulations in the last decade. As a means to strengthen the wild populations of winter flounder and to avoid further fishing restrictions the rearing of juvenile fish in hatcheries for release in coastal waters has been viewed as a possibility. Many fishery biologists have concern that hatchery-reared fish are not behaviorally and/or physiologically equipped to survive in the wild due to a lack of predator interaction and conditioning in culture conditions. However, an investigation of the physiological responses linked to predation of hatchery-reared winter flounder has not been described. This study aimed to determine if there is a stress response, as evidenced by an increase in cortisol production, in hatchery-reared juvenile winter flounder to predatory activity. Predation by green crabs (*Carcinus maenas*) and sand shrimp (*Crangon septemspinosa*) have been implicated as a source of juvenile flounder mortality in laboratory and field studies and therefore were chosen as the invertebrate predators in this study. In addition, the summer flounder (*Parylichthys dentatus*) was selected as a predator for this study because of its co-existence with young winter flounder in estuaries at selected times of the year. Juvenile fish (n =12) were subjected to the pressure of predation for 24h in an arena. Results from radioimmunoassay techniques indicate that juvenile winter flounder initiate a cortisol response to sand shrimp and summer flounder predation, while the predation from a green crab does not elicit such a response. The ability of a fish to detect and react to a stress such as predation is vital to the survival of that individual to a reproductive size. This study represents the first step toward understanding the stress physiology of hatchery-reared juvenile winter flounder to predation. Information regarding the physiology of hatchery-reared fish will provide insight into the value of stock enhancement through the release of cultured winter flounder.

1. Introduction

Winter flounder (*Pseudopleuronectes americanus*) stocks in the Northwestern Atlantic have been depleted as a result of several population pressures. In addition to over fishing, the leading cause of the natural stock depletion, an increase in predation as a result of warmer coastal water temperatures has been suggested (Keller and Klein-MacPhee 2000). As a means to strengthen the wild populations of winter flounder, and to avoid further fishing restrictions, the rearing of juvenile fish in hatcheries for release in coastal waters has been viewed as a possibility. Many fishery biologists are skeptical of such an approach because of the uncertainty regarding the fitness of hatchery-reared fish to survive natural environmental pressures such as predation. Juvenile winter flounder are susceptible to the predation of several different types of predators after settlement. An increased understanding of the relationship between juvenile winter flounder of hatchery origin and its predators will aid in appraising the value of stock enhancement by the release of wild fish into coastal waters.

Predation upon newly settled flatfish greatly affects the year-class strength of that season (Van der Veer and Bergman 1987). Crabs have been documented in a variety of regions worldwide, including estuaries in the southern US, as an important predator in flatfish population dynamics (Reichert and Van der Veer 1991). Recently it has been shown in laboratory studies that juvenile winter flounder are vulnerable to green crab (*Carcinus maenas*) predation (Fairchild and Howell 2000). This information is relevant since green crabs and juvenile winter flounder co-exist spatially and temporally in coastal waters.

Decapod crustacean predation has been implicated as a fine control mechanism for yearly class variations in flatfish (Van der Veer and Bergman 1987). In regions such as the Wadden Sea, *Crangon* shrimp species are the most widely documented predator of young-of-the-year flatfish (Fairchild and Howell 2000). Witting and Able (1995) established that the highest mortality rates due to shrimp predation occur around the time of settlement when a flatfish changes from a pelagic to a benthic lifestyle. The sand shrimp (*Crangon septemspinosa*) has been shown to consume juvenile winter flounder in laboratory trials and appears to be an important predator of flatfish in nursery grounds (Van der Veer and Bergman 1987).

Summer flounder (*Paralichthys dentatus*) is a highly piscivorous species that co-occurs temporally and spatially with juvenile winter flounder. Adult summer flounder and juvenile winter flounder are both present in Narragansett Bay from May to October (Stone et al. 1994). An increase in coastal water temperatures, which are presently being experienced, may increase the

[1]Now at Roger Williams Univeristy , Bristol, RI, 02809.

population of summer flounder in coastal waters. The increased abundance of summer flounder may in turn increase pressure upon juvenile winter flounder populations. A better understanding of the relationship between juvenile winter flounder and adult summer flounder may increase awareness about the consequences of coastal ocean warming.

The stress response of teleosts as evidenced by corticosteriod production has been documented in a variety of species. The release of cortisol by the interrenal into the blood and tissues represents the link between the initial neuroendocrine perception of stress and the mobilization of energy. Mobilized energy is used for changes in behavior and/or physiology to restore an organism to homeostasis with its environment. Studies have aimed at determining the cortisol response of flatfish to a multitude of stressors, most notably those of interest to the aquaculture industry. Waring et al. (1992) characterized the stress response of the flatfish *Platichthys flesus* to handling and net confinement while Barnett and Pankhurst (1998) examined the stress response of greenback flounder to a variety of aquaculture practices. These two studies showed that crowding, confinement, and handling are stressors capable of producing elevated plasma cortisol levels. To this point studies regarding the physiology of stress in flatfish have not examined predation as a possible stressor.

The purpose of this study was to evaluate the stress response to predation in cultured winter flounder. As a tool to investigate the stress elicited by predation, whole body cortisol levels were used to quantify the physiological response to predation by juvenile winter flounder. In addition to determining if there is a cortisol stress response to predation, our study compared the magnitude of the acute stress response of winter flounder to predators with contrasting feeding habits. Information from this study aims to increase knowledge of the teleost endocrine system and provide new insight into the ecophysiology of a flatfish species.

2. Materials and Methods

2.1 Fish Maintenance

All juvenile winter flounder (55 days after hatch) were acquired from the Lennoco Inc. Hatchery in Chatham, MA and transported to the University of Rhode Island Narragansett Bay Campus in April of 2002. Fish were maintained in flow-through seawater (30 ppt) in a holding tank until time of experiment trials. The temperature of the holding tank ranged from 17° C in the early summer to 22° C at time of last experiment. Juvenile fish were fed HUFA enriched *Artemia nauplii*. Laboratory lighting was maintained at a 12:12 light dark cycle and remained unchanged throughout the duration of the study period.

2.2 Experimental Design

Winter flounder (n=12) were placed into an experimental arena. Each arena consisted of a round tub 45 cm in diameter filled with filtered seawater (30 ppt) at 20-22º C. A 2-3 cm thick layer of fine sediment was placed at the bottom of each arena. Light aeration was maintained throughout each experiment. Fish were housed in the arenas for a 48h acclimation period before addition of a predator.

Green crabs and sand shrimp were collected from Narragansett Bay and maintained in flow-through systems until time of experiment. The carapace width of crabs used in this study ranged from 55–70 mm. The total length of sand shrimp used in this study ranged from 50-60 mm. Prior to addition to predator-prey arenas green crabs and sand shrimp were starved for 48h to encourage predatory activity upon interaction with fish. Summer flounder of 100-110 mm total length were acquired from cultured stocks at the University of Rhode Island's Flounder Facility. Summer flounder predators were housed in a holding tank with juvenile winter flounder as a food source.

Upon completion of the 48h acclimation period predators were added to treatment tanks while control tanks were maintained without the addition of predators. Two sets of predator and control arenas were performed for each experiment. For trials involving the green crabs and summer flounder the predator-prey ratio was 1:12. For trials involving shrimp predation a ratio of 2:12 was established. Predator-prey aquaria were maintained under normal photoperiod patterns that were the same as those maintained in the holding tank system. Predator-prey trials lasted for 24h until sampling was conducted.

2.3 Sampling

Upon completion of the 24h interaction period, predators were removed from trial aquaria and transferred back to a holding tank. Fish were immediately netted and administered a lethal dose of 2-phenoxyethanol (Sigma) in seawater. Fish were then removed from 2-PE, blotted with filter paper, and placed in pre-weighed plastic sample tubes. Individual fish wet weights were determined to the nearest 1.0 mg and samples preserved at –80° C.

2.4 Cortisol Extraction and Radioimmunoassay

Flounder individuals were sectioned and homogenized in 1000 µL of phosphate buffer (PBS) with pH 7.6. Samples were then spiked with a 1000 cpm volume (~10 µL) of radioactive cortisol for extraction efficiency calculation. Cortisol was extracted from fish samples using three 1.5 mL volumes of ether. Sample tubes were allowed to evaporate overnight before RIA analysis was conducted.

Dried tubes were reconstituted with 500 µL of standard diluent with a pH of 7.4. Fifty mL of reconstituted sample was then pipetted along with 5 mL of scintillation fluid into vials and placed into a scintillation counter. The recorded counts per minute value was compared to the original count determined for the 1000 cpm volume to determine radioactive cortisol extraction efficiencies for each fish sample. The mean extraction efficiency for all cortisol assays was 44.8% +/- 1.2%.

Fish samples of 200 µL were run in duplicate with 100 µL of labeled cortisol and 100 µL of cortisol

antibody at a 1:200 dilution. Tubes containing fish sample, labeled cortisol, and antibody were incubated overnight at 4° C. Following incubation, 400 µL of dextran coated charcoal (DCC) was added to remove unbound cortisol. Tubes were then centrifuged for 15 minutes at 4° C to separate the charcoal from the sample prior to removal of 500 µL of sample for counting in the scintillation counter.

Counts associated with each sample were compared against a standard curve of known cortisol concentrations. The amount of cortisol contained in each tube was then calculated and the whole body cortisol level of the fish determined from the fish's wet weight. Data was then compiled and readied for statistical analysis.

2.5 Analysis

Statistical analysis was conducted using a one-way analysis of variance to determine significance of cortisol responses in regard to treatment. P-values were calculated from log normalized whole body cortisol values to satisfy homogeneity of variance requirements. For all statistical analysis significance was accepted when $P<0.05$.

3. Results

3.1 Experiment #1- Green Crab Predation

Green crab experimental trials resulted in a reduction of the number of individuals in three of the four trial tanks (Table 1). Fish found dead in predator tanks upon inspection appeared not to die of predatory activity from the crab. In trial 1 (Fig 1) whole body cortisol levels in winter flounder exposed to green crab predation (9.86 +/- 2.56 ng/g) was not significantly elevated over the control group (9.60 +/- 2.32 ng/g; P=0.88). In trial 2 (Fig 2), the mean cortisol levels of fish exposed to predation (5.57 +/- 1.64 ng/g) was not significantly greater than the mean cortisol level of control fish (4.94 +/- 0.89 ng/g; P=0.59).

3.2 Experiment #2- Sand Shrimp Predation

Shrimp predation experiments yielded one viable pair of control and predator trials. Sampling of the second trial was unsuccessful due to heavy mortality in the

Winter Flounder Survival

Experiment	Presence of Predator	Trial I	Trial II
Crab	+	92	100
	-	92	83
Shrimp	+	83	17
	-	83	75
S. Flounder	+	83	50
	-	83	83

Table 1. Percent survival of juvenile winter flounder at completion of 24h trial period.

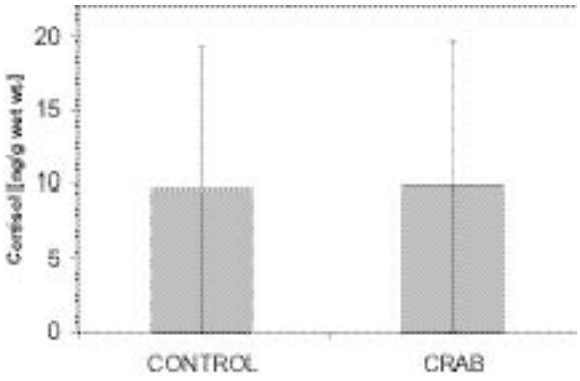

Figure 1. Mean (+/- SEM) whole body cortisol concentration (ng/g of wet wt.) of winter flounder exposed to green crab predation and corresponding control group (Trial 1).

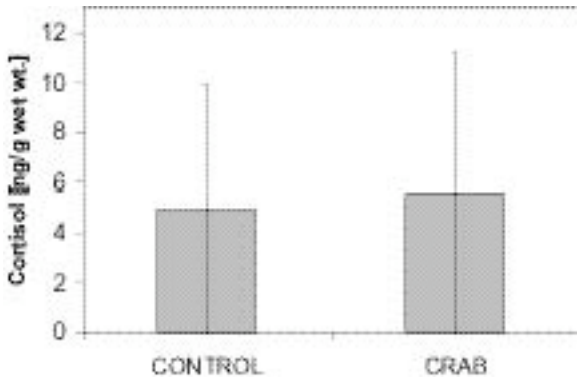

Figure 2. Mean (+/- SEM) whole body cortisol concentration (ng/g of wet wt.) of winter flounder exposed to green crab predation and corresponding control group (Trial 2).

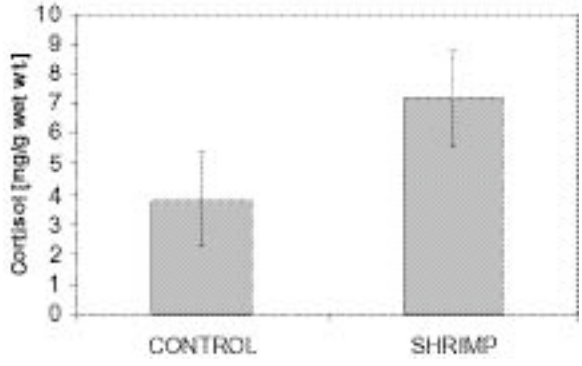

Figure 3. Mean (+/- SEM) whole body cortisol concentration (ng/g of wet wt.) of winter flounder exposed to sand shrimp predation and corresponding control group.

predator tank (Table 1). It did not appear that the mortality was a result of shrimp predation but rather of abiotic factors. In addition to a poor number of sampled fish, RIA analysis yielded cortisol levels that were extremely variable. Data from the second trial was discarded due to an extremely small number of samples and a low level of confidence in the values. In the first trial (Fig. 3) the whole body cortisol levels of fish exposed to shrimp predation (7.19 +/- 1.60 ng/g) was significantly greater than that of the control fish (3.82 +/- 1.54 ng/g; P=0.04).

3.3 Experiment #3- Summer Flounder Predation

The cortisol level of fish from trial one (Fig. 4) exposed to summer flounder predation (13.20 +/- 6.60 ng/g) was greater than control fish (5.56 +/- 0.74 ng/g). Despite the difference in cortisol levels between the control and treatment fish the values were not significantly different (P=0.62). Similar to trial one, cortisol levels of fish exposed to a summer flounder predator in trial two (Fig. 5) had a greater mean cortisol level than control fish. However, in trial two the difference in means was statistically significant (P=0.03). Fish subjected to summer flounder predation experienced a mean cortisol level of 5.92 +/- 1.23 ng/g while control fish experienced a mean cortisol level of 2.96 +/- 0.77 ng/g.

4. Discussion

The most important finding of this study is that predation from sand shrimp and summer flounder is capable of eliciting a cortisol stress response in hatchery-reared juvenile winter flounder. In the only viable experiment with shrimp predation statistical analysis supported the difference in cortisol levels observed between control and treatment fish. Summer flounder predation produced a significant elevation of cortisol levels in one of two trials. However, in the trial in which cortisol was not found to be significantly elevated by predation there is a considerable difference in the mean values between groups. In this case, a large standard error may be strongly influencing statistical analysis.

Predation from green crabs did not result in the elevation of whole body cortisol levels in both trials. It is possible that the predatory behavior of green crabs may not require flatfish to mobilize energy for sustained behavior to avoid predation. Another potential reason for the lack of a cortisol response is that the abundance of green crabs in local estuaries historically has not been great enough to warrant the development of a stress response. Green crabs are a non-indigenous species that were introduced on the eastern seaboard in the early nineteenth century (Levinton 2001). Despite the presence of blue crabs in coastal waters, it is possible that an interaction between green crabs and winter flounder for less than two hundred years is not a sufficient amount of time to initiate a physiological link between the two species.

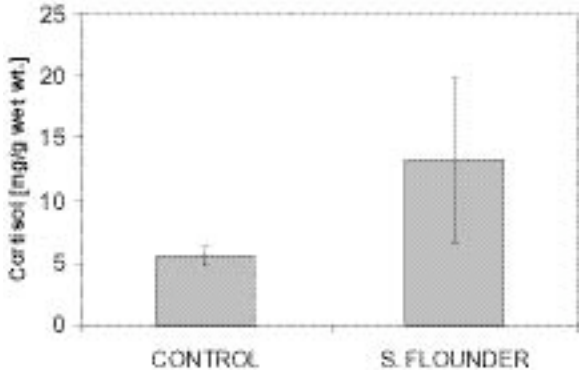

Figure 4. Mean (+/- SEM) whole body cortisol concentration (ng/g of wet wt.) of winter flounder exposed to summer flounder predation and corresponding control group (Trial 1).

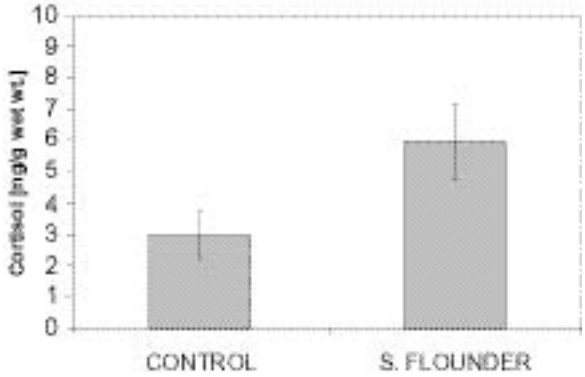

Figure 5. Mean (+/- SEM) whole body cortisol concentration (ng/g of wet wt.) of winter flounder exposed to summer flounder predation and corresponding control group (Trial 2).

The mean cortisol level of fish in control arenas varied from trial to trial in each experiment. Abiotic factors such as temperature, dissolved oxygen, and lighting were tightly controlled, and are unlikely to be the cause of the observed variation. Differences in control values may be due to natural variation of cortisol levels of fish in captivity. Further studies regarding cortisol levels of juvenile winter flounder in captivity would prove valuable in clarifying the reasons for the variation in whole body cortisol levels we observed.

Despite the variation in control values it is possible to compare the magnitude of the cortisol response to different predators in statistically significant trials. In the shrimp experiment (Fig. 2) the mean cortisol levels of fish exposed to predation were 1.9 times greater than the mean levels of control fish. In the second trial of the summer flounder experiment (Fig. 5) the mean cortisol levels of fish exposed to predation were 2.0 times greater than the mean cortisol levels of control fish. It is possible that the stress response to predation in juvenile winter flounder may be of the same magnitude irrespective of the predator involved.

A survival rate greater than 80% was observed in the majority of arenas at the conclusion of the 24h time frames. Inspection of the deceased fish suggested that they did not die of wounds inflicted by the added predator. Deceased fish did not resemble illustrations presented by Seikai et al. (1993) of flatfish preyed upon by a Crangonid shrimp. Further evidence for mortality not associated with predation is that fish were found dead in control arenas as well. We are unsure as to the cause of mortality in the trial arenas. It is possible that a certain percentage of fish in each trial were not capable of acclimating sufficiently to the change in aquaria.

The use of cortisol as a tool to investigate predatory stress between species may prove to be valuable. Further work needs to be done to determine if there is a relationship between a cortisol response elicited by a predator and the probability of a successful predatory interaction between the two species. Olla et al. (1992) determined that an elevation in cortisol levels in juvenile coho salmon reduces the ability of salmon to avoid predation soon after stress initiated by handling. A study of this nature upon juvenile winter flounder involving predator stress elicited cortisol levels would provide insight into the pathway between the neuroendocrine perception of stress and behavior in flatfish species.

Another area for future research would involve the comparison of the physiology associated with predation between cultured juvenile winter flounder and wild juvenile winter flounder. In a behavioral study, Kellison et al. (2000) observed that fish from a hatchery environment spent significantly more time swimming in the water column and took longer to become cryptic on the benthos than wild conspecifics. The authors concluded that hatchery-reared fish are not as well suited for survival in the wild due to a lack of predator interaction in rearing conditions. A comparison of the physiology involved in predator detection may elucidate the reasons for the differences in behavior of cultured flatfish in comparison to wild flatfish.

Future research focused upon understanding the ecophysiology of juvenile winter flounder will better equip fishery biologists to evaluate restocking techniques. Yamashita et al. (2001) discussed how differences in ecological responses via physiological mechanisms effects the growth and survival of individuals and populations. They made the case that there is a vast array of biotic and abiotic factors, including predation, that affect the life cycles and survival of flatfish. Further work surrounding the physiological stress response of juvenile winter flounder to predation will educate biologists about the ecophysiology of flatfish and other teleost fish.

Acknowledgments. We gratefully acknowledge Steven Gavlik for assistance with preparing this paper and for consultation regarding experimental design. We also wish to thank Mary Chandlee for assistance with RIA protocol, Phil Veillette for assistance with statistical analysis, and Neil Marcaccio for assistance in the marine laboratory. In addition, we would like to acknowledge Dave Taylor for access to invertebrate predators used in this study and Rob Pockalny for directing the SURFO program. This project was funded by the National Science Foundation through the URI-GSO SURFO program.

References

Barnett CW, Pankhurst NW. (1998). The effects of common laboratory and husbandry practices on the stress response of greenback flounder *Rhombosolea tapirina* (Gunther, 1862). Aquaculture 162:313-329.

Fairchild EA, Howell WH. (2000). Predator-prey relationship between *Pseudopleuronectes americanus* and *Carcinus maenas*. Neth. J. Sea Res. 44:81-90.

Keller AA, Klein-MacPhee G. (2000). Impact of elevated temperature on the growth, survival, and trophic dynamics of winter flounder larvae: a mesocosm study. Can. J. Fish. Aquat. Sci. 57:2382-2392.

Kellison GT, Eggleston DB, Burke JS. (2000). Comparative behavior and survival of hatchery-reared versus wild summer flounder (*Paralichthys dentatus*). Can. J. Fish. Aquat. Sci. 57:1870-1877.

Levinton JS. (2001). *Marine Biology.* New York, N.Y.: Oxford Univ. Press. 515 pp.

Olla BL, Davis MW, Schreck CB. (1992). Comparison of predator avoidance capabilities with corticosteroid levels induced by stress in juvenile coho salmon. Transactions of the American Fisheries Society 121:544-547.

Reichert MJM, Van der Veer HW. (1991). Settlement, abundance, growth and mortality of juvenile flatfishes in a subtropical tidal estuary (Georgia, U.S.A.). Neth. J. Sea Res. 27: 375-391.

Seikai T, Kinoshita I, Tanaka M. (1993). Predation by Crangonid shrimp on juvenile Japanese flounder under laboratory conditions. Nippon Suisan Gakkaishi 59(2):321-326.

Stone SL, Lowery TA, Field JD, Williams CD, Nelson DM, Jury SH, Monaco ME, Andreasen L. (1994). Distribution and abundance of fishes and invertebrates in Mid-Atlantic estuaries. ELMR Rep. No. 12. NOAA/NOS Strategic Environmental Assessments Division, Silver Spring, MD. 280 p.

Van der Veer HW, Bergman MJN. (1987). Predation by crustaceans on a newly settled 0-group plaice *Pleuronectes platessa* population in the western Wadden Sea. Mar. Ecol. Prog. Ser. 35:203-215.

Waring CP, Stagg RM, Poxton MG. (1992). The effects of handling on flounder (*Platichthys flesus* L.). J. Fish Biol. 41:131-144.

Witting DA, Able KW. (1995). Predation by sevenspine bay shrimp *Crangon septemspinosa* on winter flounder *Pleuronectes americanus* during settlement: laboratory observations. Mar. Ecol. Prog. Ser. 123:23-31.

Yamashita Y, Tanaka M, Miller JM. (2001). Ecophysiology of juvenile flatfish in nursery grounds. Neth. J. Sea Res. 45:205-218.

J. P., Breves and J. L. Specker, Graduate School of Oceanography, University of Rhode Island, Narragansett, RI 02882. (jb2770@alpha.rwu.edu, jspecker@gso.uri.edu)

On the Formation and Evolution of Velocity Shear-Driven Flow Phenomena

Jennifer A. Dionne[1] and Peter Cornillon

Graduate School of Oceanography, University of Rhode Island, Narragansett, RI, USA.

Abstract. This paper outlines the analytical and experimental techniques employed in studying the shear flow dynamics associated with frontal formation and evolution. Empirical results were collected from a one-meter rotating table possessing a 50 cm diameter inner disc. By forcing the fluid inside the disc to rotate at a slightly different rate than that of the table, a velocity shear was created. A cross correlation algorithm implemented in MATLAB was used to determine the velocity of the fluid around the frontal region. Application of fundamental fluids theory, combined with numerical modeling techniques, allowed for quantification of lateral shear development. Analysis of the spin-up process indicated discrete turbulent eddy formation around the frontal region. As the spin-up approached steady state, a continuous frontal boundary layer was produced around the shear region. As expected, the direction of mean fluid flow inside the shear region was found to directly correlate with the rotation sense of the table. Immediately outside the boundary layer, however, fluid flow was observed to be in the opposite sense of mean table rotation. It was found that such results may be correlated with phenomena observed in the warm-outbreaks of the Gulf Stream.

1. Introduction

Shear flow dynamics have long presented a challenge to theoretical and empirical conceptions of fluid behavior. While an evolved shear region may be generally understood in terms of linear fluids theory, the principles governing such flow are poorly constrained. Moreover, while it is accepted that turbulent processes serve as the impetus behind shear flow formation, the relationship between turbulence and sheared flow has not been established - either analytically or experimentally. And yet, shearing forces assume a critical role in many phenomena, a most apparent illustration arising from oceanic fronts.

In the broadest of terms, a front may be defined as any physical boundary in which the mean background gradient is significantly less than the step across the boundary. Fronts generally define convergent regions in which fluid properties - such as density, temperature, or conductivity - are markedly different on either side of the convergence. Oceanic fronts may be either permanent or transient features. Irrespective of temporal extent, however, frontal boundaries outline a regime where a number of critical biological, chemical, and physical processes can be identified.

In studying fronts, much attention has been given to the Subtropical Convergence Zone (STCZ). Located in the North Atlantic, the STCZ marks the transition zone between the westerlies to the north and the trade winds to the south. The STCZ has been found to be a region of pronounced frontal activity, with meridional convergence of wind-driven Ekman transport considered an important mechanism for generating the fronts [Roden, 1975]. More recent studies [Cushman-Roisin, 1984 and deRuijter, 1983] have indicated that horizontal gradients of vertical surface heat fluxes may also contribute to STCZ frontogenesis. In addition, it is well established that the variability of subtropical fronts is affected by mesoscale and submesoscale eddies [Vorris and Schroeder, 1976; Voorhis and Bruce, 1982; Halliwell and Cornillon, 1989].

Application of an edge-detection algorithm developed at the University of Rhode Island's Graduate School of Oceanography to satellite derived data of sea surface temperature has allowed for the development of climatological frontal probability maps. Pointing to the probability of finding a front in a given region at a given time, these maps have extracted some most interesting – if not unanticipated - characteristics of subtropical frontogenesis. Conclusions from these maps have revealed that the subtropical zone in the North Atlantic shows strong seasonal variation, with significant differences in this variation from west to east. Such results suggest that the processes responsible for frontal formation west of the 45 degree meridian are likely different from those frontogenesis processes east of the meridian [Cornillon and Shan, 2000]. Moreover, these maps have indicated a time scale of frontogenesis on the order of one month.

Still, there is insufficient empirical and observational data to fully comprehend the forces responsible for frontal formation and evolution. An understanding of these dynamics would enhance frontal studies as applied to both oceanic processes and fluids applications in general. This study seeks to examine the form and function of such shear flow dynamics – in particular, those dynamics associated with and responsible for the development of frontal boundary layers.

[1]Now at Washington Univeristy, St. Louis, MO, 63130, USA.

2. Experimental Methodology & Apparatus

Properly considered, oceanic fronts are baroclinic regions (i.e., regions where the isobaric surfaces – surfaces of constant pressure – are not parallel for all depths z) characterized by an intense vertical shear and marked horizontal density gradients. An exact model of such frontal dynamics would fully describe the response of a variable density fluid to all possible forms of momentum and heat forcing. While such a model is impractical – if not impossible – to implement, it *is* possible to imagine representation of the system response in terms of eigenmodes of a linearized system of equations.

As it turns out, this decomposed response reflects contributions from both velocity and density profiles. The fundamental (barotropic) mode is equivalent to the vertically-averaged component of the motion and reflects the pressure gradients associated with free surface elevation (since those gradients are constant with depth). The higher (baroclinic) modes are associated with components of the vertical density profile and do not couple with surface elevation. As a result, the surface boundary condition for these higher order modes is that of a rigid lid, as adopted from *http://csep1.phy.ornl.gov/CSEP/OM/NODE5.html.*

Although stratification of the water column is likely to play a significant role in the formation and subsequent evolution of open ocean fronts, the experimental arrangement employed in this study gave precedence to analysis of the zeroth-order mode. By consideration of barotropic dynamics alone, ease of model implementation and control was readily achieved. Study of isopycnic (constant density) fluid flow with lateral current shear also allowed for enhanced analogy to related boundary layer problems. Finally, this choice granted facility to study the effect of shear surface dynamics on fluid behavior in the water column – irrespective of the effects of density.

All fluids studies were performed using a one-meter diameter tank, secured atop a rotating platform; the geometry of the experimental setup is depicted in Figure 1. As seen, the table consists of 20 slip rings, allowing for electronic connections while the table is rotating. The rotation rate of the table was controlled via an external control panel, and could be adjusted to within one one-thousandth radians per second for velocities between 0.2 and 10 rad/sec. Capable of maintaining constant rotation to within 10^{-3} radians per second, the apparatus allowed for robust control of velocity-sensitive experiments.

To create the shear region, the tank was designed with a false bottom, consisting of an outer ring fixed to the table and an inner disc extending approximately half the diameter of the table, centered about the table's axis of rotation. This inner disc was gear-driven by a 0-90 Volt DC motor, allowing for velocity control relative to that of table. For stability studies, the rotation sense of this disc could be selected prior to experimentation.

The entire apparatus was equipped with wireless communication capability, in order to transmit video from the table and to remotely control the fluids

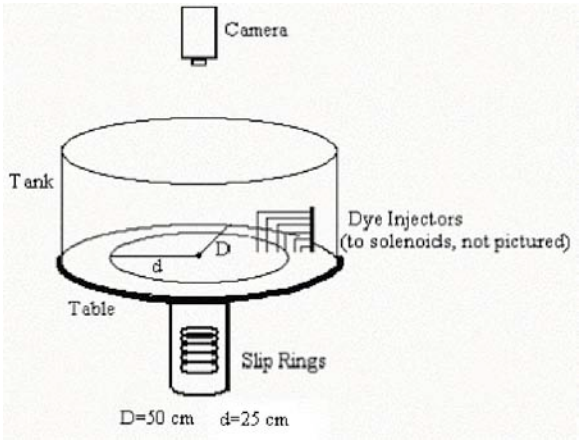

Figure 1. Schematic of rotating table employed in shear experiments. The entire table, of radius D, was made to rotate at a constant rate Ω. An inner disc (radius d) inserted into the bottom of the tank could be made to rotate at a rate ω relative to Ω. This difference in velocities served to create the shear region. Experiments were sampled using a VHS camera positioned in the rotating frame of the table (i.e., rotating at rate Ω). Fluids behavior was visualized via injection of neutrally buoyant dye spheres.

visualization methods. Images of the fluid were acquired using a VHS digital camcorder positioned axially above the table center. Attached to the table's frame, the camera was made to rotate with the table. When set to record, the video signal was sent to a desktop computer where a LabVIEW capture sequence programmatically acquired and saved bitmap images at a predefined rate. Here, resolution of 640 by 480 pixels per image could be achieved. Streaming video from the rotating frame was also sent to a VCR, allowing for reproduction of the real time signal.

Neutrally buoyant dye served as the medium for fluid dynamics visualization. The mechanical arrangement consisted of six jets inserted into the water column, straddling the region between the inner and outer disc of the false bottom. Six banks supplying three different colors of dye were fed into each of these injectors, with red dye routed to the 1st and 4th jets, blue dye to the 2nd and 5th jets, and green dye to the 3rd and 6th jets – the 1st jet corresponding to the innermost injector, and the 6th being the closest to the periphery of the tank. Solenoid valves attached below the dye banks provided for flow control. Note that the dye had to be neutrally buoyant so that only dynamics in the water-column were observed. Had the dye been too heavy or too light, it would have become entrenched in the Ekman layer – a region where fluid behavior is governed by dynamics completely separate from the mean water-column behavior.

A LabVIEW program was developed to control the voltage sent to an electro-mechanical relay, which in turn regulated the voltage sent to the solenoid valves. The program was designed such that dye injection for each jet could be rapidly turned on and off at a user-defined rate. With this switching technique, dye was injected into the system in discrete droplets, allowing

for an inexpensive and effective adaptation of particle imaging velocimetry methods.

3. Simulation and Analysis Techniques

As suggested by the experimental apparatus, all fluids studies were performed within the rotating frame of the table. The tank was filled with a 4 cm water column, covered with a lid to evade the effects of wind-stress, and made to rotate at a rate of 1.611 rad/sec in the counter-clockwise sense. In establishing the processes responsible for frontal formation and evolution, counter-clockwise rotation allowed for more ready analogy to Northern-Hemispheric oceans. Likewise, use of a 4-cm water column enhanced the observation of frontal processes as they originated from the base of the tank throughout spin-up.

In order to ensure a uniform distribution of dye around the frontal region, dye was injected into the system throughout the spin-up. Preliminary analyses indicated that spin up of a fluid contained in a cylindrical tank to solid-body rotation follows an exponential; for a 4-cm water column after 5 minutes of rotation, this function is given by:

$$\theta(t) = 320(1-e^{-t/72})$$

where θ denotes the angle evolution of a fluid parcel from its initial position and t denotes time. As this relationship suggests, by 6 minutes and 12 seconds into the spin-up the fluid volume is within thirty percent of attaining solid-body rotation.

To allow for even spacing between the dye droplets, this exponential function was adapted to govern the dye injection rate. Accordingly, as the fluid volume approached solid body rotation, dye was injected at a lower frequency than during the initial stages of spin-up. While mean dye bead diameter was on the order of 5mm, mean separation between droplets averaged approximately 10 mm.

Upon attaining solid body rotation, the inner disc was made to rotate at a rate of one revolution every 12 minutes (0.0087 rad/sec) relative to the table. Correspondingly, the image capture sequence was made to snap images of the resultant shear dynamics once per second. It is evident that it is the *relative* difference in velocities responsible for creation of the shear region. To this end, rotation of the table prior to disc spin-up may seem superfluous. The experimental model employed in this study, however, considered contributions from the barotropic mode alone. Thus, the model contributions arose only from the vertically averaged component of the motion. Put otherwise, it became imperative to have as little variation of the velocity field in the direction parallel to the axis of rotation as possible. According to the Taylor-Proudman theorem, this is guaranteed only for geostrophic flow of a rotating fluid with constant density; i.e., there must be a balance of the Coriolis force with the pressure gradient

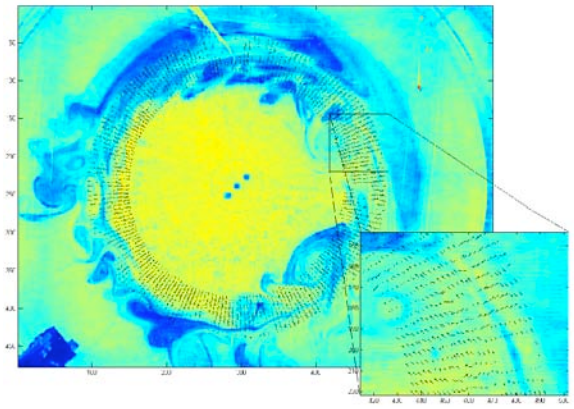

Figure 2. MATLAB generated image of a steady-state frontal vector field plotted over the blue color plane, y[0 460], x[0 640]. As seen in the enlarged region, a hint of divergence is observed over the frontal boundary. As will be discussed in section VI, this divergence is due to Ekman transport phenomena.

(including Taylor columns), this theorem asserts that both the inner disc and the outer disc must be made to rotate to obtain a controlled shear region.

Data analysis was performed using a direct cross-correlation (DCC) algorithm implemented in MATLAB. The algorithm was designed to consider an eight centimeter band centered about the disc radius. Velocity fields were obtained for images time-separated by 3 seconds. In cylindrical coordinates, the algorithm achieved a resolution of 1 pixel (0.135 cm) in the radial direction, stepping by $\pi/100$ degrees in the theta direction. To filter noise, cross-correlations were performed for each of the three image color planes (namely, red, green, and blue). The DCC results at a given point were discarded if the maximum difference between the velocities obtained from the three color planes exceeded the set speed and angle thresholds of 0.33 cm/sec and $\pi/6$ degrees, respectively. Otherwise, the resultant vectors at a point were averaged and saved to produce vector fields such as the one seen in Figure 2. Note that while DCC methods can be both time and processor-intensive, the algorithm avoids the peak-locking effect arising from fast-Fourier transform cross-correlation methods. Thus DCC methods highly reduce the degree of numerical error in the velocity profiles.

Velocity estimates were obtained for the 2700 images acquired over each 75-minute experiment. Visualization of shear formation was achieved by the sequential loading of each velocity field into a movie. Bin stacking and averaging was used to analyze and quantify the azimuthal and radial velocity components. Decomposition of the resultant velocity profiles allowed for characterization of the lateral shear region as it developed and matured.

4. Theoretical Formulation

As in any physical process, fundamental conservation laws must be obeyed; frontal flow phenomena is of no

exception. For an incompressible Newtonian flow with constant transport properties, the conservation laws are expressed

$$\text{Continuity (Conservation of Mass): } \nabla \cdot \mathbf{V} = 0$$

$$\text{Momentum: } \rho \frac{D\mathbf{V}}{Dt} = \rho \mathbf{g} - \nabla p + \mu \nabla^2 \mathbf{V}$$

$$\text{Energy: } \tilde{n} c_p \frac{DT}{Dt} = k \nabla^2 T + \Phi$$

where p is defined as the total hydrostatic pressure, $p+\rho gz$. To be sure, a theoretical formulation of the transition from turbulence to an established shear region is not readily developed. However, used in conjunction with an analysis of free surface elevation, these laws provide a basis for understanding steady-state shear.

By balance of the centripetal force with gravity, it can be shown that there is a parabolic dependence of depth on radius for a fluid in rigid body rotation in a cylindrical tank. For a fluid volume rotating at rate ω, this relationship is given by

$$y(r) = r^2 \omega^2 / (2g)$$

where, according to the said experimental arrangement, $0\text{cm} \le r \le 50\text{cm}$. Employing continuity (conservation of volume), the surface depth h at the center of the tank is found to be

$$h = H - R^2 \omega^2 / (4g)$$

where H denotes the initial depth of the fluid and R denotes the radius of the tank. Thus, the free surface contour $\eta(r)$ may be expressed as

$$\eta(r) = h + y(r)$$

homogeneous parabolic structure is perturbed, however, by rotation of the inner disc. Considering the disc to be rotating at a rate Ω relative to the table, the general form of the surface structure inside the disc is given by

$$y_i(r_i) = r_i^2(\omega + \Omega)^2 / (2g)$$

with r_i constrained by $0 \text{ cm} \le r_i \le 26.4 \text{ cm}$. If the rotation of the table were to be disregarded, the total volume of fluid above the disc would be expressed

$$V_T = \pi R_i^4 (\omega + \Omega)^2 / (4g) \qquad (1)$$

where R_i denotes the disc radius. Similarly, if rotation of the disc were disregarded, (i.e., for a uniform table rotation rate of ω), the total volume of fluid above the inner disc would be given by

$$V_i = \pi R_i^2 * h + \pi R_i^4 \omega^2 / (4g). \qquad (2)$$

Therefore, as suggested by the physical implications of (1) and (2), the surface depth h_i at the center of the tank must be

$$h_i = (V_i - V_T) / (\pi R_i^2)$$

in the presence of an established shear region. It follows that the free surface contour η_i may be expressed as:

$$\eta_i(r_i) = h_i + y_i(r_i).$$

If Ω is positive– as is the case when modeling a stable front – this contour will contain a larger first derivative (steeper slope) than $\eta(r)$ (see Figure 3, blue curve). Thus, in accord with anticipated frontal boundary layer characteristics, a convergence of fluid will be observed above the disc radius. Setting ω = 1.611 rad/sec and Ω = 0.0087 rad/sec, this steady-state dichotomy near the disc edge is only of order 0.005 cm. Nevertheless, such surface structure has a significant effect on water column behavior.

Figure 4 illustrates an exaggerated cross section of one possible manifestation of the theoretically predicted surface structure, with radius increasing to the right and positive theta defined into the page. Inside the disc, fluid motion can be solved for by direct application of equilibrium force calculations. As linear fluids theory asserts, a parcel within a mature shear region will exist in geostrophic equilibrium, exhibiting a balance of the pressure gradient force $\rho g(\partial\eta/\partial r,0)$ with the Coriolis force $\rho g f$. The parcel will also be influenced by the

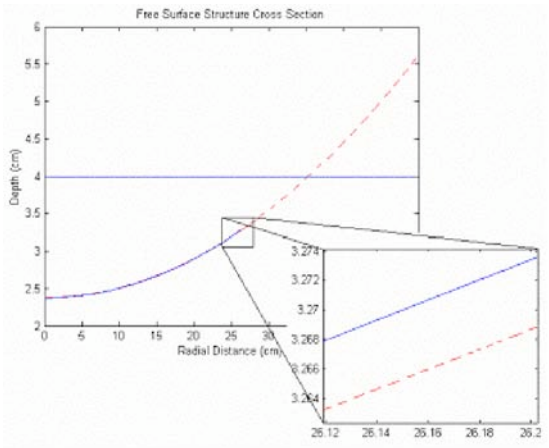

Figure 3. Numerical model illustrating the spin-up dynamics of the free fluid surface. Before spin-up of the inner disc, the surface attains a homogeneous parabolic structure, as illustrated by the red curve. Once the disc has been turned on, however, and the fluid within has achieved its own steady state, another parabola is observed within the disc radius (blue curve). If Ω>0, this parabola will have a steeper slope, resulting in a frontal convergence height on the order of 0.005 cm.

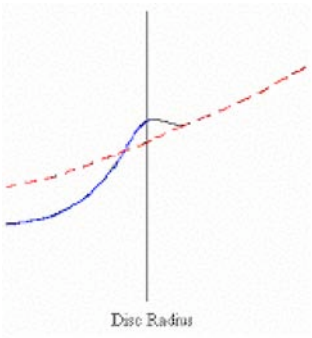

Figure 4. An exaggerated cross section of one possible manifestation of the theoretically predicted surface structure, with radius increasing to the right and positive theta defined into the page.

centripetal force $\rho v/r$ and lateral and bottom friction, f_L and f_B.

Therefore, in the radial direction, equilibrium force balance yields:

$$\rho \frac{v_\theta^2}{r} + \rho v_\theta f = \rho g \frac{\partial \eta}{\partial r} + f_{Br} + f_{Lr}$$

Likewise, in the azimuthal direction,

$$\rho u_r f = -\rho g \frac{\partial \eta}{\partial \theta} + f_{B\theta} + f_{L\theta}$$

Note that while the computed velocities are obtained only from flow in the water column, bottom friction can be ignored. Because of azimuthal symmetry, lateral friction in the radial direction f_{Lr} can also be set to zero. Moreover, since the pressure gradient force depends on the change in surface elevation – which is azimuthally constant – $-\rho g(\partial\eta/\partial r) = 0$.

Solving the equations of motion under these assumptions, the azimuthal and radial components of the velocity inside the disc are found to be, respectively,

$$V_\theta = \Omega r$$

$$u_r = 0.$$

Solving for predicted fluid motion outside the disc edge, however, presents a challenge. While fluid velocity away from the disc edge ought to be very nearly in solid body rotation, the matching of surface structure boundaries just over the disc edge could assume one of many possible forms (e.g., Fig. 4). Another possibility, for example, includes a depression in surface structure for the entire inner region and a bulge for the outer region, with no decrease in the surface height near the disc edge. It thus becomes difficult to form an accurate conceptualization of fluid flow. Even if reasonable approximations could be made, independent solution of fluid behavior in each region would not elucidate frontal dynamics at the disc edge. Accordingly, the complete velocity profile across all radii, $0\text{cm} \le r \le 50\text{cm}$, would require identification of the appropriate boundary conditions. These include equality of shear stress at the interface, kinematic equality (i.e., $v_{\_1} = v_{\_2}$ and $u_{r1} = u_{r2}$ at the interface), and asymptotic approach to the two stream velocities [Lock, 1951]. In this realm of shear-driven, rotational viscous fluid flow, it becomes essential to concede to an empirical approach.

5. Results

Throughout the study, data were collected for experimental environments considering flow in both stable and unstable velocity-driven shear regions. A reference to Figures 5 through 8 provides for quantification of the observed flow phenomena. Steady state results are presented in Figures 5 and 6; frontal spin-up analysis and simulation is depicted in Figures 7 and 8.

The velocity profiles obtained from stable steady state shear studies are illustrated in Figure 5. Both figures plot the results of bin averaging over 7 sets of 25 images, all images taken after 15 hours of the table and disc rotating in the same sense, i.e., both counter-clockwise. Note that this direction is defined as the direction of positive velocity.

As seen in Figure 5, the average radial velocity component plotted as a function of radial distance is approximately 0. The azimuthal velocity profile, however, reveals some interesting properties. As expected, the fluid within the disc is in solid body rotation (blue line, slope Ω) from 0 to 23 centimeters; within a centimeter of the disc edge, however, the velocity of the fluid becomes slower than Ω_{disc}. This trend continues up through 26 centimeters, where the fluid motion reverses direction – no longer in direct correlation with the rotation sense of the table. In this band of clockwise rotation, the velocity of the fluid steadily increases in magnitude from 0cm/sec to 0.025 cm/sec. By 26.5cm, though, the velocity of the fluid has again decreased in magnitude, approaching the steady state velocity of the table (here, 0, since results are obtained from the rotating frame).

The figure further reveals that the half-maximum of the velocity profile occurs at the disc radius. Given that the profile local maxima and minima occur within 1 cm on either side of the disc edge, such results suggest the frontal boundary layer (viscous shear layer) to be of order 2 centimeters. Studies of unstable steady state shear reveal how this spatial extent relates to the relative direction of fluid velocity.

Figure 6 plots the average of the v steady state shear results obtained from the disc rotating in the opposite sense of the table (i.e., $v_{disc} = \Omega - \Omega$). Note that the average radial velocity component was again found to be zero, exhibiting similar characteristics to those observed in the stable steady state u_{rad} profile (see Fig. 5). As in the stable steady state case, the fluid motion

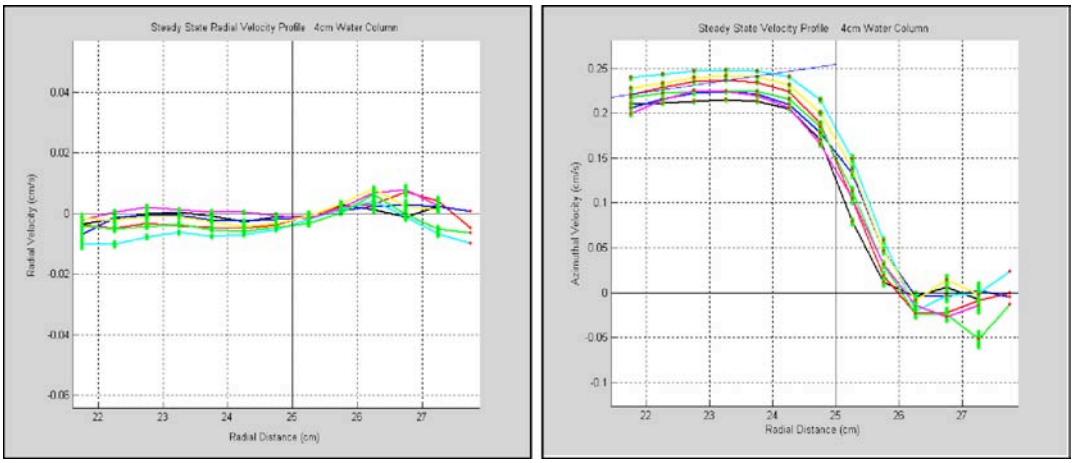

Figure 5. The radial (left) and azimuthal (right) velocity profiles plotted as a function of radial distance for an established shear region. Both figures represent the results of bin averaging over 7 sets of 25 images, each image taken after15 hours of the table and disc spinning.

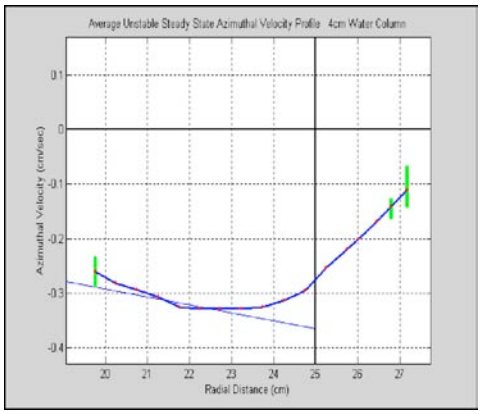

Figure 6. Average unstable steady state azimuthal velocity component plotted as a function of radial distance. Results here were obtained by averaging over a bin average of 7 sets of 25 images, each image taken after 15 hours of the disc and table rotating in opposite directions.

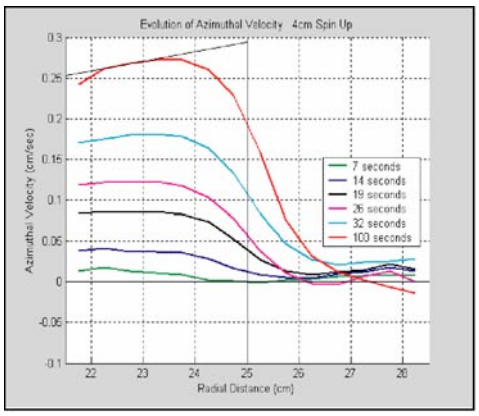

Figure 7. Illustratation of the evolution of the disc spin-up process, considering time frames 7, 14, 19, 26, 32, and 100 seconds into the spin-up. As seen, by 100 seconds, the front has nearly achieved steady state.

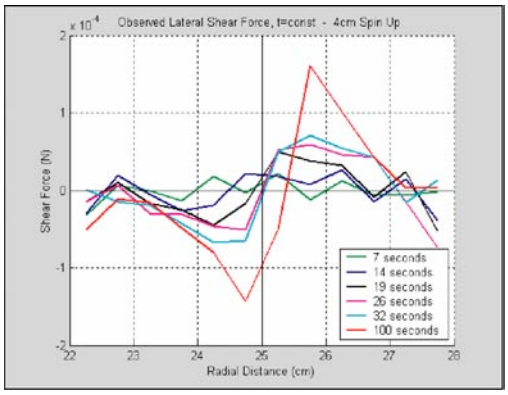

Figure 8 The observed lateral shear force plotted as a function of radius for a given time. Note the y scale factor of 10^{-4}.

approximates solid body rotation for most inner radii, with the magnitude of the velocity steadily decreasing as the disc edge is approached. Unlike the stable frontal results, however, no crossover from positive to negative velocity is observed. Rather, the velocity profile steadily decreases to 0, assuming a rate observably slower than that of the stable shear profile.

This diffuse velocity profile is attributable to the system response to disturbances. Consider a perturbation of the mean flow present in a *stable* frontal region. In the bottom boundary layer, frictional forces are of comparable magnitudes to the Coriolis and pressure gradient forces. Therefore, geostrophic equilibrium alone can no longer be used to dictate fluid behavior, and Ekman's transport theorem must be employed.

Examining the bottom boundary layer inside the disc, it is found that fluid will move slower than the disc because of friction. According to Ekman, the net fluid motion in this region must be inward – oriented 90 degrees to the left of fluid flow. Now consider fluid flow outside the disc edge, where fluid is moving slower

than the table and in the opposite direction (see Figure 5). Applying Ekman, it is found that net transport will be towards the periphery of the table – 90 degrees to the right of fluid flow. Therefore, in this bottom boundary layer, there is a net divergence of fluid across the disc edge.

By continuity, there must then be a net convergence of fluid in the water column. Suggesting a restoring force, any perturbation of the mean flow will be restored to equilibrium by this convergence of fluid across the shear layer.

To the contrary, an unstable steady state shear region is highly sensitive to even the slightest perturbations. Following the same argument employed in the stable shear region, it can be shown that there is a net convergence of fluid in the bottom boundary layer. Therefore, by continuity, there will be a net divergence of fluid across the front. This divergence can be further demonstrated by simulation of the free surface dynamics. Those methods developed in section IV are directly applicable, substituting in □ – □ for the disc rotation. Since fluid is continuously forced away from the shear boundary, it is subject to destabilizing forces that serve to enhance system perturbations. As a result, meanders of the high shear region will tend to grow on each side of the disc edge; as in Figure 6, a diffuse profile is the necessary result of averaging over all such velocities.

Thus considered, the probability of finding a well defined shear region upon averaging the vertical velocity profile is greatly reduced. As Figure 6 indicates, the viscous shear layer is of order 2 centimeters inside the disc radius, and of indefinite extent beyond 25 centimeters. Certainly, study of unstable frontal boundaries does not independently elucidate shear flow dynamics; however, it does serve as a basis for understanding how the viscous shear layer develops throughout frontal evolution.

Figure 7 plots the azimuthal velocity component as a function of radius for discrete times into the (stable) spin-up process. As seen, the velocity profile steadily evolves from 0cm/sec to steady state. Note however that it is not until 100 seconds into the spin up that the flip in the velocity profile becomes evident. In fact, in the beginning stages of spin-up, the profile bears resemblance to the unstable velocity profile. While there is no indication of a divergent water column (as in the unstable shear layer), this spread profile reflects the presence of turbulence. Preliminary analysis using a MATLAB movie of vector field development indicated discrete turbulent eddy formation around the disc edge. Accordingly, these eddies may be responsible for the energy transport into the mean flow.

The second derivative of v with respect to radius gives the lateral shear. In polar coordinates, lateral shear is given by

$$\square_{\square r} = r\frac{\partial}{\partial r}\left(\frac{u_{\square}}{r}\right) + \frac{1}{r}\frac{\partial u_r}{\partial \square}$$

Figure 8 plots the shearing force as a function of radial distance for discrete times into the spin-up. As seen, there is a steady build-up of shear within 1cm to each side of the disc radius. As the magnitude of shear evolves with time, the point of zero shear appears to drift from inside the disc (19 seconds) to directly over the disc edge (26 through 32 seconds). By 100 seconds, the shearing force has peaked at $1.4\text{x}10^{-4}$ N inside the disc radius (24.75cm) and $1.6\text{x}10^{-4}$ N outside the disc radius (25.75cm); the point of zero shear has also shifted to 25.25 centimeters. Interestingly, this is the time the flip in the velocity profile is observed.

According to Rayleigh's principle, an inflection point in the velocity profile (i.e., a point where $v_{\_}''(r) = 0$) is a necessary condition for instability. Applied to the results of Figure 8, it is observed that a possible instability is present directly over the disc edge throughout the mid-stages of spin-up. As the shear region matures, however, this instability shifts outward, corresponding more closely with the region of zero azimuthal velocity.

6. Discussion

As the above data suggest, there are of number of features associated with shear flow that call for attention. In particular, the narrow (2-cm) band of clockwise rotation outside the disc edge suggests some interesting results and raises a number of questions.

Unfortunately, the limits imposed by computational time did not allow for analysis of the principal frontal dynamics between 32 and 100 seconds. Further investigation would be required to determine how this band of clockwise rotation is generated. Referring to Figure 7, it appears there is a hint of clockwise rotation after 26 seconds; still, this region does not formally develop until 100 seconds after spin up. Even at that time, the transition from positive to negative velocity occurs 2 centimeters outside the disc radius – one centimeter beyond the flip observed after 15 hours of both the table and disc spinning.

In future studies, enhanced attention should also be given to analysis of the flow dynamics associated with the spin up of the stable frontal boundary layer. While eddies were observed in a preliminary study of the vector fields, the probability density of finding an eddy in a given region is currently undetermined. Furthermore, it remains to be seen whether these eddies are present in the steady state front. The results of such study could lend an entirely unique interpretation to the above found flow dynamics. The applicability of the study to oceanic phenomena would also benefit from consideration of the higher order baroclinic modes.

Thus, at this stage, one may only speculate on the dynamics responsible for governing and maintaining the shear flow observed in this study. Nonetheless, this does not discredit the utility and applicability of the analysis that has been performed.

In fact, the study at present reveals marked similarity to satellite observed phenomena of mesoscale eddies (current-rings) spawned by the Gulf Stream [Cornillon

and Evans, 1986]. Referred to as 'warm outbreaks', these eddies are associated with instabilities of the southern edge of the Gulf Stream at points of maximum cyclonic curvature. The typical radii of such outbreaks are of order 50 km, while maximum fluid velocities have been observed to be in excess of 50 cm/sec.

It has been found that mean flow inside warm outbreaks is anticyclonic (clockwise). However, there has been further evidence of a 2-km wide jet flowing cyclonically (counter-clockwise) around this inner region. While velocity similitude to this study's localized table experiments has not been verified, the length scale similarity is remarkably striking. It is known that mesoscale eddies assume an important role in oceanic transport phenomena. It is still unclear however how they interact with the mean flow and feed back into the general large scale circulation of the ocean. While additional empirical investigation of shear flow dynamics is required, the results obtained thus far may provide a foundation for resolving these and related boundary layer phenomena.

7. Conclusions

Perhaps only few other phenomena can generate as much deliberation over or as much insight into the fundamental nature of fluids behavior as shear flow. Indeed, shear flow represents a dynamic and novel domain that has only in recent years begun to be understood. While the defining characteristics of lateral shear are well constrained, the dynamics governing frontal formation and evolution remain unclear. Moreover, in recent years, there has been insufficient evidence – both theoretical and empirical – to comprehend the transition from turbulence to an established front. And yet, an understanding of these dynamics enhances frontal studies as applied to both oceanic processes and fluids applications in general.

As seen in this survey, empirical studies performed in a rotating table provide a powerful and straightforward foundation for understanding shear flow formation and evolution. Results were collected for both stable and unstable fronts, and gave consideration to the dynamics responsible for shear development throughout spin-up. Most notably, in steady state, the azimuthal velocity component was found to exhibit a flip, indicating a reverse of fluid direction across the boundary layer. Spin-up results indicated that this flip occurs approximately 100 seconds after disk rotation. At that time, the lateral shear was found to peak about 1 cm both inside and outside the disc edge, suggesting a shear layer on the order of 2cm.

At present, there is insufficient analytical development to *a priori* justify the dynamic balance giving rise to and sustaining the observed boundary-layer behavior. Nevertheless, the results obtained do validate phenomena observed in the warm outbreaks of the Gulf Stream. And, as the foundation of shear-driven dynamics continues to develop, we may well confront some of the most interesting – if not unanticipated – features of viscous fluid flow.

ACKNOWLEDGEMENTS. **In developing this work, I have benefited from numerous conversations with friends and colleagues. Many thanks to Dr. Peter C. Cornillon for fostering an appreciation of fundamental fluids theory, Michael Sutherland for unconditional assistance throughout this summer, and Rob Pockalny for providing this research opportunity. I am also indebted to Kim Carey and Rhonda Kenny for coordinating the SURFO experience, and to all the SURFOs for making the experience such a memorable one. A heartfelt thank-you is addressed to George and Sandra Dionne and to Nhat Vu for support, insight, and wit. This work was further supported by the National Science Foundation. Laboratory equipment was funded by the National Aeronautics and Space Administration, grant no. NAG 53736.**

References

P. Cornillon and Z. Shan, On the Characteristics of Subtropical Fronts in the North Atlantic, 2000

N.J. Balmforth and P.J. Morrison, Hamiltonian Description of Shear Flow, 1999

P. Cornillon and D. Evans, Warm Outbreaks of the Gulf Stream into the Sargasso Sea, 1986

I.G. Currie, Fundamental Mechanics of Fluids, Second Edition, 1993

F. White, Viscous Fluid Flow, Second Edition, 1991

A.E.Gill, Atmosphere-Ocean Dynamics, 1982

http://csep1.phy.ornl.gov/CSEP/OM/

Effects of Moisture on Numerical Simulations of Atmospheric Boundary Layer Roll Vortices in Hurricane Conditions

Jeffrey Gall,[1] and Isaac Ginis

Graduate School of Oceanography, University of Rhode Island, Narragansett, Rhode Island

Abstract. This study uses a 3-D high-resolution boundary layer model to investigate the effects of moisture on the development, strength, intensity, and location of roll vortices in hurricane like conditions. Six model experiments were conducted, each with a different initial moisture profile. The two main moisture sources in the model are an initial linear moisture profile and air-sea moisture fluxes. Moisture model experiments clearly indicate the significance moisture plays in atmospheric boundary layer (BL) roll vortices. The strength of the atmospheric BL roll vortices increases as the overall amount of moisture increases. Mechanical forces are the main source of energy production in the BL when large amounts of initial moisture are present, while energy production through buoyant forces become more important when little initial moisture is present. The roll wind speeds and Monin-Obukhov length ratios agree with previous observations and studies. The stream function values, however, are much larger than previous models indicate.

1. Introduction

Radarsat synthetic aperture radar (SAR) images obtained in Hurricanes Bonnie, Danielle, Georges, and Mitch revealed the presences of roll vortices in the boundary layer (Katsaros et. al. 2000). Roll vortices are extremely important because they can greatly influence the magnitude of certain fluxes (e.g. moisture, momentum, and heat) in the BL. To simulate these roll vortices in hurricane-like conditions, a 3-D large eddy simulation model was used with initial conditions that are indicative of hurricanes. This study looks at how the amount of moisture in the initial conditions as well as air-sea moisture fluxes at the surface of the boundary layer effects roll vortices.

1.1 Background

In an observational study of roll vortices during cold air outbreaks by LeMone (1973), quantitative descriptions of the rolls were produced. Roll vortices were observed and measured 4 different times over the tower and 8 different cases of roll vortices were studied using aircraft. Some results from this study were that horizontal winds within the boundary layer ranged between 8-15 ms-1 and the boundary layer height varied from .6 km to 2.2 km. A maximum value of uroll =1.2 ms-1, where uroll is the horizontal roll wind speed, was observed and the location of the maximum u-component wind of the rolls was .07z, where z is the BL height. The ratio of uroll to Vg was approximately .1. The maximum vertical velocity was 1.0 ms-1 and it occurred at .33z. Brown (1980) calculated theoretical secondary flow parameters including stream function, and determined that the maximum stream function within a roll was approximately .1 m2s-1 (see Fig. 1). Both Brown and LeMone determined that the major terms in roll maintenance are energy production from wind shear (mechanical forces) and buoyancy.

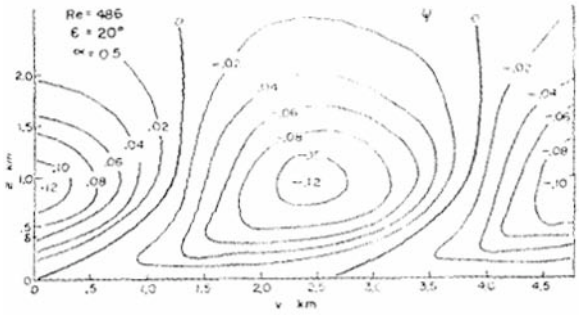

Figure 1. Stream function contours from a roll cross-section taken from Brown (1980).

The effects of latent heat release and non-precipitating clouds with cloud-top cooling on roll development are discussed differently. Mason (1985) used a finite difference model to investigate the neutral planetary boundary layer. Mason did not find any substantial changes in roll dynamics considering simulations with and without latent heat release and non-precipitating clouds with cloud-top cooling. Sykes et al. (1988) found that the aspect ratio (the ratio of wavelength to height of the rolls) increased to 10 when latent heat release was included in the model. Dry model experiments produced aspect rations ranging between 1 and 3. The aforementioned models, however, have initial and boundary conditions based on typical cold air outbreak situations.

1.2 Monin-Obukhov Length Ratio (-z/L)

In this study, z equals the boundary layer height and is assumed to be 2 km. L is the Monin-Obukhov length and is defined as:

$$L = \frac{u_*^3 \overline{T}}{kg\overline{w'T'}} \quad (1)$$

[1]Now at Cornell University, Ithaca, NY, 14853, USA.

Where u_* is the frictional velocity, $\overline{T}$ is the background temperature, k is the VonKarman constant, and g is gravitational acceleration. The Monin-Obukhov length is a parameter with a dimension of length, and gives a relation between factors characterizing dynami
c, thermal and buoyant processes. As the value of L increases, the height to which buoyant forces prevail increases. Small values of L indicate that mechanical forces such as wind shear are more significant in the BL.

There have been numerous other studies in which the term -z/L has been used as a criterion for roll formation. In three-dimensional boundary layer model experiments by Deardorff (1976), he found that rolls form only for -z/L=0, -z/L=1.5, and somewhat form for -z/L = 4.5. According to Deardorff, a critical value of -z/L=25 separates the regime of roll convection from that of cellular convection. LeMone (1973) found in an observational study that rolls formed in near-neutral conditions with -z/L ranging from 3 to 10. Coleman (1990) observed that organized vortices were present when .4<-z/L<2.9 for moderate unstable stratification. As -z/L approaches 0, inflection point instability dominates and thermal instabilities become less important. Mason (1983) examined roll development for different ratios and found that for -z/L > 0.8, rolls are mainly driven by buoyancy. D. Etling and R.A. Brown (1993) found that z/L is usually less negative for moderate winds and moderate surface heating and more negative for low winds and strong heating. In an observational study by Weckwerth (1999), it was found that as the term -z/L increased, the BL became more convectively unstable and the rolls broke apart and dissipated. When z/L =-2 (near neutral conditions), roll vortices are assumed to be due to the so-called inflection point instability which can operate whenever Ekman layer turning is imposed on the BL, even under neutral stratification. The value of the mean boundary layer wind or wind shear within the boundary layer appeared to have no effect on the formation of roll vortices. Rather, if the wind was low (mean boundary layer winds <3ms-1 and near surface winds <2ms-1) during roll occurrences, rolls evolved into open cells. Conversely, if wind speeds were high, the rolls broke into random convective elements. Different types of instability that may be the basis for roll formation include inflection point instability, parallel instability, and convective instability.

1.3 3-D Large Eddy Simulation Model

In order to resolve roll vortices in the PBL a very high resolution large eddy simulation (LES) model is required. However, the utilization of a fully 3-D LES model for investigation of large eddy effects on large-scale processes is limited not only by serious computational problems, but also because the background flow is often prescribed in such models, so that only effects of the large-scale mean flow on the small-scale (including convection scale) processes in the BL can be considered (one way interaction).

To consider the two-way interaction (effects of the large scale flow on the convective processes and vice versa) a basic 3-D system of equations can be split into two simpler sub-systems describing the large-scale and small-scale processes, respectively (see Fig. 2). The idea of such separation, first suggested by Khain et. al. (1986), is based on the differences in the horizontal scales of the large-scale and convective motions. It was successfully used for the investigation of the trade wind boundary layer (Khain and Ingel, 1995) in the tropics.

In the present study we utilize these ideas of scale separation that imply two major assumptions. Firstly, roll vortices are in the BL are quasi-homogeneous in the direction of the mean (large-scale) wind. Secondly, the spatial scale of the large eddies (convective motions) in a vertical plane perpendicular to the mean wind is much smaller that spatial scale of variability in the along-wind direction (see Fig 3). This allows reducing the 3-D basic system of equations into two sets of 2-D equations: one for averaged values associated with the mean flow ('mean flow' equations), and another for deviations from the averaged values attributed to the convective motions perpendicular to the mean ("convective" equations).

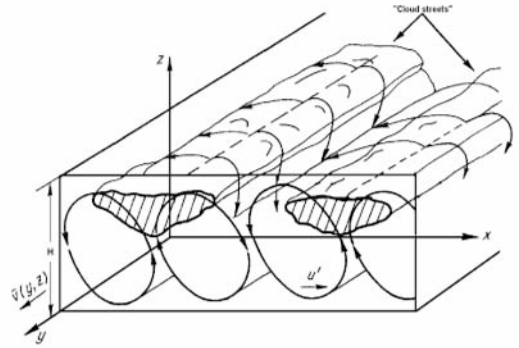

Figure 2. Schematic of secondary flow patterns associated with atmospheric boundary layer rolls simulated in this study.

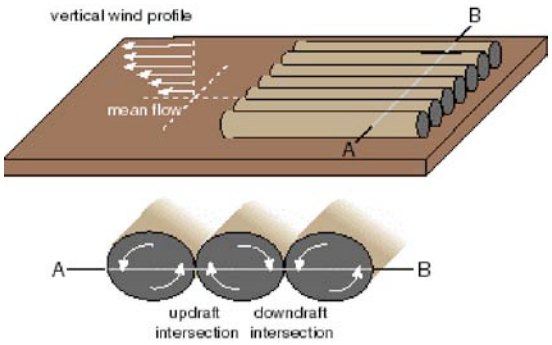

Figure 3. An illustration of the two main assumptions made in modeling atmospheric boundary layer roll vortices.

Mean flow equations:

$$\frac{\partial \bar{v}}{\partial y} + \frac{\partial \bar{w}}{\partial z} = 0 \tag{2}$$

$$\frac{\partial \bar{v}}{\partial t} + \bar{v}\frac{\partial \bar{v}}{\partial y} + \bar{w}\frac{\partial \bar{v}}{\partial z} = \overline{\frac{1}{\rho}\frac{\partial p}{\partial y}} - \frac{\partial \overline{w'v'}}{\partial z} + \nu\frac{\partial^2 \bar{v}}{\partial z^2} \tag{3}$$

$$\frac{\partial \bar{\theta}}{\partial t} + \bar{v}\frac{\partial \bar{\theta}}{\partial y} + \bar{w}\frac{\partial \bar{\theta}}{\partial z} = \frac{L}{c_p}\bar{C} - \frac{\partial \overline{w'\theta'}}{\partial z} + \kappa\frac{\partial^2 \bar{\theta}}{\partial z^2} \tag{4}$$

Convective equations:

$$\frac{\partial u_c}{\partial x} + \frac{\partial w_c}{\partial z} = 0 \tag{5}$$

$$\frac{\partial v_c}{\partial t} + u_c\frac{\partial v_c}{\partial x} + w_c\frac{\partial v_c}{\partial z} = -\frac{\partial \overline{w'v'}}{\partial z} - w_c\frac{\partial \bar{v}}{\partial z} - v_c\frac{\partial \bar{v}}{\partial y} + \nu\nabla^2 v_c \tag{6}$$

$$\frac{\partial \theta_c}{\partial t} + u_c\frac{\partial \theta_c}{\partial x} + w_c\frac{\partial \theta_c}{\partial z} = \frac{L}{c_p}C_c + \kappa\nabla^2\theta_c + \left(-\frac{\partial \overline{w'\theta'}}{\partial z} - w_c\frac{\partial \bar{\theta}}{\partial z} - w_c\frac{\partial \theta_c}{\partial z}\right) \tag{7}$$

$$\frac{\partial \zeta_c}{\partial t} + u_c\frac{\partial \zeta_c}{\partial x} + w_c\frac{\partial \zeta_c}{\partial z} = g\frac{\partial}{\partial x}\left(\frac{\theta_c}{\theta_0} + 0.61q_c - l\right) + \nu\nabla^2\zeta_c \tag{8}$$

$$\zeta = \nabla^2\psi, \quad u' = \frac{\partial \psi}{\partial z}; \; w' = \frac{\partial \psi}{\partial x} \tag{9}$$

Where $\bar{v}$ is the background horizontal wind, $\bar{w}$ is the background vertical wind, ν is the viscosity of air, θ is the potential temperature, L is the latent heat of vaporization, C_p is the specific heat, Φ is the geopotential, u_c is the convective horizontal wind, w_c is the convective vertical wind, is ζ the absolute vorticity, q_c is the convective mixing ratio, ψ is the stream function.

The interaction between the convective motions and the mean flow occurs via the convective fluxes calculated explicitly during the integration of the convective equations. The convective fluxes momentum, <w'T'>, and mixing ratio, <w'q'>, are calculated by averaging of products of corresponding deviations over the convective domain. The convective system of equations is a non-hydrostatic shallow convection system for the wind velocity components, potential temperature, mixing ration and cloud water content. Taking into account a low depth of the boundary layer clouds we assume that the clouds do not precipitate. Convective heating and cooling caused by condensation and evaporation contribute significantly to the intensity of the BL. Long-wave radiation cooling is also taken into account.

In the present set of experiments the computational domain for the convective equations has H=2 km in the vertical direction with 31 levels and 5.5 km in the x-direction with 17 grid points (Fig. 1) The mean flow domain has 200 km in the y-direction with 11 grid points. Initially, we specified idealized linear profiles of wind, potential temperature, and mixing ration that roughly correspond to hurricane conditions. At the upper boundary, the values of all variables are prescribed. At the sea surface, the momentum, heat, and moisture fluxes are calculated using the Monin-Obukhov similarity theory. The SST is set equal to 303K and the pressure near the surface is close to 1000 mb.

2. Methods

2.1 Initial Conditions

An initial linear profile of moisture is specified within the model before the mean flow equations are integrated (see Fig. 4a). Also, air –sea moisture fluxes are implemented in both the mean flow and convective sets of equations. These two components defined the general moisture scheme of the model and consequently controlled latent heat release and vertical moisture fluxes. Thus, in order to modify the moisture profile, one or both of these parameters needed to be changed.

2.2 Experimental Design

In order to reveal the effects of moisture on roll vortices, the following experiments are performed. The mean flow equations are first integrated for t=4 hours using a traditional first order turbulent scheme for the vertical transfer of heat, moisture, and momentum. For this, all convective fluxes are assumed equal to zero. After an equilibrium state is achieved (in about 4 hours), the convective equations are introduced which explicitly calculate the convective fluxes associated with roll vortices. These fluxes provide additional vertical transfer of heat, moisture, and momentum. The convective equations are integrated for t=6 hours.

2.3 Model Experiments

Six different model experiments were conducted each with a different moisture profile. Experiment 1 was the

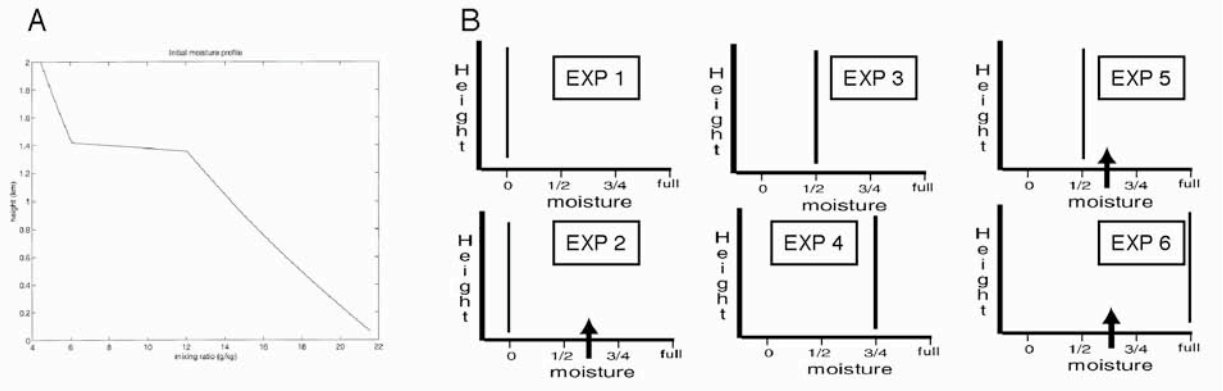

Figure 4. (a) The linear initial moisture plot used in this study. (b) Illustrations of the 6 different model experiments used in this study. The arrow indicates air-sea moisture fluxes and the dark vertical line indicates the percent of the linear initial moisture plot used.

dry case, which means that the initial mixing ratio (see Fig 4a, 4b) was set equal to zero and the air-sea moisture fluxes were turned off. Experiment 2 featured the initial mixing ratio equal to zero, but air-sea fluxes were included in both the mean flow integration as well as the convective integration. Experiment 3 had the initial mixing ratio halved, and air-sea fluxes were turned off. Experiment 4 had the initial ratio reduced by a factor of .75, and air-sea fluxes were again turned off. Experiment 5 featured the initial mixing ratio halved and included air-sea fluxes. Experiment 6 had the full initial mixing ratio profile and included air-sea moisture fluxes.

3. Results

3.1 Stream function

After completing all six model experiments, the model data was analyzed (see Fig. 5a-5f). Experiments 1 and 2 produced very similar results, experiments 3 and 4 produced similar results, and experiments 5 and 6 also produced similar results. The first quantity analyzed was stream function. These two quantities were plotted on an x-z cross-section at Y=250 km after complete integration of the mean flow and convective equations. The stream function is analogous to the gradient wind, and tends to increase as the amount of moisture increases for the 6 model experiments conducted. The rolls from experiments 1 and 2 produced extremely weak, elongated rolls. The max stream function for both experiments was 1.2 m^2s^{-1}. The height of maximum stream function was .8 km. The rolls from Experiments 3 and 4 produced 4 roll vortices. The two outside rolls were located at .25 km, which is extremely close to the surface of the BL. The max stream function for the two outside rolls was 1.6 m^2s^{-1}. The inner roll vortices were much weaker and their shape was much more circular. Inside rolls from experiment 3 were slightly weaker than the inside rolls from experiment 4. The rolls from experiments 5 and 6 were extremely well defined and circular. The max stream function for roll 5 was 12 m^2s^{-1} and was located at 1km. The maximum stream function for roll 6 was 16 m^2s^{-1} and was located at 1km. The rolls in experiments 1 and 2 are approximately 5 km apart, while the 4 rolls generated by experiments 3 and 4 are closer together with an approximate distance of 1.5 km between rolls. The rolls from experiments 5 are 2.25 km apart and the rolls from experiment 6 are 3 km apart.

3.2 Winds

The wind speeds generated by the rolls were calculated in the model. Values of vertical velocity (w_{roll}) and the u-component velocity (u_{roll}) were compared after each model run. As with stream function, the similarity between experiments 1 and 2, experiments 3 and 4, and experiments 5 and 6 held through. It appears as though the amount of moisture increased, the wind speeds of rolls increased as well. For experiments 1 and 2, the height of maximum u_{roll} was .1z (.2 km) and the maximum speed was .0036*V_g, where V_g is the overlying environmental wind speed at the location of maximum u_{roll} height. The location of maximum w_{roll} occurred at .5z (1 km), and the maximum value of vertical velocity was .6 ms^{-1}. For experiments 3 and 4, the height of maximum u_{roll} was .05z (1 km) and the value of the max was .009*V_g. The location of the w_{roll} maximum was .125z (.25 km) and the maximum vertical velocity was .8ms^{-1}. For experiments 5 and 6, the height of maximum u_{roll} was at a height of .15z (.3km) and the value of maximum wind speed was .036*V_g. The location of maximum w_{roll} was .5z (1 km) and the maximum vertical velocity was 2ms^{-1}.

3.3 Monin-Obukhov Length Ratio

Figure 6 gives the values of the ratio –z/L for each of the 6 model experiments. The x-axis is the amount of integration time of the mean flow equations. The y-axis is the value of –z/L. Model experiments 1 and 2 produced extremely similar values of L. The maximum value for experiments 1 and 2 is approximately 1.55. The maximum steady-state value for experiment 3 is

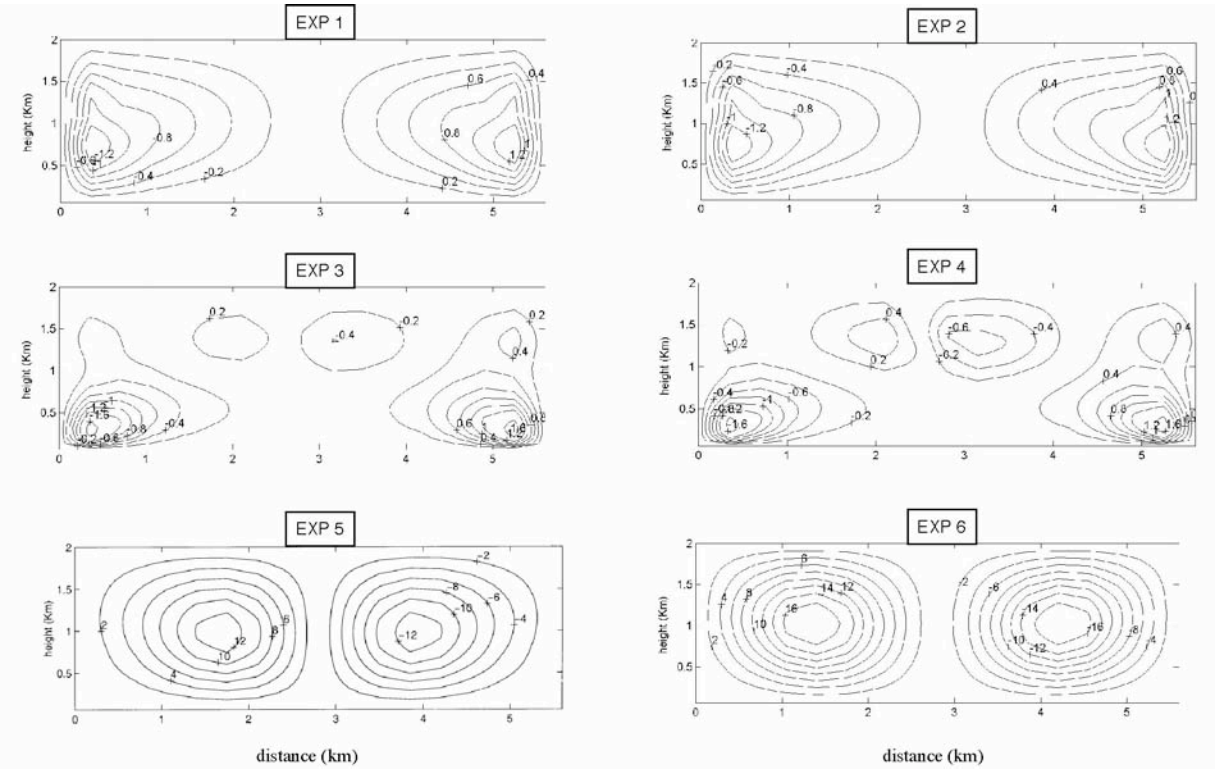

Figure 5a-f. Stream function (m^2s^{-1}) of roll vortices on a x-z cross section.

approximately 1.07 while the max value for experiment 4 produces a value of .8 for –z/L. Experiment 5, however, has a maximum steady state value of 1.05 that is extremely close to that of experiment 3. Recall that experiments 3 and 5 had the same amount of initial moisture, but experiment 5 had air-sea fluxes turned on. Experiment 6 produced a maximum steady state value of .62. Notice that experiment 1 has the greatest change between the –z/L value at .5 hours and 4 hours, while there is little change of –z/L for experiment 6 between .5 and 4 hours.

3.4 Kinetic Energy

Figure 7 contains the KE plots from each of the 6 model experiments. In this case, experiments 1 and 2, and experiments 3 and 4 produced almost the same exact plots. The x-axis is the integration time of the convective equations and the y-axis is the kinetic energy of the rolls, where the kinetic energy is defined as:

$$KE=.5u_{roll}^2 + .5v_{roll}^2 + .5w_{roll}^2 \qquad (10)$$

Experiments 1 and 2 had a maximum KE value of $3*10^6$ ms^{-2} and the time to reach steady state is between 3 and 3.5 hours. Experiments 3 and 4 had a maximum KE value of $4.05*10^6$ ms^{-2} and the steady state time in this case is greater than 4 hours. Experiment 5 had a KE max of $6.60*10^6$ ms^{-2} and it took approximately 1.75 hours to reach steady state. Experiment 6 actually had a lower KE max than experiment 5, and time it took slightly over 2 hours for experiment 6 to reach a KE steady state value.

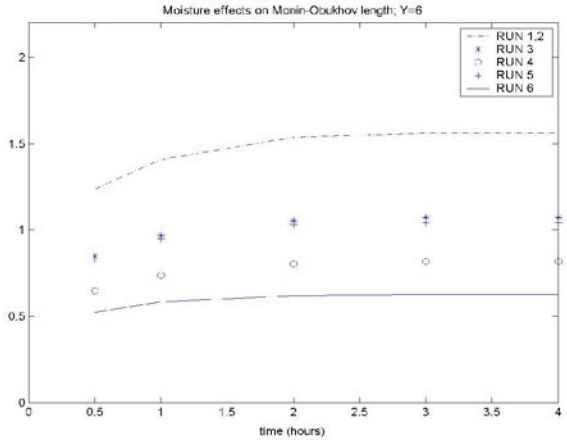

Figure 6. Comparison of the Monin-Obukhov length ratio (-z/L) for the 6 model experiments.

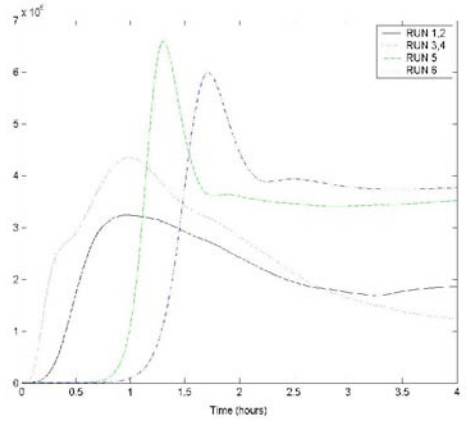

Figure 7. Comparison of the kinetic energy profiles for the 6 model experiments.

4. Discussion

The stream function is a good indicator of the strength of the roll. As the amount of moisture increased (both initial moisture and air-sea fluxes), the max stream function increased. Also, the time of maximum stream function was approximately 1 hour for experiments 1 through 4. Experiments 5 and 6 had a max stream function at 6 hours. Thus, both air-sea moisture fluxes and an initial moisture source are required for the stream function to continually strengthen and have a maximum stream function at the end of the model run. The model experiments conducted here, produce a maximum stream function that are much greater than the model experiment conducted by Brown (1980) (see Fig. 3). Brown's model, however, assumes an overlying wind of $10ms^{-1}$ and dry conditions. Thus, the stream function values which are closest to Brown's are those that have no moisture (experiments 1 and 2).

The strength of maximum u_{roll} and w_{roll} increases as both the initial moisture and air-sea moisture fluxes increase. The magnitude of u_{roll} increased from $.0036*V_g$ to $.036*V_g$ and the magnitude w_{roll} increased from $.6ms^{-1}$ to $2ms^{-1}$, with increasing moisture. When air-sea fluxes are turned off, but initial moisture is present, the location of w_{roll} and u_{roll} will be lower than if air-sea moisture fluxes were turned on. The location of u_{roll} and w_{roll} for experiments 3 and 5 are much lower than experiments 1 and 2 and experiments 5 and 6.

Although the average location and strength for the maximum u_{roll} and w_{roll} were determined by LeMone (1973) for conditions in which the average BL wind ranged between 8ms-1 and 15ms-1, the results on winds from the model agrees relatively well with LeMone's observations (Table 1). The location of maximum u_{roll} agrees very well with the .07z value LeMone gives. The location of maximum w_{roll} somewhat agrees with the observations of LeMone. Although the model experiment range is larger than with u_{roll}, LeMone's location of vertical velocity falls within the range of values generated by experiments 1 through 6. LeMone's observational vertical velocity magnitude ($1ms^{-1}$) is very close to vertical velocity outputs ($.6ms^{-1}$ – $2\ ms^{-1}$) generated by model experiments. The magnitude of u_{roll} generated by model experiments is much lower than observations made by LeMone. This is most likely due to the fact that the model had an extremely fast overlying wind.

Experiment 1 had the highest value of –z/L (1.55), while experiment 6 had the lowest value (.62). From figure 6, it can be shown that as the amount of initial moisture increased, the –z/L term decreased. Also, air-sea fluxes had little effect on the monin-obukhov length ratio. The –z/L term being >.8 for experiment 1 implies that energy production from buoyant forces is the dominant mechanism in roll formation based on the results by Mason (1983). The lower –z/L value for experiment 6 implies that energy production from mechanical forces (e.g. wind shear) is the primary mechanism in roll formation. Thus, the initial moisture amount directly effects the primary mechanism by which roll vortices in the BL form. Low amounts of initial moisture cause mechanical forces to be the primary formation mechanism, while larger amounts of initial moisture cause buoyant forces to be the primary mechanism.

The monin-obukhov length ratio results agree very well with the three-dimensional experiments conducted by Deardorff (1976). He found that rolls form for –z/L=0, -z/L=1.5, and somewhat form for –z/L=4.5. Consequently, he determined that as the –z/L term increases, roll formation becomes more disorganized. This agrees with the results from the 6 model experiments. Experiment 6 had the greatest organization and strength and had the lowest –z/L value (.62) as well. Experiment 1, however, was the most disorganized and consequently had a –z/L value of around 1.55. Coleman (1990) observed that organized roll vortices were present when .4<-z/L<2.9 for moderate unstable stratification. Results from model experiments agree with the results of Coleman in that –z/L model values fall within his predetermined range. LeMone (1973) observed that rolls formed for 3<-z/L<10 in near-neutral conditions. The range of .5<-z/L<1.5 generated from the 6 model experiments falls just below LeMone's observations.

The KE plots produced some very interesting results. When the amount of initial moisture is large and air-sea fluxes are present, the time it takes to reach maximum KE is longer than when initial moisture is smaller and air-sea fluxes are turned off. As the amount of moisture increases, the maximum value of KE increases except for experiment 6. Experiment 6 has a slightly lower max KE than does experiment 5. Experiments 1 and 2 have a higher steady state KE value than do experiments 3 and 4. Thus, the presence of initial moisture without air-sea moisture fluxes causes the rolls from experiments 3 and 4 to achieve a low steady state KE value.

	Run 1 and 2	Run 3 and 4	Run 5 and 6	LeMone
Location of u_{roll}	.1z	.05z	.15z	.07z
magnitude of u_{roll}	.0036*V_g	.009*V_g	.036*V_g	.1*V_g
location of max w_{roll}	.5z	.125z	.5z	.33z
magnitude of w_{roll}	.6 ms^{-1}	.8 ms^{-1}	2 ms^{-1}	1 ms^{-1}

Table 1. Comparison of model results of wind with observations from LeMone (1973)

5. Conclusions

Stream function, roll wind speeds and locations, monin-obukhov length ratios, and kinetic energy profiles all indicate that moisture plays an extremely important role in the development of boundary layer roll vortices. Stream function values indicate that both high amounts of initial moisture and air-sea moisture fluxes are required for strong, organized rolls to develop. The primary formation mechanism in low moisture model experiments is energy production from buoyancy, while the primary formation mechanism in high moisture model experiments is energy production from mechanical forces. Good agreement is shown between the model location of maximum uroll, the model location of maximum wroll, and the magnitude of maximum wroll with the observations of LeMone. The model, however, underestimates the magnitude of uroll when compared to LeMone's observations.

Acknowledgments. I would like to thank Dr. Ginis and Dr. Biju Thomas for all of their help and guidance in this project. I would also like to thank Robert Pockalny for assisting me with Adobe Illustrator and other technical aspects of this paper.

References

Brown, R.A., 1980: Longitudinal instabilities and secondary flows in the planetary boundary layer: A review, *Rev. Geophys. Space Phys*., **18**, 683-697.

Coleman, G.N., 1990: A numerical study of the stratified turbulent Ekman layer. *Ph D. thesis, Dep. Mechanical Engineering, Stanford University.*

Deardorff, J.W., 1976: Discussion of thermals over the sea and gull flight behavior by A.H. Woodcock. *Boundary-Layer Meteorol.* **10**, 241-246.

Katsaros, K.B., P. Vachon, P.G. Black, P.P. Dodge, and E.W. Uhlhorn, 2000: Wind fields from SAR: Could they improve our understanding of storm dynamics? *John Hopkins APL Technical Digest*, **21(1)**, 86-93.

Khain A.P., M.G. Yarmolinskaya, L. Kh. Ingel, 1986: Numerical Modeling of interaction of convective and large-scale processes in the atmospheric boundary layer with the4 formation of a temperature inversion. *Atmos. And Ocean Physics*, **22**, 987-993.

Khain A.P. and L. Kh. Ingel, 1995: Numerical modeling of interaction of a nonstationary divergent flow with convective processes in the boundary layer over the ocean. *Atmos. And Ocean Physics*, 31, 496-506.

LeMone, M. A., 1973: The structure and dynamics of horizontal roll vortices in the planetary boundary layer. *Journal of the Atmospheric Sciences*, **30**, p. 1077-1091.

Mason, P.J., 1985: A numerical study of cloud streets in the planetary boundary layer. *Boundary-Layer Meteorol.* **32**, 281-304.

Raasch, S., 1990: Numerical simulation of the development of convective boundary layer during a cold air outbreak. *Boundary-Layer Meteorol.* **52**, 349-357.

Sykes, R.I., Lewellen, W.S. and Henn, D.S., 1988: A numerical study of the development of cloud-street spacing. *J. Atmos. Sci.* **45**, 2556-2569.

Weckwerth, T.M., Horst, T.W. & Wilson, J.W., 1999: An observational study of the evolution of horizontal convective rolls, *Mon. Weather Rev*., **127**, 2160-2179.

J. S. Gall and I. Ginis, Graduate School of Oceanography, University of Rhode Island, Narragansett, RI 02882. (jsg37@cornell.edu, iginis@gso.uri.edu)

[1]Cornell University

An exploration of mixotrophy in *Dinophysis acuminata*

Emily Grason[1] and Lucie Maranda
Graduate School of Oceanography, University of Rhode Island

Abstract. Jacobson and Andersen first established mixotrophy as a nutritional strategy for the marine protist *Dinophysis acuminata* Claparède and Lachmann in 1994. In order to investigate time of feeding, integrated depth samples from Greenwich Cove were collected every two hours over two 24-h sample periods. The samples were concentrated and filtered for *D. acuminata*, and the cells were analyzed for the presence of food vacuoles using DIC microscopy. To explore the possibility of a diel cycle of feeding, frequency of appearance of food vacuoles in cells was reported as a function of time over the sample period. On June 17-18, 2002, a peak in feeding occurred at 2100h, where 26% of cells in the sample contained some form of vacuoles. This result may find application in the hitherto unsuccessful effort to fully culture *D. acuminata* for research purposes. Additionally, potential identification of D. acuminata prey has implication for trophic web dynamics. A second sample period, July 22-23 2002, yielded too few cells to enable comparison of results.

1. Introduction

The photosynthetic dinoflagellate *Dinophysis acuminata* has never been successfully maintained in culture, in spite of many efforts to investigate media of differing nutritional content (Maestrini et al. 1995). Due to the inability to keep *Dinophysis* alive over an extended period in the laboratory, little is known of the ecology of this genus. The use of natural communities introduces a high level of variability into studies and can confound results. Though *D. acuminata* has been documented to cause Diarrhetic Shellfish Poisoning events in the waters of Japan and Western Europe, the production of toxins by this species has never been proven in U.S. coastal waters, where its abundance can on occasion cause it to dominate the phytoplankton community.

Evidence of mixotrophy in *D. acuminata* has recently been observed in the form of food vacuoles among cell contents (Jacobson and Andersen 1994), suggesting a previous deficiency in understanding of *D. acuminata* nutrition. Subsequent studies have cited an inability to perceive an actual feeding event as grounds to question mixotrophy (Berland et al. 1995). However, Jacobson and Anderson (1996) demonstrated with two other dinoflagellates, *Alexandrium ostenfeldii* and *Scippsiella* spp., that feeding on the scale of a population may differ temporally. We therefore endeavored to investigate a diel pattern in feeding habits for *D. acuminata*.

2. Methods and Materials

2.1 Sample Collection

During two 24-h sample periods, June 17, and July 22, 2002, samples were collected from a public dock on Greenwich Cove, RI (41º39.5´N, 71º27´W). A 2m x .0125m PVC tube was used to obtain an integrated water column sample every two hours for a full tidal cycle (low- high-low-high-low). After volume (200-300 ml) had been recorded, the sample was filtered through a 105 _m mesh and concentrated through a 10 _m mesh via reverse filtration to a volume of ca. 25 ml. The concentrated sample was subsequently preserved in glutaraldehyde (1% final concentration). A second depth-integrated sample was taken and 15 ml was preserved in Lugol's iodine solution for *D. acuminata* cell density. Samples were labeled and refrigerated (ca. 7°C) until analysis.

Concurrent with each water sample, a YSI 600 probe was lowered to bottom (1m at low tide, 2m at high tide) at the site to acquire a temperature and salinity profile for the water column (every 0.25m).

2.2 Laboratory Analysis

Dinophysis acuminata cell counts on the unconcentrated samples were performed using a Palmer-Maloney chamber. All microscopy and imaging was performed on a Nikon Eclipse E800 light microscope at 400x. An aliquot of the concentrated samples were rinsed of glutaraldehyde using 0.45 _m filtered seawater, leaving ~5-10 ml of preserved sample for future electron microscopy analysis. The rinsed samples were transferred to 50 ml centrifuge tubes and refrigerated at 7°C. *D. acuminata* cells were examined for food vacuoles using differential interference contrast (DIC) microscopy and blue light excitation epifluorescence (Ex 450-490, DM 500, BA 515). From each sample, 200 cells were counted and categorized based on presence of vacuoles. One sample with a particularly low cell count (6/17 1500h) required centrifugation in order to increase concentration. Cells were categorized as: having no food vacuoles (Fig. 1), 1-3 food vacuoles (Fig. 2) > 3 food vacuoles, or "droplets" (Fig. 3), spherical bodies of roughly the same appearance and location as food vacuoles, but smaller in size.

Unfortunately, for the samples from the July 22-23 study, lack of time precluded the extensive analysis performed on the first study and only two samples could

[1]Now at Bowdoin College, Brunswick, ME, 04011.

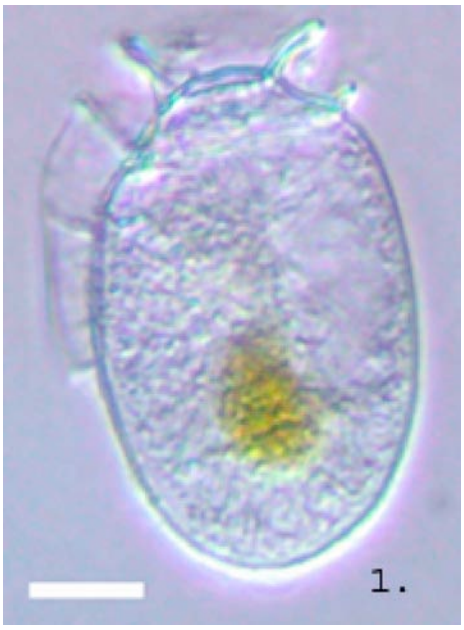

Figure 1. Live *Dinophysis acuminata* cell magnified 400x. Note contracted chloroplast. White scale bar represents 10 µm.

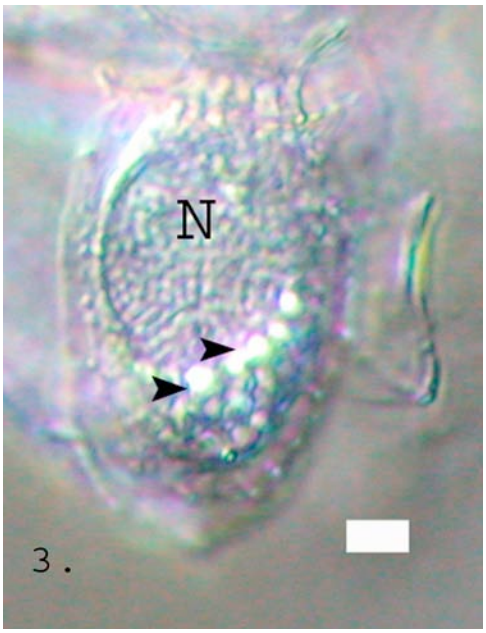

Figure 3. Preserved *acuminata* containing droplets. N-Nucleus. White scale bar represents 10 µm.

Figure 2. Preserved cell containing multiple vacuoles (white arrows) at 400x magnification. White scale bar represents 10 µm.

be analyzed, 0900h and 2100h. However, both of these sub-samples only included 50 cells.

2.3 Transmission Electron Microscopy

In order to explore the contents of the food vacuoles, we utilized thin section transmission electron microscopy. A sample was considered a good candidate for TEM if it contained a high number of cells with well-preserved food vacuoles. The glutaraldehyde fixed samples were post-fixed with 1% osmium tetroxide in buffer minus NaCl for 3 h at 4°C and dehydrated in an ethanol series. Fixed cells were then embedded in Spurr's low viscosity resin. Thin sections were cut with a diamond knife using a DuPont/Sorvall MT2-B ultramicrotome and examined with a JEOL 1200EX scanning/transmission electron microscope operating at 80 kV accelerating voltage.

3. Results

For June 17-18, composition of 200 cell sub-samples based on the four categories of vacuoles was plotted against time (Fig. 4). During this period, cell density ranged from 110-2738 cells/ml. Low tides occurred at 7:09 am and 7:27 pm on the 17th and at 8:13 am on the 18th. The sun rose at 5:12 am and set at 8:22 pm on the 17th. Average water column temperature ranged from 17.1°C to 19.7°C (Fig. 5), while salinity varied from 24.5 PSU to 25.9 PSU. Although profile data were collected for both temperature and salinity parameters, the values for each sampling time were averaged because the samples were depth integrated.

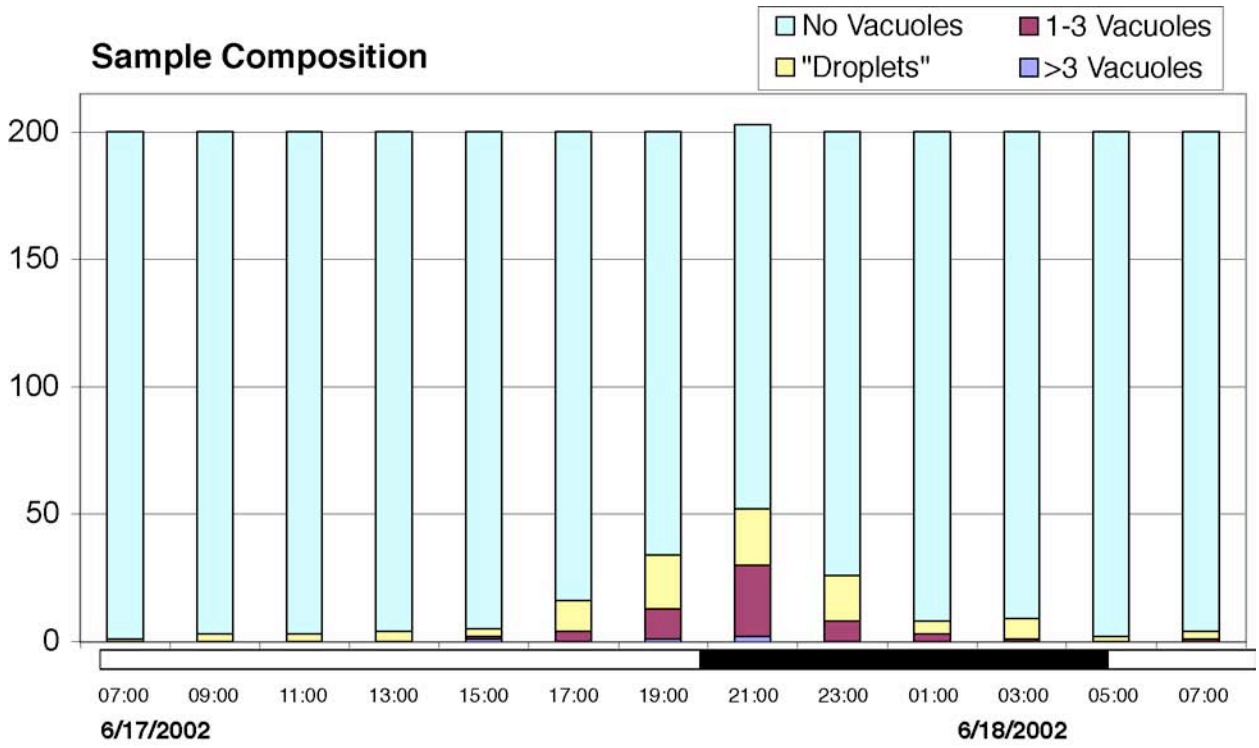

Figure 4. Composition of a 200 cell sub sample by category for June 17-18, 2002. The 2100h sample consisted of 203 cells. Black and white bar on X-axis represents photoperiod.

The sample taken at 2100h contained the highest number of cells with vacuoles and all categories related to vacuoles peaked in this sample. Cells containing droplets comprised 11% of the sample, while cells with 1-3 vacuoles accounted for 14% of the sample, and 1% of the cells contained greater than 3 vacuoles. Moreover, on either side of the 2100h sample, numbers of vacuolated cells dropped off evenly generating a singular curve with a maximum at 2100h (Fig. 6).

The July 22-23 sampling period was characterized by cell densities nearly two orders of magnitude lower than June 17-18, with concentrations ranging from 1-20 cells/ml. Of the 0900 sample, 2% of cells included 1-3 vacuoles while no others contained vacuoles. The 2100h sample consisted of 2% cells with greater than 3 vacuoles and 4% cells with droplets. However, due to the low number of cells analyzed, the results are decidedly less accurate and cannot be directly related to the June 17-18 study.

Epifluorescence was also used to help determine presence of food vacuoles. Because the finger-like projections of the chloroplasts extend over the cell, they can be mistaken for vacuoles. The primary pigment, phycoerythrin, fluoresces orange under blue light excitation, whereas vacuoles typically did not fluoresce. Vacuoles, then, could be identified by the dark gap they left between chloroplast projections. However, 4-5 cells examined were exceptional in that structures that were clearly vacuoles fluoresced a whitish-green. The vacuoles in these instances were always numerous and dispersed throughout the cell.

The limited number of thin sections analyzed via TEM failed to yield cells with vacuoles, and further analysis could not be performed. We have included a plate which shows typical dinoflagellate morphology (Fig.7).

4. Discussion

Results from the June 17-18 study of the Greenwich Cove population of *D. acuminata* show a strong association of feeding with time of day, 2100h, for this population. This conclusion of a nighttime feeding peak is supported by Gréneli et al. (1997) who determined that positive carbon uptake for this species occurs even in the dark. If *D. acuminata* feeds exclusively at night, feeding behavior may be induced by darkness, explaining the inability to observe a feeding event. Moreover, physical disturbance incurred during movement of samples may also interrupt feeding events. Therefore, a to date failure to view feeding should not be allowed to directly preclude mixotrophy.

Other factors that relate to photosynthesis should also be tested for correlation with feeding in future studies. Mixotrophy, as a nutritional strategy, is used as a

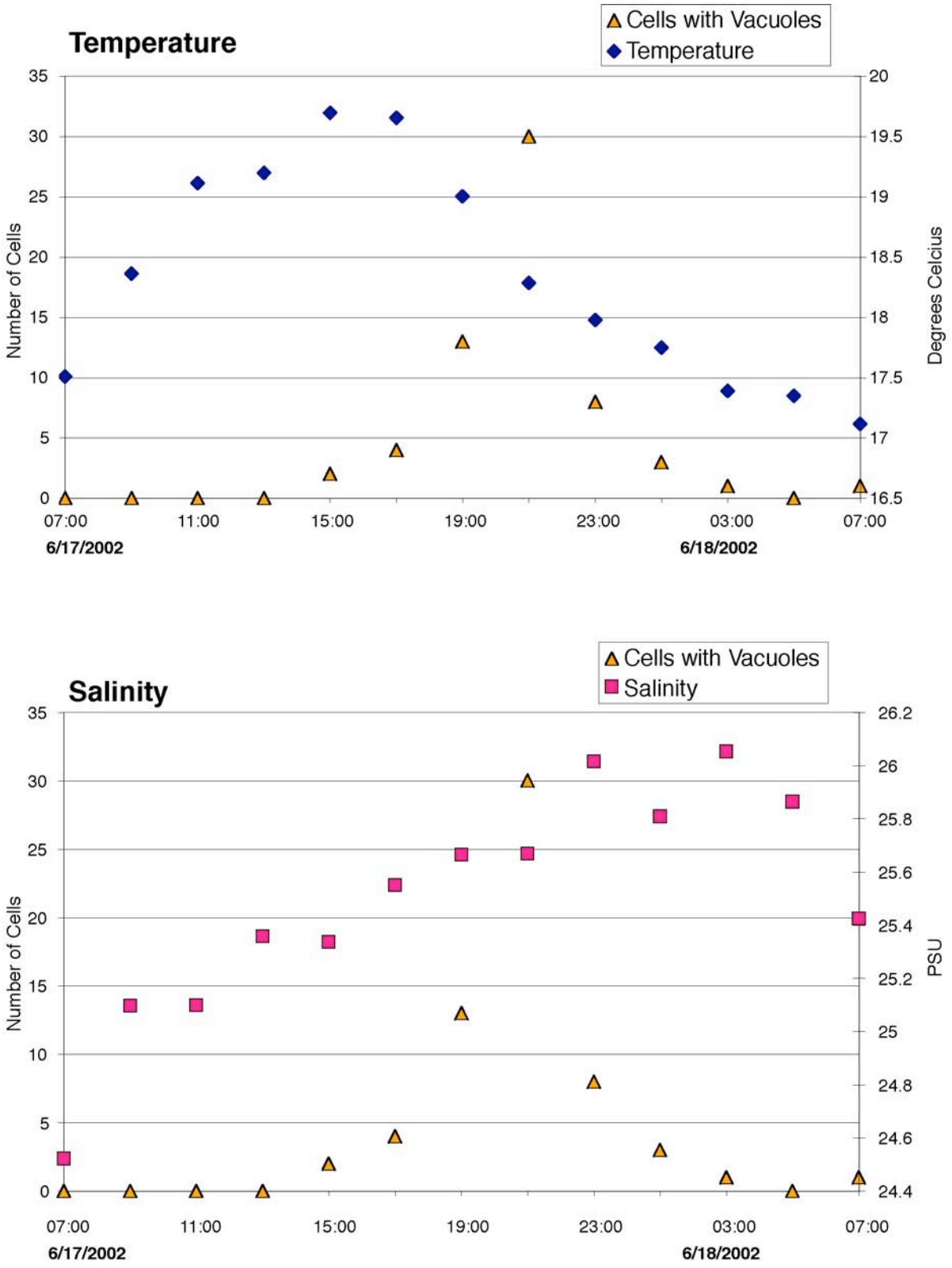

Figure 5. (top) Average water column temperature in degrees Celsius and number of cells with vacuoles (1-3 and >3) on June 17-18, 2002. (bottom) Average water column salinity in PSU and number of cells with vacuoles (1-3 and >3) on June 17-18, 2002.

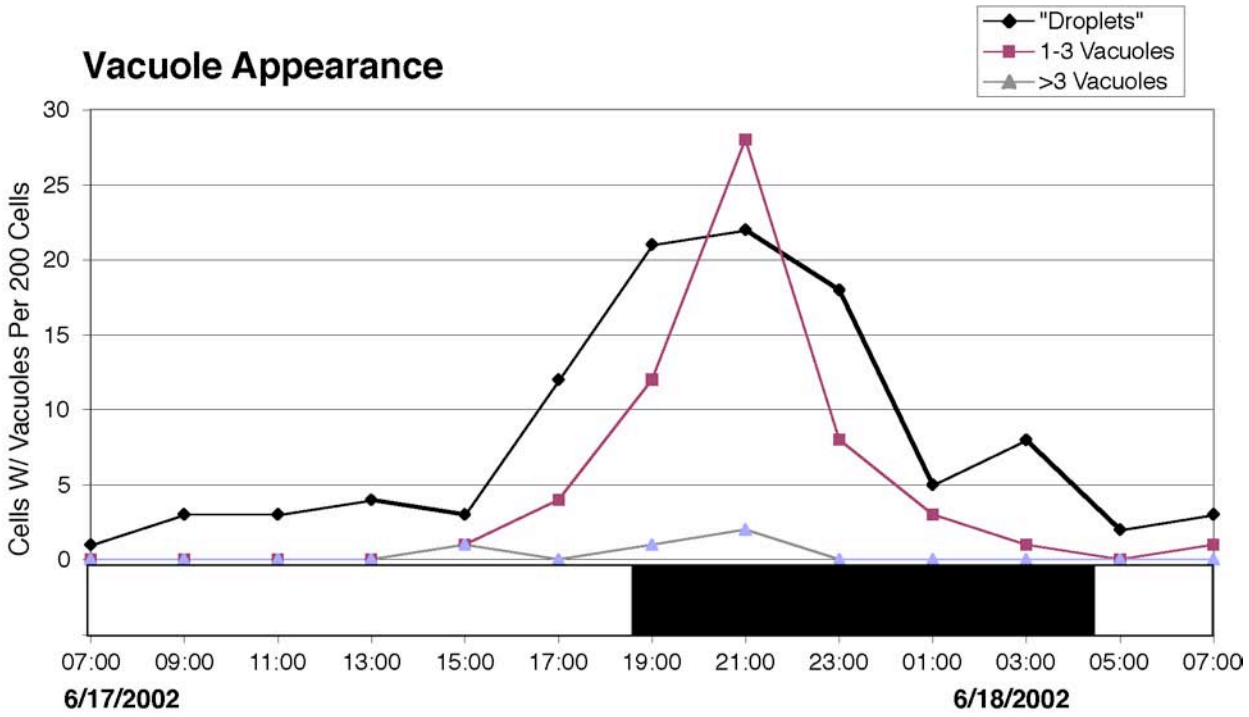

Figure 6. Number of cells with categorized vacuoles per 200 cells by sample for June 17-18, 2002. Black and white bar on X-axis indicates photoperiod.

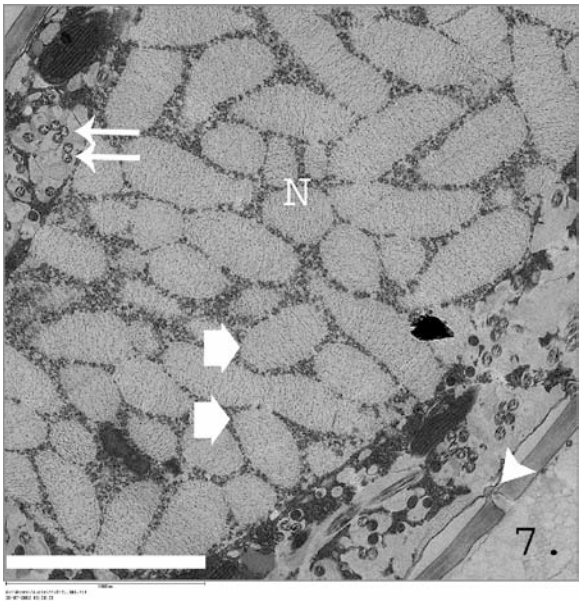

Figure 7. Thin section transmission electron micrograph of cross section of *D. acuminata* cell. White scale bar equals 5 µm. Note rhabdosomes (long white arrows) and condensed chromosomes (wide white arrows) typical of *Dinophysis* cells. White arrowhead points to a thecal pore where the membrane joins the theca. Magnification-4000x.

supplement to photosynthetic production, and thus timing of feeding is likely to be dependant on conditions for photosynthesis. A timing pattern related to physical conditions of the environment, such as light intensity and vertical water column mixing, is likely to influence the amount of feeding occurring in the *D. acuminata* community. Therefore, we should expect feeding to vary temporally.

Method of feeding is often a further stumbling block in understanding mixotrophy for this species. In their initial study Jacobson and Andersen (1994) offered a simplified peduncle as the most likely candidate. However, previous examination of this structure concluded that the "reduced" peduncle indicated a lost ability to feed via myzocytosis (Lucas and Vesk 1990). Lucas and Vesk further speculate that the flagellar pore, through which the peduncle would have to extend, is much too narrow to permit passage of this structure. A later evaluation of the peduncle found it similar to that of two actively phagotrophic species of dinoflagellates, *Dinophysis rotundata* and *Oxyphysis oxytoxioides* (Jacobson and Anderson 1992). The peduncle of all three species contains only a single microtubular ribbon, which, in the case of *D. rotundata* and *O. oxytoxioides* at least, is sufficient for myzocytosis. Moreover, Jacobson and Anderson (1992) also hypothesize that the unique myonemal structure surrounding the flagellar pore in these two species, may allow for deformations in the size and shape of the pore, as would be necessary for ingestion of the large food vacuoles found inside the

cells. *D. acuminata* exhibits a similar structural setup (Jacobson and Andersen 1994).

Admittedly a certain amount of subjectivity exists in evaluation of food vacuoles. The droplets we examined occurred in a size spectrum that occasionally made categorization difficult. However, due to the preliminary nature of this study, we decided to err always on the conservative side of the question. Therefore, vacuoles were only counted when definitive identity was established. We expect that as a result our vacuole counts are lower than what was actually there.

Unfortunately, due to the brevity of the project period, we were unable to successfully replicate our findings. However, the clarity and strength of the feeding peak in the initial study offer impetus for further study of the pattern. Attempts should be made to replicate the association with the various physical factors (salinity, temperature, tide, photoperiod).

The inclusion of mixotrophy in the characterization of *D. acuminata* has had important ramifications not only for trophic web dynamics, but also for the ability to maintain the species in culture. The feeding behavior of this photosynthetic *Dinophysis* species has been hitherto poorly studied, despite being established by Jacobson and Andersen in 1994, but it may be the key to successful culture maintenance.

Acknowledgements. Lucie Maranda, Jan Rines, Paul Johnson, Malcolm McFarland, Paul Hargraves, Percy Donaghay, Jim Sullivan, the National Science Foundation, and the East Greenwich Police Department.

References

Berland BR, SY Maestrini, D Grzebyk, and P Thomas 1995 "Recent aspects of nutrition in the dinflagellate *Dinophysis* cf. *acuminata*" *Aquatic Microbial Ecology*. Vol 9(2): 191-198.

Granéli E, DM Anderson, P Carlsson, and SY Maestrini 1997 "Light and dark carbon uptake by Dinophysis species in comparison to other photosynthetic and heterotrophic dinoflagellates" *Aquatic Microbial Ecology*. Vol. 13(2): 177-186.

Jacobson D, and R Andersen 1994 "The discovery of mixotrophy in photosynthetic species of *Dinophysis* (Dinophyceae): light and electron microscopal observations of food vacuoles in *Dinophysis acuminata*, *D. norvegica* and two heterotrophic dinophysoid dinoflagellates" *Phycologia*. Vol 33 (2): 97-110.

Jacobson D, and DM Anderson 1992 "Ultrastructure of the feeding apparatus and myonemal system of the heterotrophic dinoflagellate *Protoperidinium spinulosum*" *Journal of Phycology*. Vol 28(1): 69-82.

Jacobson D, and DM Anderson 1996 "Widespread phagocytosis of ciliates and other protests by marine mixotrophic and heterotrophic thecate dinoflagellates" *Journal of Phycology*. Vol 32(2): 279-285.

Lucas IAN, and M Vesk 1990 "The fine structure of two photosynthetic species of *Dinophysis*" *Journal of Phycology*. Vol 26(2): 345-357.

Maestrini SY, BR Berland, D Grzebyk, AM Spano 1995 "*Dinophysis* spp. cells concentrated from nature for experimental purposes, using size fractioning and reverse migration" *Aquatic Microbial Ecology* Vol. 9 (2): 177-182.

Magnetic analysis of a Lake Tanganyika sediment core

Joseph D. Malkovich[1] and John W. King

Graduate School of Oceanography, University of Rhode Island, Narragansett, Rhode Island

Abstract. A long-range paleomagnetic data set from sediment core T97-52V from Lake Tanganyika, East Africa is used in this study to construct paleosecular variation age models. Inclination records closely correlate to two other regional paleomagnetic records, and show nearly linear age-depth relationships on ~25 ka and ~80 ka time frames. Paleosecular variation age models confirm the accuracy of an established robust radiocarbon age model for the core. Environmental magnetic data obtained from the core prove unsuitable for high-resolution paleolimnological and paleoclimatological analyses of Lake Tanganyika and equatorial Africa due to the effects of reduction diagenesis throughout much of the core. Coarse evidence for stadial-interstadial climatic transitions appears in the environmental magnetic proxies and implies high-latitude forcing of equatorial interior African climates since early marine oxygen isotope stage four. The signature of stadial-interstadial climatic transitions further validate radiocarbon and paleosecular variation T97-52V age models.

1. Introduction

1.1. Background

Research focused on environmental change has become increasingly important as investigators examine human impacts on natural systems. Possible consequences of anthropogenic-induced climate change have sparked climate research on time scales varying from several decades to hundreds of millions of years (Ruddiman, 2001). An understanding of past natural climatic variation is vital in order to qualify recent and present human disturbances of climate systems and to assess possible future environmental consequences of human actions (Bradley, 1999).

This paper uses paleomagnetic and environmental magnetic measurements to analyze a Lake Tanganyika sediment core. Magnetic methods are useful tools for dating and environmental analysis, since they are fast, non-destructive, easy to carry out, and relatively inexpensive compared to other sediment dating and climate proxy analyses like micropaleontological studies, palynology, geochemistry and isotope analyses, and electron microscopy (Verosub and Roberts, 1995).

This study contributes to reconstructing the climatic history of continental equatorial Africa in two important ways. Directional changes in Earth's magnetic field over time are compared to two other regional records to construct paleosecular variation (PSV) age models. A scarcity exists of studies detailing PSV records for Africa (Williamson et al, 1991). This paper adds an important data set to the sparse regional record on a time frame greater than 80 ka, much longer than other regional PSV studies (e.g. Thouveny and Williamson, 1988; Williamson et al, 1991; Walker, 2001). Establishing an accurate age model is a crucial first step in paleoclimatic reconstruction, since knowledge of the timing of locally observed past climatic events is necessary to attempt correlation with other climate studies, or to propose causal mechanisms for observed events. The present study also attempts to examine Lake Tanganyika limnology and regional climate using mineral magnetic properties of the sediment. This approach assumes variations of measurable magnetic materials in lacustrine sediments preserve records of environmental change (Dearing, 1999).

Investigators have been keenly interested in the climatic significance of past water level variations in Lake Tanganyika. But studies of sediment cores (e.g. Vincens et al, 1993; Williamson et al, 1991; Gasse et al 1989) or paleontological evidence such as stromatolites (Cohen et al 1997a) have focused on time frames shorter than the past 30 ka. Seismic investigations have tended to focus on changes over long time scales (several Ma) with lower resolution (e.g. Cohen et al, 1997b; Lezzar et al, 1996). Scholz et al (2002, in press) have completed an initial study on a Lake Tanganyika core with an uncharacteristically long time scale, using non-magnetic proxies such as biogenic silica, organic carbon, lithostratigraphy, and seismic stratigraphy to examine lake levels over the past ~100 ka. The present paper closely follows the Scholz et al (2002, in press) analysis of Lake Tanganyika core T97-52V, and uses PSV correlation to constrain the core's robust ^{14}C age model. This study comprises part of an ongoing project examining east African rift lakes.

1.2. Climate forcing mechanisms in tropical Africa

Climate studies of equatorial Africa have presented conflicting evidence regarding possible forcing mechanisms of natural climatic oscillations. Investigators generally agree that astronomic orbital (Milankovitch) cycles have influenced Quaternary tropical African climates. But whether precession-controlled (~ 20 ka) direct insolation variations or longer scale eccentricity-modulated (~100 ka) cycles and consequent ice volume oscillations of the past 800 ka have effected these climate changes remains in contention (Scholz et al, 1998).

[1]Now at Gustavus Adolphus College, St. Peter, Minnesota

Ample evidence supports the presence of dominant 100
ka glacial-interglacial cycles in high-latitude records of the past 900 ka. Shorter precession and obliquity (~41 ka) orbital cycles, however, have played a mitigating role (Ruddiman, 2001). deMenocal (1995) reports that over the past 2.8 Ma cold North Atlantic sea surface temperatures have caused climatic cooling and increased aridity in tropical Africa. Northern Hemisphere incipient glacial cycles have been implicated in creating the initial cold sea surface temperatures and causing cessation of direct precessional climatic control (deMenocal, 1995). Spectral analysis of marine oxygen isotope data has shown that obliquity and precession cycles superimposed on the dominant eccentricity cycle have been responsible for high-latitude ice volume and climate fluctuations over the past 450 ka (Imbrie and Imbrie, 1979).

Researchers have also observed connections between shorter orbital scale changes in high-latitude processes and subtropical African climate. For example, deMenocal (1995) relates that ~41 ka periodic eolian dust fluxes into the Atlantic from equatorial west Africa have occurred contemporaneously with high-latitude climatic cooling, yet never explicitly argues for high-latitude causation for this phenomenon as he does with his observed eccentricity dominated glacial-interglacial remote forcing trend. Sub-orbital scale North Atlantic Heinrich events that correlate with changes in organic carbon data from the Arabian Sea reinforce the possibility of a teleconnection between polar and subtropical marine climates (Schulz et al, 1998). A similar correlation between Heinrich events and peaks in organic carbon data observed in Lake Tanganyika supports such a teleconnection extending to continental equatorial Africa (Scholz et al, 2002, in press). Neither of these studies, however, argues for high-latitude causation of low-latitude climate behavior.

Studies inferring late Pleistocene-Holocene Lake Tanganyika water levels and regional climate from sediment proxies (e.g. Gasse et al, 1989; Vincens et al, 1993) and hydrologic budget models (Bergonzini et al, 1997) report evidence for lake levels varying contemporaneously with Milankovitch cyclicity-driven global ice volume. These researchers argue that lake level fell during the last cool and dry tropical stadial (the Last Glacial Maximum) and rose during the present warmer and wetter tropical interstadial. Alternatively Pokras and Mix (1987) argue that late Pleistocene and Holocene climate changes in equatorial Africa have been directly forced by precession-driven insolation changes. Others extend the argument further and contend that both equatorial and sub-polar climates respond directly to primary and harmonic precessional cycles (McIntyre and Molfino, 1996). Recent paleoenvironmental reconstructions in tropical Africa based on lacustrine mineral magnetic data have been completed by Williamson et al, (1993), Williamson et al (1998), and Walker (2001), although these papers do not focus on the low-latitude climate forcing controversy discussed above. The present study attempts to add clarity to this complex issue using paleomagnetic and mineral magnetic analyses.

1.3. Cause of magnetism in lacustrine sediments

Earth's magnetic field has been linked to convection currents in the molten iron-nickel outer core that produce the self exciting geodynamo, although the field-generating process is still a matter of some debate (McElhinny, 1973). A possible causal mechanism for convection involves inner core growth through gradual cooling and the preferential fractional addition of iron from the outer core (Merrill and McFadden, 1990). The hypothetical consequent enrichment of lower-density, buoyant minerals at the inner core-outer core boundary creates convection cells that supply mechanical energy to drive the geodynamo.

The sum of three vectors completely define the geomagnetic field at any location: declination (D), inclination (I), and intensity (F) (Figure 1) (Thompson and Oldfield, 1986). Inclination, the dip angle of a field line above or below the horizontal plane tangential to Earth's surface, depends on latitude (□), and is currently defined as positive in the northern hemisphere where a compass needle's north-seeking end plunges downwards (McElhinny, 1973). Declination, the field's horizontal component, is the angle between geographical north and the local magnetic meridian. Magnetic intensity is the

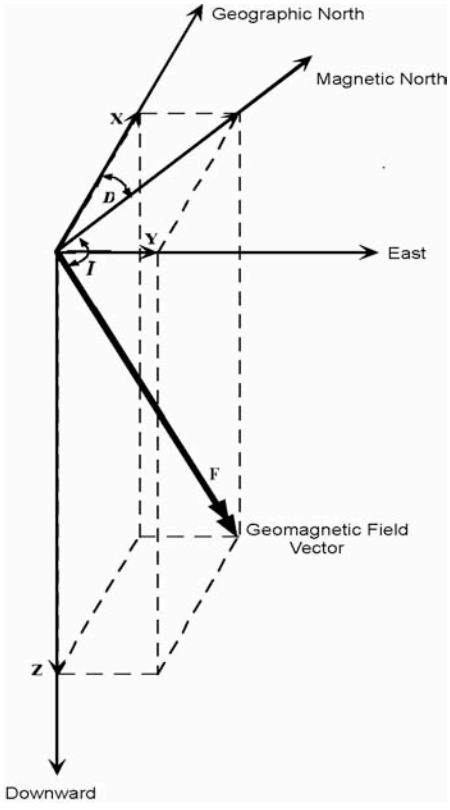

Figure 1. Diagram of the three vector components comprising Earth's magnetic field at any location: Declination (D), Inclination (I), and Intensity (F). Drawn after McElhinny, 1973.

average dipole moment along the directional sum of declination and inclination (Butler, 1992).

Earth's magnetic field varies in direction and intensity on several time scales. Secular variation is the phenomenon of annual to millennial scale changes in declination and inclination (Thompson, 1984). When a best-fit dipole field (Figure 2) is subtracted from the actual field observed at Earth's surface a significant non-dipole field component becomes apparent (Figure 3) (McElhinny, 1973). The non-dipole field tends to move westward between 0.2 and 0.6 degrees per year (Thompson and Oldfield, 1986). Geophysicists have demonstrated that outer core fluid motions orders of magnitude smaller than the convection implicated in generating the main dipole field produce the non-dipole field drift, revealing the cause of secular variation (Jacobs, 1994). The geomagnetic axial dipole (GAD) model states that to a first approximation the geomagnetic axis equals Earth's rotational axis when averaged over time scales greater than 10^4 years (Figure 4). According to the GAD model the directional components of secular variation fluctuate around a long term mean such that D = 0° and tan I = 2 tan □ (Butler, 1992).

Minerals containing iron are of primary importance for magnetic analyses, and these may be categorized based on their reactions to magnetic fields. A paramagnetic mineral exhibits magnetic behavior only in the presence of an applied field, and its magnetization is lost when the field is removed regardless of field intensity (Butler, 1992). Spontaneous magnetization--the parallel orientation of adjacent electrons' spin magnetic moments--gives rise to remanent magnetization, or magnetic behavior in the absence of an applied field (Thompson and Oldfield, 1986). Two varieties of magnetic minerals receive dominant attention in paleomagnetic and environmental magnetic studies: ferrimagnets, such as magnetite (Fe_3O_4) and maghemite (Fe_2O_3), and canted antiferromagnets, such as hematite (□Fe_2O_3) and goethite (□FeOOH) (Thompson and Oldfield, 1986). The importance of ferrimagnetic iron monosulfides such as greigite and mackinawite and the paramagnetic disulfide pyrite (FeS_2) may also play a role in magnetic studies where reduction diagenesis has altered the originally deposited sediments (Karlin and Levi, 1983; King and Channel, 1991). Since iron is ubiquitous in the crust, iron-bearing magnetic minerals constitute a significant sedimentary fraction in many depositional environments, allowing analysis of paleomagnetic natural remanence and

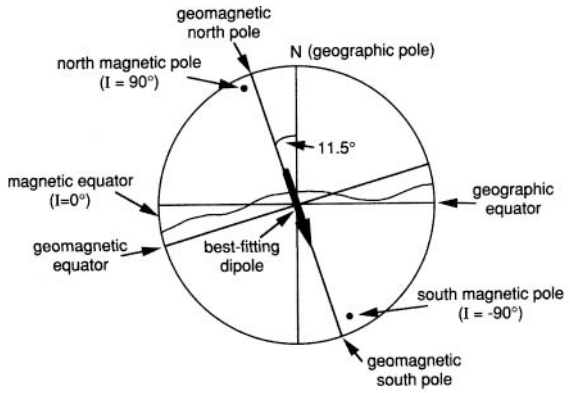

Figure 2. Diagram showing the best fitting dipole approximation of Earth's magnetic field, denoted in this figure by the geomagnetic equator, geomagnetic poles, and solid geocentric arrow. The main dipole accounts for only 80-90% of observed directional magnetic field behavior at Earth's surface. From Butler, 1992.

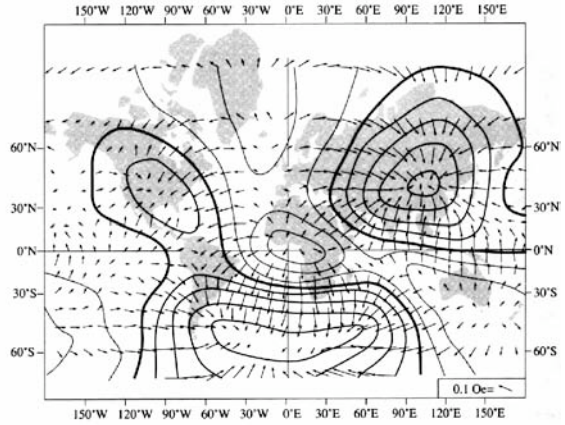

Figure 3. Map showing the non-dipole magnetic field, the result of subtracting the main dipole field from the actual magnetic field. Arrows indicate the direction and intensity of the horizontal component of the field. The scale in Oe is at bottom right (1 Oe = 0.1 mT). Contours show lines of equal vertical intensity of the non-dipole field. Thick black lines indicate a zero vertical non-dipole component. Thin black lines denote downward (positive) intensity and thin gray lines denote upward (negative) intensity. Contour interval is 0.02 Oe. From Butler, 1992.

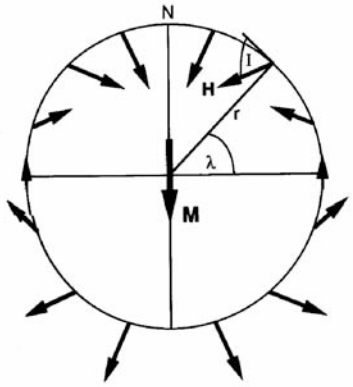

Figure 4. Diagram depicting the Geocentric Axial Dipole (GAD) model of Earth's magnetic field. Inclination and declination tend to fluctuate around mean values predicted by the model. These average values are calculated on time scales greater than 10^4 years.

responses to laboratory imparted magnetic procedures.

Paleosecular variation is the signature of non-dipole field movement preserved in the geologic (predominantly sedimentary) record (Thompson and Oldfield, 1986). Obtaining PSV data from sediments requires the measurement of natural remanent magnetization (NRM). NRM is a vector sum of magnetic declination, inclination, and intensity, and is an intrinsic property of a magnetic mineral grain dependant on grain morphology and magnetic field behavior when the grain cooled below its blocking temperature (thermoremanent magnetization, or TRM) or grew larger than its blocking volume (chemical remanent magnetization, or CRM) (Thompson and Oldfield, 1986). Lacustrine sediments preserve an expression of NRM through detrital remanent magnetic processes. Depositional remanent magnetization (DRM) occurs when previously magnetized mineral grains align with the ambient field while settling through the water column (Verosub, 1977). Post-depositional remanent magnetization (PDRM) occurs below the water-sediment interface and involves field-induced particle rotations in fluid-filled interstices above NRM lock-in depth (King and Channel, 1991). PDRM lock-in requires sufficient sediment dewatering to mechanically inhibit grain rotation (Butler, 1992), and typically occurs between 5 cm and 40 cm for fine grained sediments depending on sedimentation rate (Williamson et al, 1991). Since non-dipole field foci fluctuate non-periodically on time scales typically shorter than several thousand years (Thompson and Oldfield. 1986) continental-size non-dipole anomalies permit stratigraphic correlation with a resolution on the order of 10^2 to 10^4 years between lakes within several thousand km (Figure 3) (King and Peck, 2001).

1.4. Physical setting and study site

Lake Tanganyika (~3.5°-9° S, ~29°-31.5° E), one of the world's largest and deepest lakes, occupies a basin that began to form over 10 Ma with incipient east African rifting (Figure 5) (Lezzar et al, 1996). The lake is currently situated at a surface elevation of 773 m, has a maximum

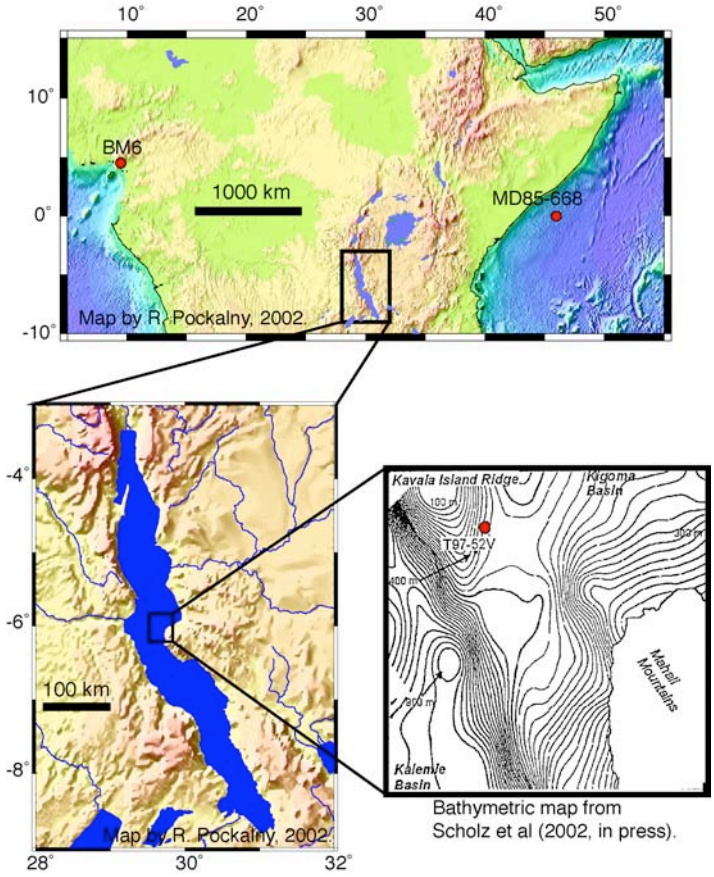

Figure 5. Location maps of Lake Tanganyika and the study area. The top map shows Lake Tanganyika in relation to core site BM6 in Lake Barombi Mbo, Cameroon and core site MD85-668 in the Indian Ocean's Somali Basin. Note these proximity of these cores to Lake Tanganyika within the 3000-4000 km radius of effective PSV correlation. The map at bottom left shows the general situation of the Kavala Island Ridge accommodation zone in central Lake Tanganyika. The bathymetric map of the study area at bottom right shows southeastern ridge morphology and the location of core T97-52V at 393 m water depth. Contour interval is 50 m. Notice the core site on the topographic "saddle" between the Mahali Peninsula to the southeast and the ridge axis to the northwest. Maps by R. Pockalny (2002) and from Scholz et al (2002, in press) as indicated.

depth of 1470 m, a volume of 18,000 km^3, and a surface area of 32,600 km^2 (Bergonzini et al, 1997). A series of linked half-graben depocenters, in which over 6 km of sediment have accumulated since rifting began, structurally control lake morphology, and the consequent high-relief basin provides a good location for paleolimnological studies since the majority of water loss is from evaporation (Scholz and Rosendahl 1988). As much as 94% of water loss comes from evaporation (Gasse et al, 1989), and the remaining percentage exits the lake through the Lukuga River, which controls maximum lake level during the modern high stand (Lezzar et al, 1996). Lake Tanganyika water level low stands are caused by low regional precipitation:evaporation ratios due to the high regional evaporation rate and because the high-relief basin receives most of its runoff from short streams originating on rift scarps close to the lake margin, with the exception of the Malagarasi River (Figure 6) (Cohen et al, 1997a). Climatically driven changes in Lake Tanganyika's hydrologic budget have resulted in mainly vertical movements of water levels because the basin is so steep sided, evidenced in the relatively small lateral facies migrations visible in the sedimentary record (Cohen et al, 1997b).

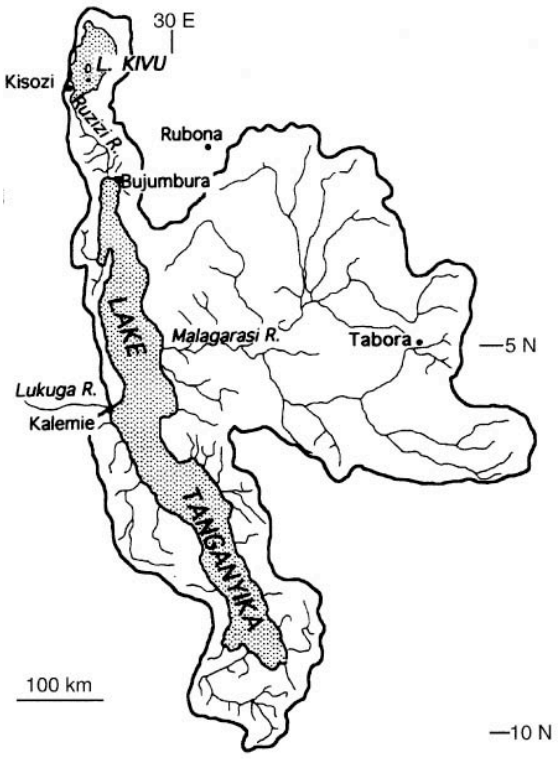

Figure 6. Map showing Lake Tanganyika's catchment area. The catchment area is large in absolute terms, but notice that except for the Malagarasi River watershed all streams draining into the lake originate ~100 km or less from the shoreline due to basin structural morphology. From Bergonzini et al, 1997.

Lake Tanganyika therefore serves as a valuable archive of equatorial African climate change since its hydrology and structural morphology have permitted rapid and large-magnitude water levels fluctuations (Scholz and Rosendahl, 1988). But the lake has preserved long-range, nearly continuous sedimentary records since its enormous volume has usually prevented the complete desiccation that has befallen other regional lakes during extended and severe dry climatic intervals (Scholz et al, 1998). Various studies cite sediment discontinuities as evidence that lake levels have fallen over 400 m below present lake level several times in the last several 100 ka (e.g. Scholz and Rosendahl, 1988; Lezzar et al, 1996; Cohen et al, 1997b; Scholz et al, 2002, in press). Establishing the timing of Lake Tanganyika water level variations is vital to climatologic reconstruction and also bears important implications for scientists' understanding of rapidly divergent fish evolution by paleogeographic isolation when lake levels have fallen low enough to create several distinct paleo-lakes between exposed topographic highs (Cohen et al, 1997b). The Kavala Island Ridge (KIR) is a submerged topographic high, or accommodation zone, in central Lake Tanganyika (Figure 5) (Scholz et al, 1998). Approximate KIR latitude of ~6°S results in a GAD model (Figure 4) predicted inclination of -11.8°. The KIR comprises part of the southeast-northwest trending Kalemie-Mahali bathymetric shoal that divides the lake into a northern basin and a southern basin (Lezzar, et al, 1996). Core T97-52V was collected in 1997 during an extensive coring and seismic profiling cruise on Lake Tanganyika (Scholz et al, 2002, in press). The site is located on a "saddle" between the 40 m deep ridge crest to the northwest and the Mahali Peninsula to the southeast. The core site depth of 393 m minimized the chances of physical sediment disturbance from bioturbation (Scholz et al, 2002, in press), since Lake Tanganyika is a meromictic lake with permanently anoxic conditions extant below 150 m (Scholz et al, 1998).

The core location was selected based on seismic profiles depicting almost 10 m of undisturbed strata overlying two pronounced seismic discontinuities characterized by high seismic amplitudes (Scholz et al, 2002, in press). The upper seismic discontinuity was a successful target of core T97-52V and appears as a lithologic unconformity 940 cm down core. Truncated seismic unconformities reveal former subaerially exposed and eroded sediments (Scholz and Rosendahl, 1988). Scholz et al (2002, in press) follow this interpretation and its lake level implications for the 940 cm discontinuity. Seismic profiling was also used to constrain the coring location by assuring investigators that subaqueous mass wasting processes such as those reported in other Lake Tanganyika study areas by Vincens et al (1993) and Cohen et al (1997b) were absent and had caused no physical disturbance of the targeted sediment.

A previously collected core revealed predominant hemipelagic sediment ideal for magnetic analysis at core

site T97-52V, a logical result of the site's location far from fluvial sediment input into the lake (Hecky and Degens, 1973, cited in Scholz et al, 1998). This early core suggested a sedimentation rate on the order of 10 cm per ka, which was corroborated by the proposed radiocarbon age model of Scholz et al (2002, in press). A sedimentation rate an order of magnitude less than that recorded for other Lake Tanganyika cores (e.g. Gasse et al, 1989; Williamson et al, 1991; Vincens et al, 1993) allows examination of ~80 ka of nearly continuous data down to the 940 cm unconformity in a conventional ~10 m core (Scholz et al, 2002, in press).

2. Methods and Data

2.1. Core sampling and lithology

A suite of six deep-water electric vibracores was collected from the KIR of central Lake Tanganyika in 1997. Data from T97-52V (~10.4 m long) is presented in this paper. Following field collection the core was sectioned on ship, and afterwards split and stored at the University of Rhode Island's sediment core repository at the Narragansett Bay Campus. The upper 40 cm of the core were missing when the core was removed from the repository.

Seven U-channel sub-samples ~150 cm long and 3.6 cm^2 in cross sectional area were extracted from the center of the split core during 6/2002, and magnetic properties were measured during 6-7/2002. U-channel sub-sampling allows measurement on a limited-access pass-through cryogenic magnetometer, yielding data at much smaller sample intervals than possible with discreet cubic sub-samples (Walker, 2001). Sampling from the center of the core also reduces the possibility that physical disturbances caused during the coring process, a likelihood due to the nature of electric vibracores, could have marred the magnetic data (Scholz et al, 1998).

Alternately laminated and homogenous brown to gray-green muds dominate the lithology of T97-52V (Figure 7). Green muds typically indicate the presence of reduced iron (J. Maxson, pers. comm., 2002), and have been observed in other Lake Tanganyika cores recovered from similar depths (e.g. core MPU12 in Vincens et al, 1993). Apart from mm-scale laminations, obvious sedimentary structures are absent in the core. However, the nearly uniformly fine-grained sediment column is interrupted by a 5-cm thickness of dark fibrous organic material at 665 cm. A distinct transition occurs in sediment color around 940 cm down-core, where brown to gray-green laminated mud abruptly switches to homogenous gray mud. Discreet sub-samples showed that below 940 cm water content was 45%, considerably less than the 75% determination for the core above this level (Scholz et al, 2002, in press). During U-channeling of the bottom ~150 cm greater stiffness, cohesiveness, and resistance to U-channel insertion were observed compared to the core sections above 940 cm. Non-magnetic sediment physical properties therefore correspond to the visually apparent lithologic shift at 940 cm.

2.2. Magnetic measurements

This study uses two general types of data: paleomagnetic measurements and environmental magnetic measurements of laboratory imparted magnetizations and remanences (Thompson and Oldfield, 1986). Automated pass-through cryogenic magnetometers permit rapid, non-destructive, and inexpensive collection of this wide variety of magnetic

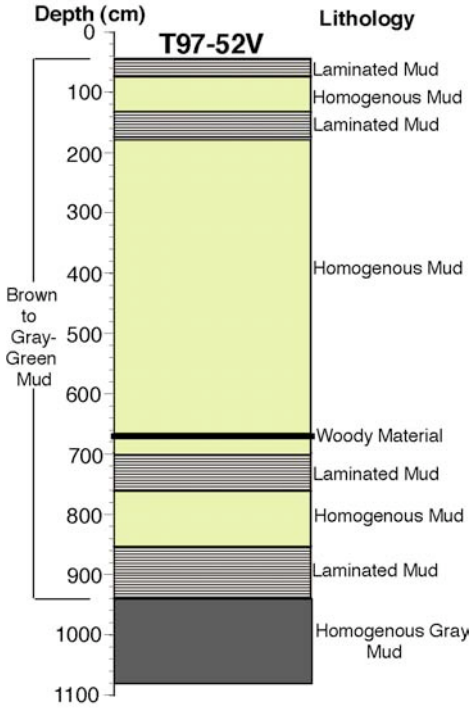

Figure 7. Diagram showing lithology of core T97-52V. The upper 40 cm of core are missing. From 40-940 cm brown to gray-green laminated and homogenous muds dominate. Homogenous gray mud containing much less pore water extends from 940-1085 cm (bottom of core).

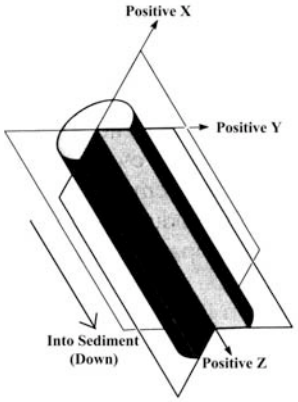

Figure 8. Diagram showing X, Y, and Z directions of a sediment core acquired perpendicular to the sediment-water interface. U-channels are pressed into the split core face along the long (Z) axis, so X, Y, and Z directions are the same in the cores and U-channels.

data (King and Channel, 1991). Room temperature U-channels pass through a chamber housing Superconducting Quantum Interference Device (SQUID) sensors, cooled by liquid helium to 4° K. Magnetic minerals in the sediment cause a flow of electrons in the SQUIDs, which translate current strengths into the average magnetic moments of U-channel intervals (Butler, 1992). Three SQUIDs measure magnetic moments in three orthogonal directions: X, Y, and Z (Figure 8). A computer generates composite intensity and sediment magnetization directions from these orthogonal measurements. All magnetic data reported in this paper except low-frequency susceptibility were measured at 1 cm sampling intervals on a 2-G Enterprises cryogenic magnetometer.

During coring, storage, and sample handling procedures sediment cores acquire weak and unstable magnetizations called overprints that obscure NRM signals. Overprints were removed by alternating frequency (AF) demagnetizing coils in this study. An AF field with linearly decreasing intensity removes magnetizations with coercivities less than the peak field intensity by aligning magnetic moments antiparallely through rapid 180° changes in field direction. These antiparallel magnetizations effectively average out to zero net
magnetization (Butler, 1992). Magnetic cleaning allows measurement of true NRM because viscous and isothermal remanent magnetizations (VRM and IRM) show much less resistance to AF demagnetization than CRM or TRM, the remanences giving rise to sedimentary DRM (McElhinny, 1973). Therefore AF demagnetization has been used both to remove both low-intensity magnetizations acquired over time (VRM) (Thouveny and Williamson, 1988) and due to physical core disturbance (Scholz et al, 1998).

2.3. Paleomagnetic data

Paleomagnetic data (declination, inclination, and NRM intensity) were measured first to record the sediments' preservation of the Earth's magnetic field behavior through time (Figure 9). Inclination data were subsequently used to signal changes too greatly

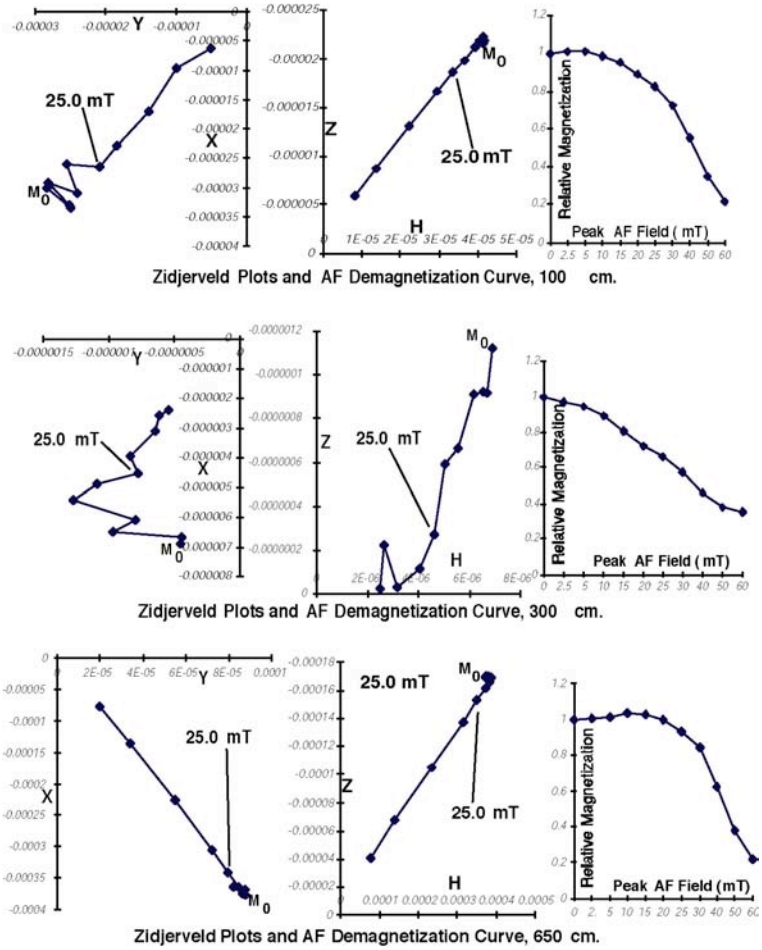

Figure 9. T97-52V declination, inclination, and NRM intensity. Note that NRM intensity does not indicate the strength of the geomagnetic field, but rather the intensity of sediment magnetization, which can be influenced by ulterior factors including sedimentation rate, diagenetic activity, magnetic concentration, magnetic grain size, and magnetic mineralogy.

construct paleosecular variation age models for the core (King et al, 1983; Thouveny and Williamson, 1988; Williamson et al, 1991; King and Peck, 2001; Walker, 2001). The vertical line in the plot of T97-52V inclination is the predicted GAD inclination of -11.8° for the study site. Actual observed average inclination was -12.5°, indicating inclination data is fit for paleosecular variation correlation. The NRM intensity and too rapidly to indicate changes in Earth's magnetic field strength over time, and therefore must be controlled lithologically by sediment properties (J. King pers. comm., 2002).

During measurement of paleomagnetic data AF demagnetization was imparted stepwise from 2.5 mT to 60.0 mT, and the removal of overprints and decreasing remanence intensity were observed with Zidjerveld plots and AF demagnetization curves (Figure 10). A trend from M_0 (initial magnetization) toward the origin in Zidjerveld plots indicates demagnetization of true remanence and therefore the removal of overprints. Demagnetization curves show sediment remanent magnetization following each AF step. Notice that remanence relative to untreated NRM intensity may initially increase, also revealing the presence of overprints. A smooth demagnetization profile (negative slope) indicates the successful removal of overprints. All NRM data presented in this study are from the 25.0 mT demagnetization step, since Zidjerveld plots generally showed the removal of overprints by this point, and magnetization intensity generally remained above 50%, sufficient for paleomagnetic analysis (C. Heil, 2002, pers. comm.). Of 1041 data points only 43 (4.3%) had magnetic intensities less than 50% of the untreated sediment following the 25.0 mT demagnetization step. Most of these points fell between 140-200 cm. The 300 cm Zidjerveld plot shows unstable magnetic behavior following the 40.0, 50.0 and 60.0 mT demagnetization steps. Because this region of the core yielded a low absolute NRM intensity signal, however, the signal-:noise ratio is very small. Indicators of reduction diagenesis characterize this core interval, including the dominance of large magnetic grains carrying the remanence (see section 3.2). Demagnetization of multidomain (MD) grains is a stochastic process due to the unpredictable component of domain wall movements (J. King, 2002, pers. comm.). The 300 cm Zidjerveld plot at center shows the effects of MD grain demagnetization and background noise influencing magnetization signals following high peak field demagnetization steps and therefore does not render the 25.0 mT data unsuitable for paleomagnetic interpretation (J. King, 2002, pers. comm.).

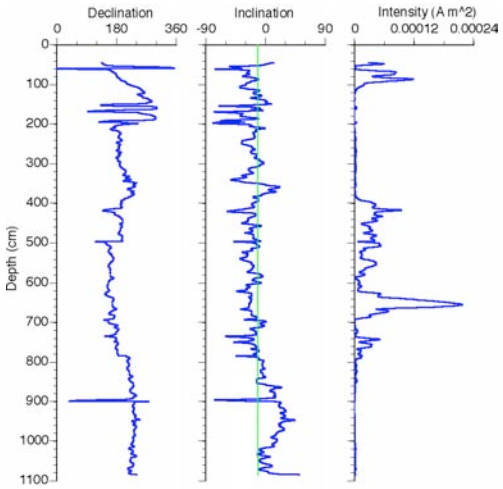

Figure 10. Representative Zidjerveld plots and AF demagnetization curves showing typical magnetic behavior of T97-52V sediments for 100 cm (top), 300 cm (middle), and 650 cm (bottom) core depths. Plots depict stepwise demagnetization up to 60.0 mT. X, Y, and Z refer to the three orthogonal directions of magnetization measured by SQUIDs, and H is the resultant vector of X+Y. X vs. Y represents the horizontal plane and H vs. Z represents the vertical plane (C. Heil, pers. comm., 2002). M_0 indicates untreated NRM in Zidjerveld plots.

2.4. Age models

Williamson et al (1991) conducted a ~ 25 ka paleomagnetic examination of core MPU12 from the southern Lake Tanganyika basin, but due to sediment disturbance and anomalous radiocarbon dates the age model in their study was based on PSV correlation with the Lake Barombi Mbo (4.5° N, 9.5°--Figure 5) record from core BM6 (Thouveny and Williamson, 1988). Therefore a PSV age model for core T97-52V was also constructed by direct comparison to BM6 PSV data. Correlative tie points were drawn by visual curve matching (Figure 11) and inclination records from the two cores were used to construct an age-depth model (Figure 12). Inclination was chosen for correlation rather than declination since T97-52V shows more pronounced variation in inclination, and obvious tie

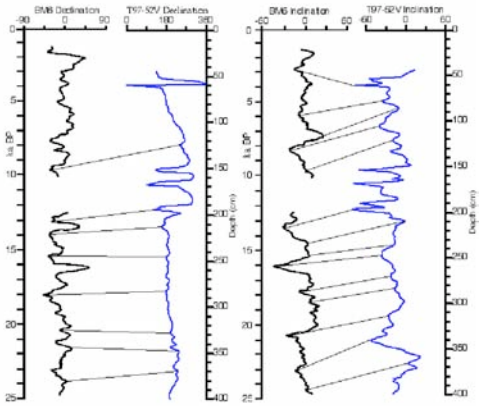

Figure 11. Inclination and declination from T97-52V correlated with core BM6 inclination and declination. Tie lines were established through visual curve matching. The correlated inclination records were used to construct a ~25 ka age-depth model (Figure 12). BM6 curves from Thouveny and Williamson, 1988, who dated core BM6 through a combination of radiocarbon dates and PSV correlation with the European record.

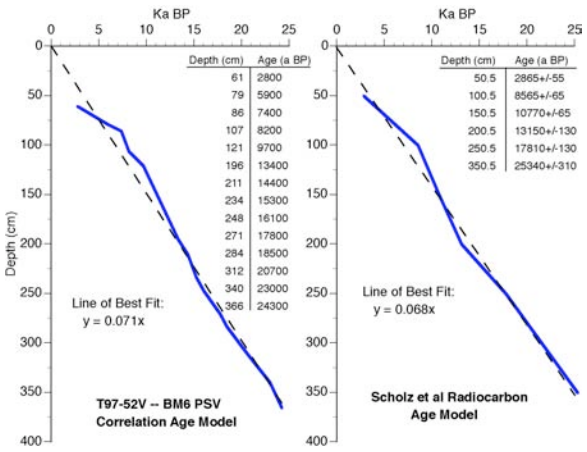

Figure 12. Comparison of the BM6--T97-52V inclination correlation age model and the upper ~25 ka of the Scholz et al (in press) radiocarbon age model. Best-fit lines have nearly identical slopes, indicating close correspondence of depths and modeled ages.

lines were easily established above the large break in core BM6 for inclination records but not for declination. The calibrated upper ~25 ka (Bard, 2001) of the Scholz et al (2002, in press) ^{14}C age model is also shown. Closely agreeing approximate lines of best fit were drawn for each age model. No other long-range (greater than ~50 ka) lacustrine paleomagnetic records exist within the 3000-4000 km effective radius of PSV correlation for the T97-52V site. But marine core MD85-668, collected in the Somali Basin (0.1° N, 46.0° E--Figure 5), has a low resolution inclination record extending over the last ~140 ka and is close enough to Lake Tanganyika for comparison (Meynadier et al, 1992). This record was used to construct an~80 ka PSV age model for T97-52V, which was subsequently compared to the Scholz et al (2002, in press) model (Figures 13 and 14). Curve smoothing of T97-52V inclination data using a 13 data point window allowed correlation of this high-resolution Lake Tanganyika record and the lower resolution marine record. The unconformity at 940 cm in T97-52V prevented establishment of inclination tie lines between cores for the lower section of T97-52V, rendering impossible the extension of the PSV age model below 940 cm.

2.5. Environmental magnetic measurements

Environmental magnetic analysis uses measurements of magnetic concentration, magnetic grain size, and magnetic mineralogy in sediments as proxies for paleoenvironmental variations (King and Channel, 1991). Changes in these parameters allow investigators to determine climate driven environmental changes in sediment provenance, weathering and erosion, sediment transport, depositional environment, and postdepositional processes (Verosub and Roberts, 1995). Low frequency volumetric susceptibility (K), anhysteretic remanent magnetization (ARM), and

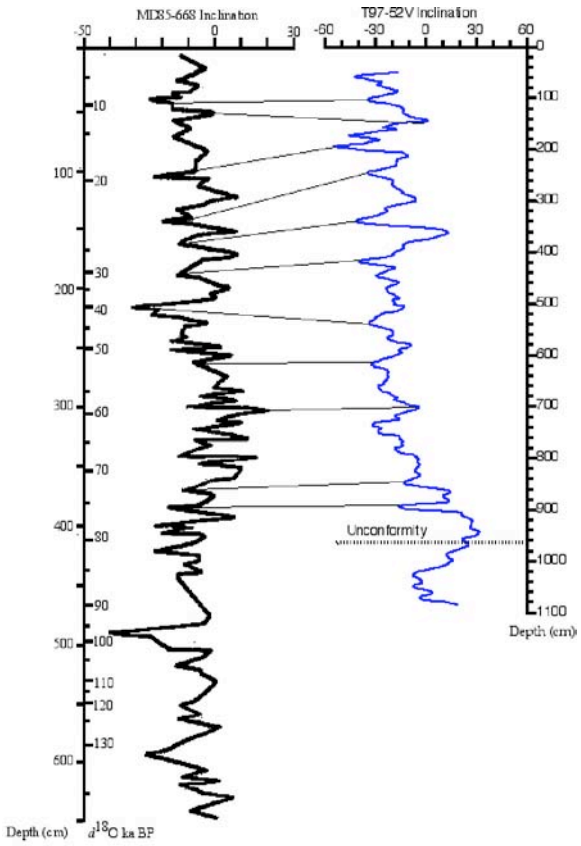

Figure 13. Correlated inclination from T97-52V and core MD85-668 from the Somali Basin. Tie lines were established through visual curve matching. An ~80 ka age-depth model was constructed using the correlated inclination records (Figure 14). T97-52V data were smoothed using a 13 data point window. MD85-668 curve and $\delta^{18}O$ time scale from Meynadier et al, 1992.

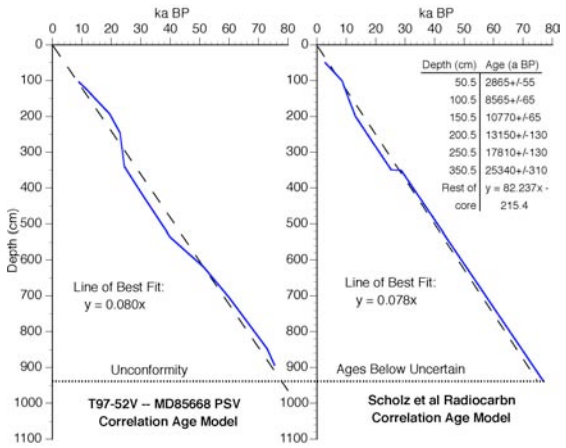

Figure 14. Comparison of the MD85-668--T97-52V inclination correlation age model and the upper ~80 ka of the Scholz et al (in press) radiocarbon age model. Below 350 cm Scholz et al used a linear regression of radiocarbon dates to construct their lower age model. Best-fit lines have nearly identical slopes, indicating close correspondence of depths and modeled ages.

isothermal remanent magnetizations (IRMs) were imparted and measured in the laboratory and used to produce environmental magnetic data.

Susceptibility is a very weak magnetization measured in the presence of its inducing field, and disappears when the field is removed (Thompson and Oldfield, 1986). Susceptibility was measured at 1 cm intervals using the susceptibility point sensor of a GEOTEK Multisensing Core Logger immediately after the core was split (Scholz et al, 2002 in press). Susceptibility data serve as average indicators of ferrimagnetic mineral concentrations in the sediment, and tend to show sensitivity toward MD and large pseudo-single domain (PSD) magnetic grains due to their large volumes relative to single domain grains (King et al, 1982).

IRMs were imparted in +Y and -Y directions with a Cenco electromagnet and Variac 230V power source. Saturation IRM (SIRM) was imparted with a dc field of 1200 mT in the +Y direction, measured, and then subjected to stepwise AF demagnetization identical to that performed during NRM data acquisition. SIRM also serves as a magnetic concentration indicator, but in ratios with other measurements it can help reveal variations in magnetic grain size and mineralogy (Thompson and Oldfield, 1986). After samples underwent AF demagnetization of SIRM they were resaturated at a field of 1200 mT, after which back IRM (BIRM) was imparted at 300 mT in the -Y direction, measured, and again subjected to stepwise demagnetization up to 60.0 mT. The hard IRM (HIRM) parameter was then calculated: HIRM=(SIRM+BIRM)/2. HIRM measures concentrations of high coercivity canted antiferromagnetic minerals, since lower coercivity minerals are saturated by the 1200 mT field in the +Y direction and also saturated by the 300 mT field in the -Y direction, effectively canceling their contribution to HIRM (King and Channel, 1991). The S parameter was also calculated: S=BIRM/SIRM. This ratio measures amounts of ferrimagnetic minerals (such as magnetite) relative to canted antiferromagnetic minerals (such as hematite and goethite). Values close to one indicate that magnetite-like minerals carry most of the remanence, while values less than one represent much greater proportions of canted antiferromagnets. The S ratio takes advantage of the much lower coercivities and much stronger remanent magnetizations of ferrimagnetic minerals to characterize magnetic mineralogy (Verosub and Roberts, 1995).

ARM was imparted along the Z axis with a dc field of 0.1 mT, similar in intensity to the geomagnetic field (Verosub and Roberts, 1995), in the presence of a steadily decreasing AF field with a 100.0 mT peak intensity. K_{ARM}, the susceptibility of ARM, is ARM intensity acquired per unit of dc bias field. K_{ARM} is sensitive to single domain and small pseudo-single domain magnetic grains (Verosub and Roberts, 1995), since the weak dc field used to impart ARM is insufficient to completely realign magnetic domain walls in larger grains (J. Peck, 2002, pers. comm.). Since susceptibility shows sensitivity towards larger magnetic grain sizes, the ratio K_{ARM}/K provides a technique for determining average magnetic granulometry, and varies inversely with grain size (King et al, 1982).

2.6. Environmental magnetic data

Environmental magnetic data are presented in Figure 15, and their significance for inferring regional climate change will be addressed in section 3. All mineral magnetic parameters behaved congruously over the same core intervals, suggesting that the same environmental factors could be responsible for their variations.

All four signals display noisy data through the top 20 cm of the core. HIRM goes to zero from 50-60 cm corresponding to a sharp and drastic minimum in the S ratio. K_{ARM}/K shows sharp spikes in both directions during this section, and K shows values close to or below 0 in the top 20 cm.

During the interval 60-100 cm K shows a broad peak centered at about 85 cm. This range of positive susceptibility values corresponds to S parameter values of close to 1 and to two wide peaks in HIRM. K_{ARM}/K shows high values relative to the rest of the core at 60 cm, but these values decrease to a minimum near 110 cm, followed by a sharp spike at 120 cm.

The region from100-120 cm marks a transition period in which the S ratio switches from small fluctuations between 0.8 and 0.9 to rapid, high-magnitude oscillations, and were HIRM steadily decreases to near 0. At 120 cm K becomes negative and varies minimally down core to 200 cm. S continues noisily fluctuating around a median value of approximately 0.7 from 130 cm to nearly 400 cm down core. S goes to zero at 200 cm, then rises sharply to near 1 around 210 cm, and drops again to 0.2 at 218 cm. K_{ARM}/K and HIRM both show drastically attenuated and monotonous signals between 120-200 cm.

The data from 200-380 cm show K increasing from negative to positive values with small fluctuations. K_{ARM}/K shows increased values barely above 0 through the same interval. In addition, a sharp peak in K_{ARM}/K well above the low surrounding values occurs at 210-224 cm. HIRM from 200-380 cm also rises slightly above its near-zero signal between 120-200 cm.

At 400 cm the apparent median value for S ratio fluctuations changes to close to 1, although noisy oscillations increase in magnitude, especially towards larger values, reaching 1.8 at 418 cm. But at 500 cm S becomes stable, varying around 0.9 and 1 down core to 690 cm. HIRM, K, and K_{ARM}/K all show long intervals of markedly higher values from 390-690 cm. These three signals do fluctuate in intensity from 390-690 cm but remain significantly above 0 throughout the section. Variations in the relative sizes and timing of local maxima and minima are obviously coherent between 390-690 cm.

S decreases from values near 1 to around 0.7 between 690-730 cm. Drastic attenuation of HIRM and K_{ARM}/K occurs throughout this interval. K plunges to 0 just below 700 cm and immediately begins to increase again.

Between 730-790 cm all four measurements go through four rapid oscillations of differing intensity with the maximum peak just below 740 cm.

From 790 cm to the bottom of the core, including the 940 cm discontinuity, the S ratio varies minimally near 1. HIRM shows a slight signal from 790-880 cm, is essentially 0 from 880-1000 cm, and then fluctuates with very low-amplitude to the core bottom. K_{ARM}/K similarly shows a weak signal down to about 910 cm, after which point this parameter permanently remains at 0. K decreases steadily from a low positive value at 790 cm to -2 at the 940 cm unconformity. K then rapidly jumps to a relatively high value, and remains high throughout the rest of the core.

3. Discussion

3.1. Paleomagnetic results

Noisy paleomagnetic data between 40-60 cm coheres with the unstable behavior of mineral magnetic properties in this section. The observed wild fluctuations are spurious data caused by physical disturbance of the sediment during the vibracoring process. The coring equipment liquefied the top 40 cm of the core, which were not recovered from the field. Accurate data begins at 60 cm.

High-magnitude variations in declination and inclination between 140-210 cm correspond to a period of extremely low NRM intensity and negative K values. This suggests that unstable directional signal fluctuations are caused by background noise influencing an interval of low magnetization and magnetic concentration.

Initial measurements of declination data from core sections 3 and 4 (498-784 cm) appeared offset by approximately 180° from the rest of the core. Data were reversed 180° to correct for the apparent sampling from wrong split core halves, but the resulting declination data presented in this paper are about 30° below typical data for the rest of the core. Uncertain sampling procedures therefore render declination data poorly suited for confident use between 498-794 cm. But inclination records showed no anomalous behavior during this interval, and using the wrong core halves would produce no difference in the recorded vertical field component. Inclination data were therefore used with confidence.

Possible causes for the large negative spikes in inclination and declination just above 900 cm remain ambiguous, but the large amplitudes and miniscule durations of these minima suggest that these data are spurious. The cause of these peaks is not well understood.

Paleomagnetic directional data were used to construct the age models presented in section 2.4. Lines of best fit clearly show close agreement between depths and corresponding modeled ages. The two PSV age models, constructed independently by correlation to two cores dated by different methods, corroborate the radiocarbon time scale presented by Scholz et al (2002, in press) for the calibrated upper ~25 ka and extrapolated~80 ka. This validation of the established T97-52V age model adds to its robustness and confirms its dates for paleolimnological and paleoclimatological interpretations of other data for the past ~80 ka.

Ages for the bottom 140 cm of the core below the unconformity remain unconstrained. PSV data can add no clarity to this problem since correlation with core MD85-668 proved impossible. Further long-range paleomagnetic data from equatorial Africa are needed to establish a firm regional PSV time scale.

The peak in inclination between 950-960 cm could represent the signal of a geomagnetic excursion such as the Blake event (Jacobs, 1994). Inclination reaches a value of 52° at this point, a deviation of 63.8° from predicted GAD inclination of –11.8°. The possibility of an excursion as a stratigraphic control point was not investigated in depth in the present study, however, due to the lack of a concurrent large anomaly in declination and since mineral magnetic data and the NRM intensity signal show extreme alteration of magnetic sediments during this interval.

3.2. Environmental magnetic results

General trends in mineral magnetic data appear between 60-120 cm (segment A), 120-380 cm (segment B), 380-690 cm (segment C), and 690 cm down to the 940 cm unconformity (segment D). K values in segments A and C indicate measurable concentrations of magnetic minerals, and K_{ARM}/K data show that fine grain sizes dominate these intervals relative to segments B and D, except for the four oscillations between 730-790 cm in segment D. The S ratio shows that ferrimagnets carry the majority of the remanence in segments A and C. But canted antiferromagnets contribute sizably to the volume of magnetic minerals, as revealed by HIRM values in segments A and C. These patterns indicate that sediments originally deposited at the core site remained unaltered and contained the minerals measured in data acquisition procedures for segments A and C.

Although HIRM is low in segment B, decreased and noisy S ratio values suggest relatively elevated contributions of canted antiferromagnetic minerals to carrying the remanence. K_{ARM}/K data reveal large grain sizes bearing the remanence, and negative K values show extremely low magnetic concentrations through this section. These data display characteristic mineral magnetic signatures of reduction diagenesis (King and Channel, 1991). Sharp transitions in K, HIRM, and K_{ARM}/K, and the abrupt switch from mild oscillations in the S parameter to higher-amplitude variations indicate down-core diagenetic filtering of magnetic signals (J. King, 2002, pers. comm.). In this process magnetic material in the sediment is rapidly removed just below the upper horizon of strong magnetization when the majority of Fe^{3+} in fine-grained remanence-carrying particles is reduced under anoxic conditions (Karlin and Levi, 1983). It is possible that the authentic mineral magnetic data in segment A therefore cannot be compared using a uniformitarian approach to data down-core, since the geologically recent segment A

sediment may not have been exposed to in situ conditions long enough for reduction diagenesis to result. A degree of caution must therefore accompany assertions regarding segment A.

Reduction diagenesis typically indicates dissolution and pyritization of iron minerals in deep anoxic sedimentary basins (Levi and Karlin, 1983), suggesting attenuation of NRM intensity and mineral magnetic parameters from 120-380 cm may evidence water depths at core site T97-52V well in excess of Lake Tanganyika's 150 m-deep oxygenated-anoxic transition zone. An alternate explanation is also feasible. Lake Tanganyika becomes a closed basin with only slight lowering of lake level (Cohen et al, 1997a). Intense evaporation in closed-basin lakes can lower lake level and consequently increase salinity to the point that a permanent halocline develops, below which level shallow bottom waters are anoxic (J. King, 2002, pers. comm.). In this scenario reduction diagenesis could occur despite lake levels shallower than 150 m at the KIR. The existence of evaporite minerals in conjunction with pyrite and dark-green mud in Lake Tanganyika core MPU12 suggests that this hypothesis warrants further investigation (Vincens et al, 1993).

A consensus exists among climate researchers that Lake Tanganyika water levels have fluctuated over the last 30 ka, but reached a low stand ~18 ka BP corresponding to the Last Glacial Maximum (Scholz and Rosendahl, 1988, and references therein). Multifold evidence suggests water levels similar to the modern high stand existed by ~12 ka (e.g. Gasse et al, 1989; Vincens et al, 1993, Scholz et al, 2002, in press). Constraining lake level fluctuations in segment B proves impossible due to natural "clipping" of magnetic environmental proxy data by reduction diagenesis (J. King, 2002, pers. comm.). Since the precise cause of reduction diagenesis remains unclear for T97-52V, the present study cannot legitimately evaluate lake level for the past ~30 ka with mineral magnetic data.

However, further analysis of the spike in K_{ARM}/K near 220 cm may add some clarity to this situation. Indication of small grain sizes here introduces the possibility that anaerobic or microaerophyllic magnetogenic bacteria could have influenced reduction processes and the magnetic signal (Hesse and Stolz, 1999). Magnetic extraction, x-ray diffraction, and electron microscopy are needed to examine the possible presence of magnetosomes at this horizon. An ulterior hypothesis is that abiotic precipitation of iron-manganese minerals at the sediment eH-pH threshold boundary could have been responsible for this signal (J. Peck, 2002,pers. comm.).

Interval C is interpreted as an extended period (~31-57 ka) of lake level fluctuations around an average medium depth. Lake levels stood low enough that meromictic conditions ceased and bottom waters became mixed and oxygenated, yet Lake Tanganyika remained deep enough that hemipelagic deposition of mud-sized sediments still dominated. By this reasoning increases in K_{ARM}/K show lake level was higher than the mean, and decreases in this grain size parameter indicate slightly lower lake levels and a consequent higher component of larger-grained terrestrial sediment input. This interpretation takes into account mineral magnetic indications that magnetic signals appear authentic and unaltered by reduction diagenesis. In segment C the S ratio is near 1, K values are positive, and K_{ARM}/K, HIRM, and K exhibit close correlation throughout this interval. Segment C partially overlaps Scholz et al's (2002, in press) section II, which, based on organic carbon proxies, was interpreted as representing increased mixing due to slightly lower lake levels than at present and possibly increased winds.

Corresponding oscillations in all mineral magnetic parameters between 730-790 cm are poorly understood. The largest peak centered on 740 cm corresponds in stratigraphic level to the Heinrich event H6 visible in total organic carbon and $\delta^{13}O$ signals of Scholz et al (2002, in press). This brief period of quasi-cyclic oscillations deserves further investigation.

Below 800 cm monotonous signals of reduction diagenesis once again dominate mineral magnetic trends. NRM intensity has been virtually obliterated from 800 cm to the bottom of the core as well. Flat lines in paleomagnetic and mineral magnetic data indicate some form of signal disruption, probably reduction diagenesis, since a certain amount of variation typically characterizes these data (J. King, pers. comm., 2001). The absence of significant magnetic signals below 800 cm prevents paleolimnological or paleoclimatological evaluations of the data.

3.3. Evidence for high-latitude climate control

Despite the impossibility of gleaning information about specific environmental processes from the magnetic data, general trends showing either preservation of magnetic records or destruction of magnetic minerals by diagenesis indicate that global ice volume have influenced equatorial African climates over the past ~80ka. Transitions between segments A, B, C, and D were separated by dashed horizontal lines (Figure 15), and the timings of these transitions were determined using the PSV-corroborated radiocarbon time scale for T97-52V. The abrupt transitions between magnetic data segments are interpreted as the transitions between high-latitude stadial-interstadial stages. Magnetic segment transitions have ^{14}C ages ~2-3 ka younger than corresponding marine oxygen isotope dates for stadial-interstadial stage transitions (Figure 16). Therefore I propose the signature of northern-latitude climatic variations affecting ice mass also influenced tropical African climate over the past ~80 ka, but with a 2-3 ka time lag. Magnetic signals do not directly indicate specific paleoenvironmental processes that have affected the T97-52V location, but these data still serve as general paleoenvironmental proxies since, since sedimentation and diagenesis both depend on climatically driven weathering, erosion, and hydrologic processes. Mineral magnetic signals reflect stadial-interstadial African equatorial climatic changes, although they do not indicate the precise effects of these changes.

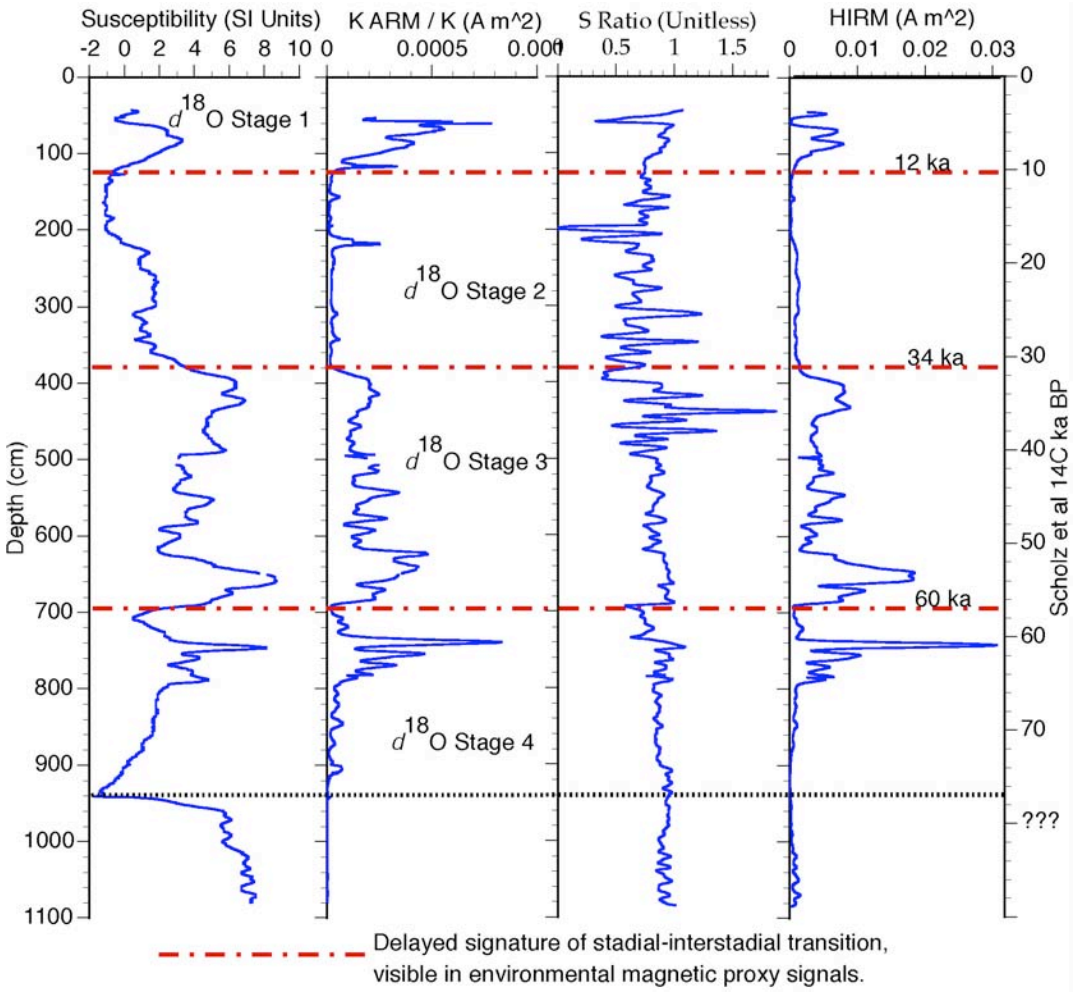

Figure 15. Plots of environmental magnetic parameters for T97-52V. See text for discussion. Note that X-axes for K_{ARM}/K, S ratio, and HIRM have a left-hand value of 0, but the K X-axis ranges from -2 on the left-hand side. Horizontal dashed lines indicate stadial-interstadial climate transitions and are discussed in section 3. Notice that these indicators of regions of generally similar data correspond exactly to the NRM intensity signal in Figure 9. Age model on the right-hand side from Scholz et al (2002, in press).

The same stadial-interstadial trend appears in the NRM intensity signal (Figure 17). Pictured along with NRM intensity is NRM/ARM, a parameter typically used to examine relative paleointensity of the geomagnetic field (King and Peck, 2001). However, this ratio can only accurately show field strength changes over time if magnetic concentration, grain size, and mineralogy remain consistent throughout the data set (King et al, 1983). The NRM intensity data presented in this paper meet none of these criteria and vary greatly due to climatically driven sedimentation and diagenesis processes (J. King, 2002, pers. comm.). But the NRM/ARM data do reveal a perplexing quasi-periodic pattern especially visible between 80-200 cm, and 400-520 cm. Although reduction diagenesis has altered the signal between 120-380 cm, NRM/ARM calculations in this region can safely be used, since both remanences are obtained at similar field intensities, and both NRM and ARM display similar signal intensities over coherent intervals. NRM/ARM values evidence this fact since they fluctuate around similar relative values for the entire core. Preliminary spectral analysis indicates power at ~22 cm, or ~1.8 ka according to the Scholz et al (2002, in press) age model (Figure 18). Since NRM intensity and ARM both vary depending on climatically influenced sediment properties, this periodicity suggests millennial scale high-latitude Dansgaard/Oeschger (D/O) oscillations may influence the Lake Tanganyika sediment record through a climatic teleconnection (Bond et al, 1999). Whether these apparently periodic oscillations lag behind dated high-latitude D/O cycles remains unclear and provides an impetus for further analysis.

Notice that the delayed signal for the onset of $\delta^{18}O$ stage four (76 ka) is absent in mineral magnetic and NRM intensity data. Following the trend of clear magnetic indications of transitions between $\delta^{18}O$ stages higher in the core, a clear manifestation from stage five

to stage four is expected between 73-74 ka on the PSV-affirmed radiocarbon age model. Negative K values and HIRM measurements at 0 from 900-940 cm, as well as a decrease in K_{ARM}/K to values near 0 indicate severe diagenetic alteration of magnetic material jut above the discontinuity. Reduction diagenesis could have played a role in destroying the magnetic indicators of a climatic transition. The unconformity reveals a probable erosional period in which core site T97-52V became subaerially exposed (Scholz and Rosendahl, 1988), so the stadial-interstadial signature also could have been eliminated by physical sedimentation processes during recurrent deposition above the hiatus prior to reduction diagenesis. The robust PSV-radiocarbon age model indicates deposition resumed ~77 ka. The absence of a clear stadial-interstadial transition in magnetic data does not invalidate the argument for high-latitude climate forcing, since such transitions prominently appear higher in the core, and the unconformity itself results from a climatically-induced lake level change. Further examination of the unconformity in other sediment cores is needed to elucidate this issue.

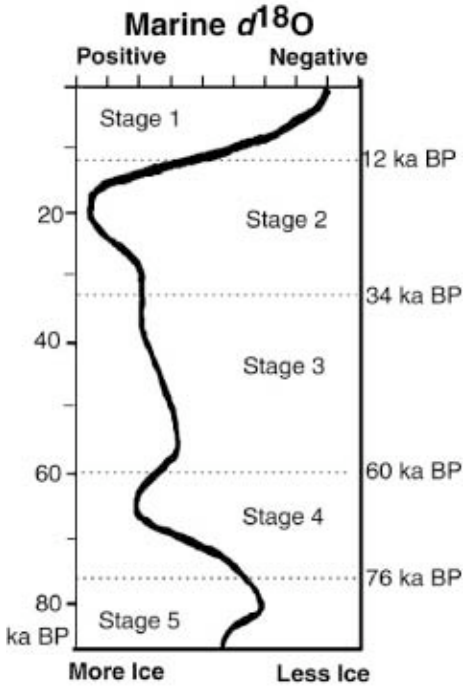

Figure 16. Diagram of marine oxygen isotope time scale for the last 80 ka. Astronomical orbital cycles, whose timings have been precisely and accurately calculated, control global ice volume, which dominantly influences marine oxygen isotope ratios (Imbrie and Imbrie, 1979). More positive $\delta^{18}O$ ratios indicate its enrichment in seawater due to preferential evaporation of $\delta^{16}O$ and trapping of the lighter isotope in increased volumes of glacial ice. The astronomical control of stadial-interstadial fluctuations has been utilized to construct this high-accuracy, high-resolution time scale. Figure modified from Ruddiman, 2001. Dates from Bond et al, 1999.

4. Conclusions

This paper uses long-range paleosecular variation data from a sediment core dated previously using an extrapolated radiocarbon age model to construct ~25 ka and ~80 ka PSV age models for the core. These PSV data and age models supply an important data set for equatorial Africa, where such records are lacking. Paleomagnetic age models in this study readily affirm the accuracy of the Scholz et al (2002, in press) ^{14}C age model for core T97-52V.

Mineral magnetic data prove unsuitable for paleolimnological and paleoclimatological analysis throughout much of the core due to attenuated signals resulting from reduction diagenesis. Useful data were obtained for the interval 380-690 cm, which is interpreted as a period of lake levels fluctuating around an average lower than the present water surface elevation. General trends in the patterns of mineral magnetic data segments and intervals of NRM intensity data indicate that climatically driven sedimentation/diagenesis processes in equatorial Africa followed stadial-interstadial climatic transitions over the past ~80 ka with a 2-3 ka lag time. Possible NRM/ARM cyclicity with a period of ~1.8 ka may indicate the influence of Dansgaard/Oeschger oscillations on

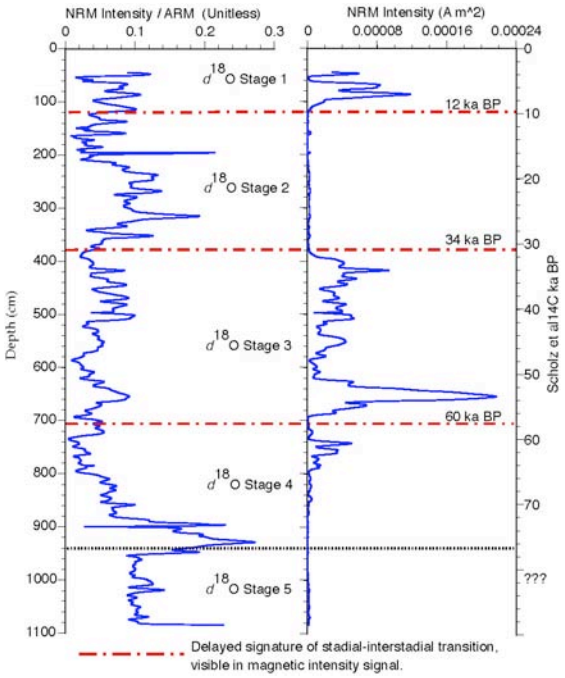

Figure 17. Diagram of NRM intensity and NRM/ARM. NRM intensity shows the same general stadial-interstadial signal variations over segments A, B, C, and D as the four mineral magnetic parameters in Figure 15. Horizontal lines represent these delayed transitions, and dates for these transitions compared to the radiocarbon time scale come from the marine oxygen isotope record. Quasi-periodic ~22cm oscillations in NRM/ARM could represent teleconnections from high latitudes of Dansgaard/Oeschger climate fluctuations.

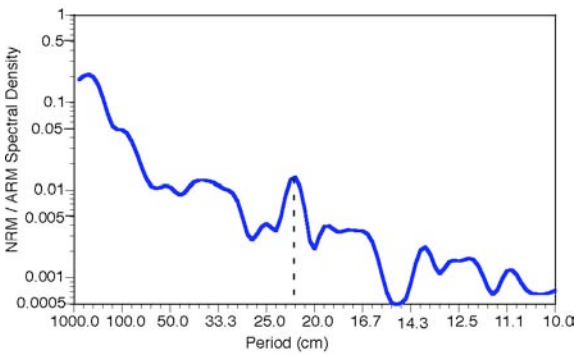

Figure 18. Spectral analysis diagram indicating significant power above the red noise spectrum at a period of ~22 cm in the NRM/ARM ratio. This period corresponds to a time periodicity of ~1800 years using the Scholz et al (2002, in press) radiocarbon time scale (see Figure 14). Since high latitude processes are shown to influence tropical African climates, these quasi-cyclic fluctuations, presumably a result of climatically controlled sedimentation/diagenesis activity, could correspond to Dansgaard/Oeschger high-latitude climate oscillations.

tropical African climate as well. This evidence shows high-latitude forcing of tropical African climate changes over the past ~80 ka.

The signature of stadial-interstadial transitions preserved in the mineral magnetic and NRM intensity data further confirm paleosecular variation age models and the established radiocarbon age model. The ages of these sedimentary climate proxy transitions are determined using the PSV-validated T97-52V ^{14}C age model, which exhibits close agreement with the high-accuracy marine $\delta^{18}O$ time scale taking into consideration the climate-forcing lag time.

Acknowledgments. I thank Dr. John King for providing me with this opportunity and answering many questions, Chip Heil for help with magnetic techniques, answering all my questions, and giving insight and advice, Carol Gibson for help with computers and general troubleshooting, Kathryn Ford and Brad Hubeny for advice, Rhonda Kenny for help locating background information, Scott Rutherford for assistance with spectral analysis software, and the PELL Marine Library staff for obtaining references for me. I am grateful to Rob Pockalny for making location maps presented in this paper and coordinated the 2002 SURFO program with assistance from Kelly Kriner, and Kim Carey. This research experience was made possible through a grant from the National Science Foundation.

References

Bard, E., Extending the calibrated radiocarbon record, *Science, 292*, 2443-2444, 2001.

Bergonzini, L., Chalie, F., and Gasse, F., Paleoevaporation and paleoprecipitation in the Tanganyika basin at 18,000 years B.P. inferred from hydrologic and vegetation proxies, *Quat. Res., 47*, 295-305, 1997.

Bradley, R.S., *Paleoclimatology: Reconstructing Climates of the Quaternary*, Academic Press, San Diego, California and London, 613 p., 1999.

Bond, G.C., Showers, W., Elliot, M., Evans, M., Lotti, R., Hajdas, I., Bonani, G., and Johnson, S., The North Atlantic's 1-2 kyr climate rhythm: relation to Heinrich events, Dansgaard/Oeschger cycles, and the Little Ice Age, in *Mechanisms of Global Climate Change at Millennial Time Scales, Geophysical Monograph 112*, edited by P.N. Clark, R.S. Weber, and L.D. Keigwin, pp. 35-58, American Geophysical Union, Washington, D.C., 1999.

Butler, R.F., *Paleomagnetism: Magnetic Domains to Geologic Terranes*, Blackwell Scientific Publications, Boston, USA, 319 p., 1992.

Cohen, A.S., Talbot, M. R., Awramik, S.M., Dettman, D.L., and Abell, P., Lake level and paleoenvironmental history of Lake Tanganyika, Africa, inferred from Late Holocene and modern stromatolites, *GSA Bull., 109*, 444-460, 1997a.

Cohen, A.S., Lezzar, K., Tiercelin, J., and Soreghan, M., New palaeogeographic and lake level reconstructions of Lake Tanganyika: implications for tectonic, climatic and biologic evolution in a rift lake, *Basin Res., 9*, 107-132, 1997b.

Dearing, J.A., Holocene environmental change from magnetic proxies in lake sediments, in *Quaternary climates, environments, and magnetism*, edited by B. A. Maher and R. Thompson, pp. 231-278, Cambridge University Press, Cambridge, UK, 1999.

DeMenocal, P.B., Plio-Pleistocene African climate, *Science, 270*, 53-59, 1995.

Gasse, F., Ledee, V., Massault, M., and Fontes, J., Water-level fluctuations of Lake Tanganyika in phase with oceanic changes during the last glaciation and deglaciation, *Nature, 342,* 57-59, 1989.

Hecky, R.E., and Degens, E.T., Late-Pleistocene chemical stratigraphy and paleolimnology of the rift valley lakes of Central Africa, *Woods Hole Oceanogr. Inst., Tech. Report No. 73-28*, 93 p., 1973.

Hesse, P., and Stolz, J.F., Bacterial magnetite and the Quaternary climate record, in *Quaternary climates, environments, and magnetism*, edited by B. A. Maher and R. Thompson, pp. 163-198, Cambridge University Press, Cambridge, UK, 1999.

Imbrie, J., and Imbrie, K.P., *Ice Ages: Solving the Mystery*, Enslow Publishers, Short Hills, New Jersey, 224 p., 1979.

Jacobs, J.A., *Reversals of the Earth's Magnetic Field*, Cambridge University Press, Cambridge, UK, 346 p., 1994.

Karlin, R., and Levi, S., Diagenesis of magnetic minerals in Recent haemipelagic sediments, *Nature, 303*, 327-330, 1983.

King, J.W., Banerjee, S.K., Marvin, and Ozdemir, O., A comparison of different magnetic methods for determining the relative grain size of magnetite in natural materials: some results from lake sediments, *Earth Planet. Sci. Lett., 59*, 404-419, 1982.

King, J.W., Banerjee, S.K., Marvin, J., and Lund, S., Use of small-amplitude paleomagnetic fluctuations for correlation and dating of continental climatic changes, *Palaeogeog. Palaeoclim. Palaeoecol., 42*, 167-183, 1983.

King, J. W., and Channell, J.E.T., Sedimentary magnetism, environmental magnetism, and magnetostratigraphy, *Rev. Geophys., Suppl., April 1991, U.S. National Report to International Union of Geodesy and Geophysics 1987-1990*, 358-370, 1991.

King, J., and Peck, J., Use of paleomagnetism in studies of lake sediments, in *Tracking Environmental Change Using Lake Sediments. Volume 1: Basin Analysis, Coring, and Chronological Techniques*, edited by W.M. Last and J.P Smol, pp. 371-389, Kluwer Academic Publishers, Dordrecht, The Netherlands, 2001.

Lezzar, K.E., Tiercelin, J., De Batist, M., Cohen, A.S., Bandora, T., Van Rensbergen, P., Le Turdu, C., Mifundu, W., and Klerkx, J., New seismic stratigraphy and Late Tertiary history of the North Tanganyika Basin, East African Rift system, deduced from multichannel and high-resolution reflection seismic data and piston core evidence, *Basin Res., 8*, 1-28, 1996.

McElhinny, M.W., *Paleomagnetism and Plate Tectonics*, Cambridge University Press, Cambridge, UK, 358 p., 1973.

McIntyre, M., and Molfino, B., Forcing of Atlantic equatorial and subpolar millennial cycles by precession, *Science, 274*, 1867-1870, 1996.

Merrill, R.T. and McFadden, P.L., Paleomagnetism and the nature of the geodynamo, *Science, 248*, 345-350, 1990.

Meynadier, L., Valet, J., Weeks, R., Shackleton, N.J., and Hagee, V.L., Relative geomagnetic intensity of the field during the last 140 ka, *Earth Planet. Sci. Lett., 114*, 39-57, 1992.

Pokras, M. P., and Mix, A.C., Earth's precession cycle and Quaternary climatic change in tropical Africa, *Nature, 326*, 486-487, 1987.

Ruddiman, *Earth's Climate: Past and Future*, W. H. Freeman and Co., New York, 465 p., 2001.

Scholz, C.A., and Rosendahl, B.R., Low lake stands in Lakes Malawi and Tanganyika, East Africa, delineated with multifold seismic data, *Science, 240*, 1645-1648, 1988.

Scholz, C. A., King, J.W., Swart, P.K., Colman, S., Forcing mechanisms of tropical continental climate: deciphering a 100 kyr record of limnological change from Lake Tanganyika sediment cores, *Proposal # ATM-981-3970 to the National Science Foundation*, 1998.

Scholz, C.A., King, J.W., Ellis, G.S., Swart, P.K., Stager, J.C., Colman, S.M., Paleolimnology of Lake Tanganyika, East Africa, over the past 100 kYr, *Paleolimnology, in press*, 2002.

Schulz, H., Von Rad, U., and Erienkeuser, H., Correlation between Arabian Sea and Greenland climate oscillations of the past 110,000 years, *Nature, 393*, 54-57, 1998.

Thompson, R., Geomagnetic evolution: 400 years of change on planet Earth, *Phys. Earth Planet. Int., 36*, 61-77, 1984.

Thompson, R., and Oldfield, F., *Environmental Magnetism*, Allen and Unwin, London, 227 p., 1986.

Thouveny, N., and Williamson, D., Palaeomagnetic study of the Holocene and Upper Pleistocene sediments from Lake Barombi Mbo, Cameroun: first results, *Phys. Earth Planet. Int., 52*, 193-206, 1988.

Verosub, K.L., Depositional and postdepositional processes in the magnetization of sediments, *Rev. Geophys. Space Phys., 15*, 129-143, 1977.

Verosub, K., L., and Roberts, A.P., Environmental magnetism: past, present, and future, *Jour. Geophys. Res., 100*, 2175-2192, 1995.

Vincens, A., Chalie, F., Bonnefille, R., Guiot, J., and Tiercelin, J., Pollen-derived rainfall and temperature estimates from Lake Tanganyika and their implication for Late Pleistocene water levels, *Quat. Res., 40*, 343-350, 1993.

Walker, B., High-resolution paleomagnetic analysis of a sediment core from Lake Bosumtwi, Ghana, in *Papers from the Summer Undergraduate Research Fellowship Program in Oceanography, 2001. Graduate School of Oceanography, University of Rhode Island, Narragansett, RI, GSO Technical Report 2001-02.*, pp. 46-56, 2001.

Williamson, D., Thouveny, N., Hillaire-Marcel, C., Mondeguer, A., Taieb, M., Tiercelin, J., and Vincens, A., Chronological potential of palaeomagnetic oscillations recorded in late Quaternary sediments from Lake Tanganyika, *Quat. Sci. Rev., 10*, 351-361, 1991.

Williamson, D., Taieb, M., Damnati, B., Icole, M., and Thouveny, N., Equatorial extension of the younger Dryas event: rock magnetic evidence from Lake Magadi (Kenya), *Glob. Planet. Change, 7*, 235-242, 1993.

Williamson, D., Jelinowska, A., Kissel, C., Tucholka, P., Gibert, E., Gasse, F., Massault, M., Taieb, M., Van Campo, E., and Wieckowski, K., Mineral-magnetic proxies of erosion/oxidation cycles in tropical maar-lake sediments (Lake Tritrivakely, Madagascar): paleoenvironmental implications, *Earth Planet. Sci. Lett., 155*, 205-219, 1998.

J. D. Malkovich and J. W. King, Graduate School of Oceanography, University of Rhode Island, Narragansett, RI 02882. (jmalkovi@gac.edu, jking@gso.uri.edu)

A Chemical Sensor to Aid in the Search for Underwater Archaeological Sites

Johanna L. Mathieu[1] and Alfred K. Hanson

Graduate School of Oceanography, University of Rhode Island, Narragansett, Rhode Island

Abstract. This paper investigates the potential application of underwater chemical sensors to underwater archaeology. A model is explained that demonstrates that in ideal circumstances certain archaeologically important metals, namely iron, copper, tin, and lead, corroding in seawater may be detectable using current technology. A design for a copper and iron in situ underwater chemical sensor, which uses chemiluminescence detection methods, and its integration into the AUV REMUS is proposed. A description of the next steps of this project and an overview of other uses for this sensor is included.

1. Introduction

It is a very challenging task to locate underwater archaeological sites. Underwater archaeologists have to work with both oceanographers and engineers to develop efficient and cost effective means of surveying the ocean to look for shipwrecks and other evidence of the human past. Sonar surveys often produce hundreds of potential archaeological sites—some of which are meaningful and most of which are simply anomalies on the sea floor, trash, or nothing at all. Scientists must dig through data and, oftentimes, arbitrarily choose which sites are worth a second look.

Using another sensor in conjunction with a sonar system in an underwater archaeological survey could provide scientists with more information about each individual site and allow them to make better decisions about which sites to go back to. An underwater chemical sensor, which is able to detect certain metals in seawater, used in conjunction with a side-scan sonar system, should be able to detect the chemical signatures of the materials on board a sunken ship and/or the materials the ship is made from. While sonar data only gives us an idea of the seafloor relief, chemical data should give us an idea of what materials are on a site. Importantly, a chemical survey does not require that we disturb the sediments or archaeological artifacts. Collecting chemical data and sonar data simultaneously should be a more time-efficient way to look for underwater archaeological sites. Moreover, it should also be more cost-effective because chemical data has the potential to eliminate many of the later, more thorough investigations of target sites which end up in the discovery of mounds of rocks.

This paper proves the concept that it would be useful and feasible to build a chemical sensor to aid in underwater archaeological searches. We include a summary of the archaeological and chemical investigation we have conducted in order to choose which materials we should attempt to sense chemically. We also present a simplified model that determines whether or not the materials we have chosen might be observable in the vicinity of a shipwreck. Then, we explain which environments would be most appropriate for conducting such a search. Based on this data and current technology in the field of underwater chemical sensing, we propose the design of an underwater copper and iron sensor that uses chemoluminescence detection methods and is able to take chemical measurements in situ continuously, autonomously, and unobtrusively. We include a method for integrating this sensor into the REMUS, a small Autonomous Underwater Vehicle (AUV). Finally, we lay out the next steps of this project and several of the other potential applications of this sensor.

[1]Now at the Massachusetts Institute of Technology

2. Choice of Materials to Detect

We first determined which materials we should attempt to sense chemically in seawater. Not only do these materials need to be historically prevalent on shipwrecks but they also must have chemical principles that allow for their corrosion and adequate dispersion in seawater. In general, ships have been made of and carried both organic materials and metals. We have limited our analysis to metals because organic materials generally do not last as long as metals in oxygenated water. Therefore, we first chose a set of metals to analyze based upon their archaeological importance and then narrowed down this list by looking at how these materials chemically behave in seawater.

2.1. Archaeological Reasons

In antiquity only a handful of metals were intentionally used and understood. These include iron, tin, copper, lead, silver, and gold (Hamilton, 1998). During the Bronze Age, the materials for bronze, copper and tin, were traded across the Mediterranean as oxhide-shaped ingots. Two Bronze Age shipwrecks feature these interesting archaeological artifacts. At Cape Gelidonya 34 copper ingots were found weighing an average of 25 kg each (Pedersen, 2002a). At the Uluburun shipwreck, archaeologists found 11 tons of metal—10 tons were copper and 1 ton was tin (Pedersen, 2002b). Moreover, Cemal Pulak tells us, "Copper ingots have been found all over the Mediterranean Shoreline, reflecting two facts: first, that

most large-scale trade was shipborne; and second that copper ingots were an acceptable form of currency" (Pulak, 1999). In antiquity, silver and gold were transported across the Mediterranean in their raw form, as coins, and as jewelry. Moreover, raw silver and gold were transported in large quantities from the Americas to Europe in more recent times. During Roman times, lead was used for anchors and ship ballast, and also in making pewter, which was commonly traded across the Mediterranean. Lead weights, cannonballs, sheeting, and stripping are commonly found on underwater archaeological sites. Iron is the most common metal found on archaeological sites (Hamilton, 1998). It was used to make weapons and tools, and also fasteners and braces for ships. Therefore, archaeology tells us that the materials we should attempt to look for are iron, tin, copper, lead, silver, and gold.

2.2. Chemical Reasons

In choosing which material to detect it is important to reach a balance between a corrosive material (so that it emits enough particles into the water column for our sensor to detect) and a material that is somewhat resistant to corrosion (so that the material will not have completely corroded away by the time we analyze the site). Gold does not corrode in seawater and therefore we should not build a sensor to look for it. The remaining five metals proposed all corrode in seawater. In general, their corrosion potential from least to most corrosive is: silver, copper, lead, tin, and iron (Hamilton, 1998). However, the actual rate at which they corrode is greatly affected by a variety of environmental factors making it incredibly difficult to predict the amount of corrosion products in the water column around an underwater archaeological site. These factors include oxygen levels, sedimentation and seafloor composition, temperature, pH, depth, current velocity, and plant/animal life. Also, placing two different metals together can affect their corrosion rates. In general, adding a less noble metal to a more noble metal decreases the corrosion rate of the more noble metal (Brown, 2002). This is why zinc is often used in conjunction with steel as a sacrificial anode. Moreover, corrosion rates are generally not constant over time. Usually corrosion it at its highest and then dies off exponentially. This is sometimes due to the fact that corrosion by-products can protect the original material. For instance, a film of cuprous oxide often forms on corroding copper and protects it from further corrosion (Boyd and Fink, 1978). Furthermore, it is possible that metals could go into static equilibrium with their environment. Also, corrosion is not consistent. Slightly different alloys, thicknesses, mechanical stresses, impurities, and differences in manufacturing techniques can all drastically affect corrosion rates. In one case, during an excavation in Tel Abu Hawam, Israel, a pair of bronze cymbals was found on the ocean floor. While one was almost entirely corroded away the other was in very good condition (Fox, 1994). All and all, this means that we should expect to see a wide range of corrosion rates for each material and any approximations we make about corrosion should take this into consideration.

3. A Corrosion Model

3.1. Purpose

The purpose of this model is merely to demonstrate that it is reasonably likely enough for us to detect corroding materials on shipwrecks. It is also useful in determining if there are certain materials more worth pursuing than others. Therefore, this model assumes somewhat ideal conditions for corrosion and dispersion into seawater.

3.2. Assumptions and Method

The model used is a simple box model. It assumes a 1000 lb spherical source. Also, it assumes that as particles are corroded away from the source they enter a one meter cubed box. The particles are equally distributed within this box such as in a well-mixed benthic boundary layer (Hanson and Donaghay, 1998). The flux of seawater through the box, which is the driving force for the movement of particles in this model, is 0.001 m^3/s, which indicates that the water surrounding the archaeological site is relatively stagnant such as in a basin. It is assumed that the materials corrode uniformly at the given corrosion rates and that these rates stay the same over time. Figure 1 (a-f) includes the data that was derived from running this model with silver, copper, lead, iron, and tin. Each includes a graph of the material's weight over time and a graph of the concentration of the material within the one meter cubed box. The corrosion rates used are indicated at the top of the graphs. In Figure 1 (a-e), the rates are taken from Boyd and Fink (1978) and generally based upon averages from a sixteen-year study. The corrosion rate for silver is not well substantiated and should probably be lower. In Figure 1(f), the corrosion rate is taken from a conjecture made by Cemal Pulak (1999) based on analysis of copper ingots from the Uluburun Shipwreck. In each case the average seawater background concentration of the metal is plotted in red and assumed constant over time (Pilson, 1998). Moreover, an approximate detection threshold of 0.1nmol/kg is plotted in green. A calculation was also performed to ensure that the concentrations of trace metals due benthic flux are many orders of magnitude less than the concentrations of trace metals due to corrosion as taken from this model (Riley and Chester, 1976).

It is important to remember that there are many other things that affect trace metal concentrations in seawater including dispersion, speciation, and complexation. In this model we have neglected both the hydrodynamics of particle dispersion and chemical interactions in order to drastically simplify our calculations and give us a more general picture of the best-case scenario. A more precise model of this situation could be created in the future in order to analyze many more of the factors that affect the concentrations of trace metals in seawater. For instance, Applied Science Associates works on the

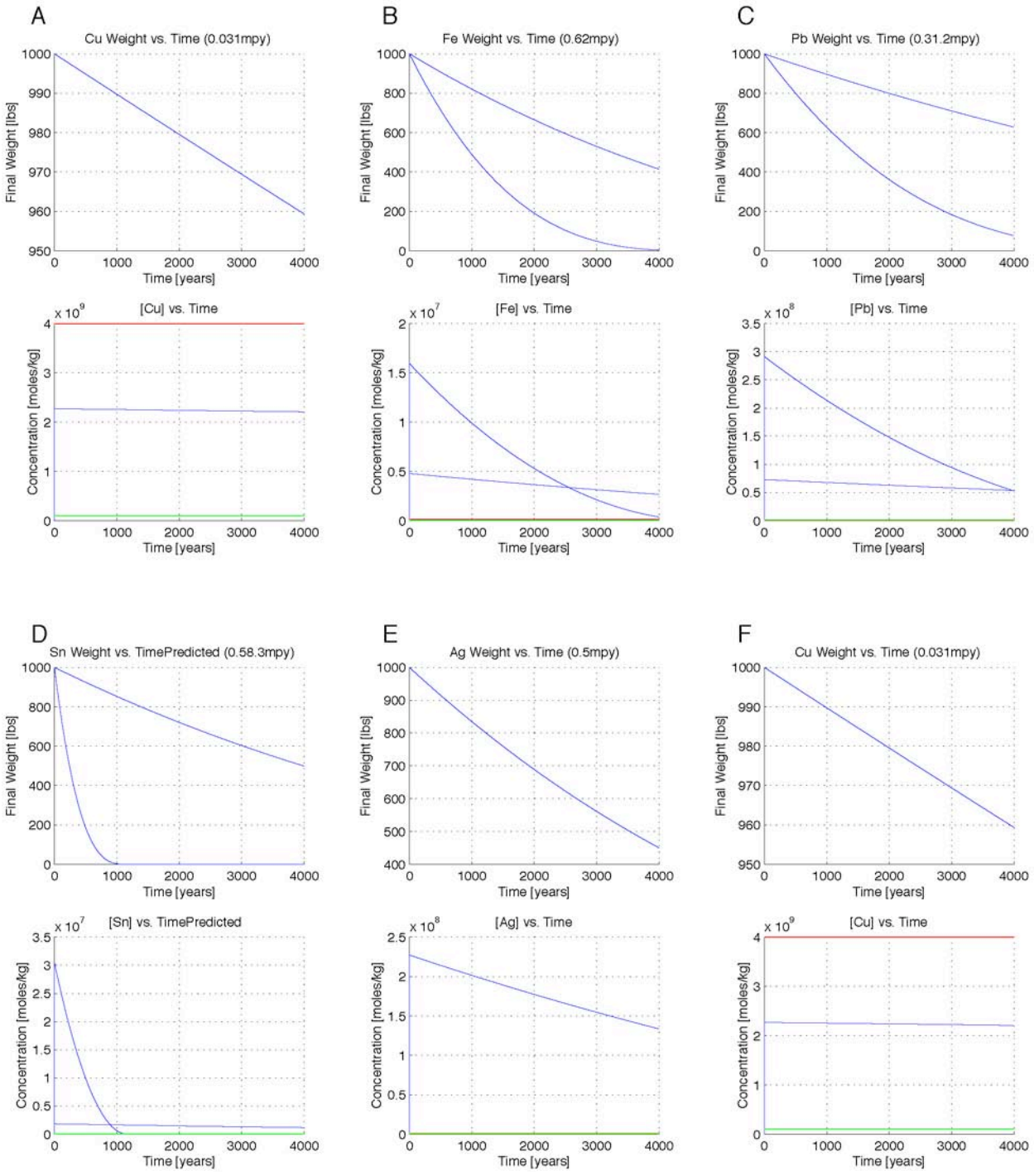

Figure 1 (a-f). In each case, in the top graphs, the blue line depicts the weight of the metal over time due to corrosion. In the bottom graphs, the blue line depicts the concentration of the metal in seawater over time due to corrosion. The red line indicates the average background concentration of the metal in seawater (Pilson, 1998). The green line indicates the assumed detection threshold of 0.1 nmol/kg. The corrosion rates (in mils per year where 1 mil is 0.001 of an inch) used in Figure 1 (a-e) are indicated in the heading of each graph and are taken from Corrosion of Metals in Marine Environments (Boyd and Fink, 1978). The corrosion rate used in Figure 1 (f) is indicated in the heading of that graph and is based on conjectures made by Cemal Pulak (Pulak, 1999). The scales are not the same between the graphs. Not all lines indicating the detection limit and the background concentrations can be easily seen because in some cases, due to the scale of the graph, they essentially coincide with the x-axis. Also, important to note is that the value given for silver is not firmly established and it likely that that value should be much lower.

problem of determining where a chemical may be coming from in the marine environment based on the specific hydrodynamics of that area. Performing such calculations in reverse may be helpful in better understanding our problem.

3.3. Results of the Model

3.3.1. Analyzing the Graphs. As we can see from the data produced in Figures 1 (a-e) we can expect to see much higher concentrations of each metal due to corrosion than both the background concentration and the detection threshold, at least initially. In all cases, because of the decreasing size of the object due to corrosion, concentrations taper out over time. Therefore, for more than 4,000 years we might expect to find high enough concentrations of these metals in seawater for us to detect. Of course, due to the assumptions in our model, this is an upper bound. In Figure 1 (f) we can see that the concentration of copper due to corrosion is less than the background concentration. This is because the corrosion rate derived from assumptions made by Cemal Pulak (1999) is much lower than published corrosion rates given by Boyd and Fink (1978). Therefore, either Pulak's assumptions are wrong or the corrosion rate of these copper ingots was not constant. Based on literature about corrosion it is likely that the latter is the case. The corrosion rate of these ingots probably diminished drastically over the 3,300 years that they have been submerged. This would mean that the copper concentration in the seawater at present would be much lower than our model has predicted. Another possibility is that the environment that the ingots were found in is not conducive to corrosion and therefore these ingots have actually corroded at this very low rate for the entire time they have been submerged. Unfortunately, no chemical study as been performed on the site to determine if the ingots are still leaching corrosion products into the seawater. However, if this model does in fact illustrate the corrosion rate and subsequent concentrations of copper in the seawater surrounding the Uluburun shipwreck and if our sensor was accurate to 0.1nmol/kg we could potentially sense these copper ingots. Not only is there more than 1,000 pounds of copper on the seafloor in this location, but also our sensor would detect the concentration of copper due to corrosion added to the background concentration, which, in turn would be perceptibly higher than just the background concentration because these two values are of the same order of magnitude. Therefore, due to this model we can see that it may be possible to detect all of these corroding materials in seawater under somewhat ideal environmental conditions if there was enough of the material present on the seafloor.

3.3.2. The Best Environment. Through analysis of this model we can determine the ideal environment for operation of a sensor. This environment will allow for average corrosion rates meaning that oxygen level, depth, pH, sediment composition, and temperature will all be moderate. Low background concentrations of the trace metals that we are looking for are desirable. Moreover, the best environment would also have relatively stagnant water and exhibit a strong well-mixed benthic boundary layer. Anoxic waters would probably not be ideal for this sensor because metal corrosion is variable in such environments because of their high concentrations of hydrogen sulfide.

4. Sensor Design

4.1. A Final Choice of Materials to Detect

Despite the fact that there is good reason to design a sensor to be able to detect iron, copper, lead, tin, and silver, for this particular project we have decided to narrow this list down to metals that are detectable using current technology. Not only must we choose metals for which there is an easy method of detection in seawater, but this method must be adaptable for in situ operation. Moreover, this same method must have a low enough detection threshold for our application. Currently few methods exist which can accurately and easily detect silver and tin concentrations in seawater. Moreover, though methods for the detection of lead in water do exist they are mostly for freshwater and not exceptionally sensitive. Methods do exist for copper and iron, as these metals are important to detect in seawater because of iron's biological importance and copper's environmental importance. Table 1 summarizes each of the factors taken into account in order to narrow down the number of metals our sensor will detect, specifically corrosion, seafloor residency, archaeological likelihood of discovery, and current technology. Based on all of these factors we have chosen to design a copper and iron sensor. A sensor to detect lead would also be particularly useful in the future.

Table 1. A Comparison of Several Different Archaeologically Important Metals

	Corrosion Potential (Concentration of Metal)	Residency on Seafloor	Archaeological Likelihood of Discovery (in Large Quantities)	Reliable Seawater Detection Method That Could be Used for In Situ Measurements
Gold	None	Long	Low	No
Silver	Low	Long	Low	No
Copper	Medium	Medium	Medium	Yes
Lead	Medium	Medium	High	No
Tin	High	Short	Low	No
Iron	High	Short	High	Yes

4.2. Method of Detection

In designing an in situ underwater copper and iron sensor we have explored several possible detection methods. Importantly, in order for this sensor to be appropriate to this application it needs to be simple and accurate. It must have very good time resolution and therefore must not preconcentrate the sample or analyze it in batches. Rather a continuous flow-through method is ideal. The many methods for detection of trace metals in seawater include chemiluminescence, fluorescence, spectophotometry, and electrochemical methods (Buffle and Horvai, 2000). In order to ensure appropriate time resolution we have decided against electrochemical methods. Moreover, without preconcentration both spectophotometry and fluorescence do not produce the accuracy we need. Fortunately, chemiluminescence has both very good accuracy and resolution. The only downside to this method is that in order to analyze some metals a large number of different reagents would be required. Fortunately, for both copper, and iron, the number of reagent required is relatively small. The bench top chemiluminescent method for copper established by O'Sullivan et al (1995) and the bench top method for iron established by Sunda and Hunstman (1991) produce both the resolution and accuracy that we need for this application and importantly are easy to implement in situ. These methods and a description of how we plan to convert them from bench top methods to in situ methods will be described in Section 4.4 of this paper.

4.3. Design Parameters

A copper and iron sensor used for underwater archeological searching could be designed for integration into a variety of different vehicles and instruments, such as AUVs and Remotely Operated Vehicles (ROVs), and used in conjunction with a multitude of other sensors, such as sonar systems and sub-bottom profilers. We have decided to integrate our sensor into an AUV because in the future engineers hope to use them to do archaeological sonar searches more efficiently (Mindell and Bingham, 2001). Therefore, we have chosen to design our sensor so that it will operate on REMUS, Remote Environmental Monitoring UnitS, a small AUV created by the Wood's Hole Oceanographic Institution equipped with a side-scan sonar system. The benefit of using this AUV is that its nose and hull can detach, so that an extra hull section containing a sensor can be inserted. This sensor can rely on the power provided by REMUS and can also transmit and accept data from the AUV. REMUS is only 52 inches long and 7.5 inches in diameter and therefore we are limited in the size of our sensor. We have decided to fit our sensor into a six-inch hull section. It will have the same diameter as the REMUS.

4.4. Mechanical, Electrical, and Fluidics Design

Using SolidWorks, a three dimensional CAD program, we have created a detailed design of our copper and iron sensor. We have also created several block diagrams in Adobe Illustrator. Based on the two chemiluminescent methods chosen a flow-through copper and iron detection scheme was developed. Figure 2 shows the flow design that will be replicated for each metal. For copper, reagent 1 is 5% H_2O_2 in addition to an acid in order to lower the pH of the solution to 3 to free copper from organic ligands. Reagent 2 is CEDAB, 1,10 phenanthroline, TEPA , and sodium hydroxide. The detection limit for this method is 0.06 nmol/kg (Sunda and Huntsman, 1991). For iron, reagent 1 is an optional solution to reduce Fe (III) into Fe (II) in order to acquire a total iron amount if desired. Reagent 2 is luminol, potassium hydroxide, and boric acid. The desired pH for this reaction is 9.9 and the detection limit is 0.05 nmol/kg (O'Sullivan et al, 1995). In each case a calibration solution allows the device to be calibrated in situ as often as desired.

Similar to Figure 2, Figure 3 is a plumbing diagram that takes into consideration the actual parts needed for this system. The photomultiplier tubes (PMT) chosen are from Hamamatsu's HC120 Series. They are able to measure the intensity of light produced in a chemical reaction, and this intensity corresponds to the concentration of the metal in the seawater. The pumps are Bio-Chem Valve Inc. Series 090SP micro-pumps. The flow-through cell can be obtained through Hellma Worldwide. The junctions, coils, and tubing can be purchased from Upchurch Scientific.

Next an electronics scheme was created which shows the power and data transfer between the individual parts (Figure 4). As you can see that while the sensor gets its power from the REMUS and can communicate with REMUS, it stores its data on a Persistor CF2 microcontroller. This microcontroller also controls the action of the pumps and PMTs. The actual circuit board, which will serve as a power converter, not yet been designed.

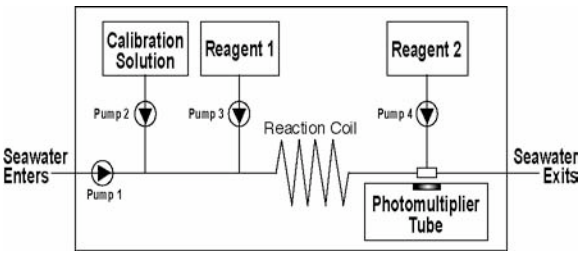

Figure 2. This block diagram depicts the general flow design of the sensor. The seawater enters the device and can be mixed with a calibration solution if calibration is deemed necessary. It then mixes with the first reagent and a reaction can take place in a reaction coil. The second reagent is added and this reaction produces light that the PMT measures. The seawater exits.

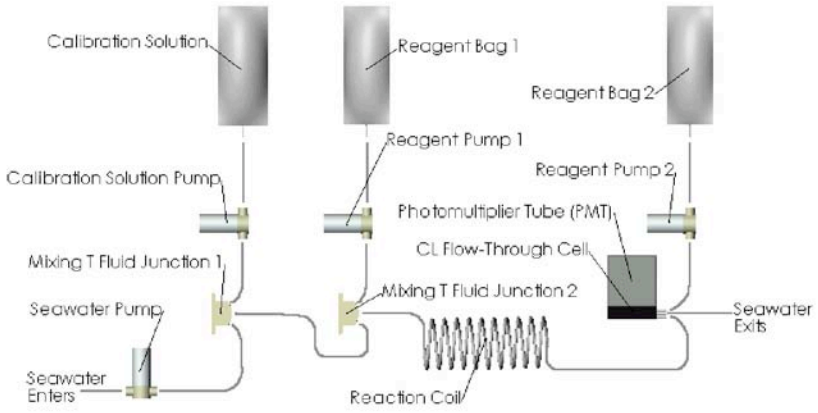

Figure 3. This SolidWorks plumbing diagram is similar to Figure 2 , but shows the actual part from which the sensor will be created.

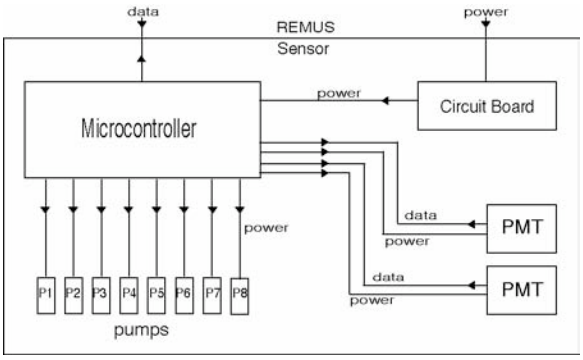

Figure 4. This block diagram depicts the general electronics design of the sensor. The power is received from the REMUS. The sensor and the REMUS can transmit data to each other. The power is regulated through the circuit board and then sent to a microcontroller. The microcontroller sends power to the pumps and PMTs and the PMTs, in turn, send data back to the microcontroller. Information gathered is stored on the microcontroller.

The whole system was assembled in order to fit into a six-inch REMUS hull section (Figure 5). The top half of this system, which holds the electronics and fluidics, is dry and the bottom half, which holds the reagent bags, is flooded so that the reagents will be at the same pressure as the seawater. The six-inch REMUS hull section as adapted for this sensor is shown in Figure 6.

4.5. Design Limitations

Limitations on this device include a depth limit dependant upon the fluidics and electronics. Also, in order to detect chemical plumes due to corroding materials on shipwrecks the sensor will have to travel fairly closely along the seafloor. Proximity to the seafloor may be limited by the side-scan sonar on the REMUS.

4.6. Other Design Options

The design above is just one path that we could take in building such a sensor. In the future micro-electrical mechanical (MEMs) devices could be used in fluidics systems in order to decrease the overall size of the sensor (Figure 9). For this project we have researched the possibility of designing our device using MEMs technology; however, it seems as though at the current time this would be an especially tricky task. This is because of the troubles with purging bubbles from MEMs systems, pumps, and valves (Buffle and Horvai, 2000).

5. Discussion

5.1. Benefits of this Research

The development of an iron and copper sensor to be used in underwater archaeology would be an important advancement in the field and help make searching for underwater archaeological sites more time-efficient and cost-effective. This technology would allow us to gather chemical data in addition to sonar data in the sea without intrusion into the sediment. This is especially important on archaeological sites where disturbing the

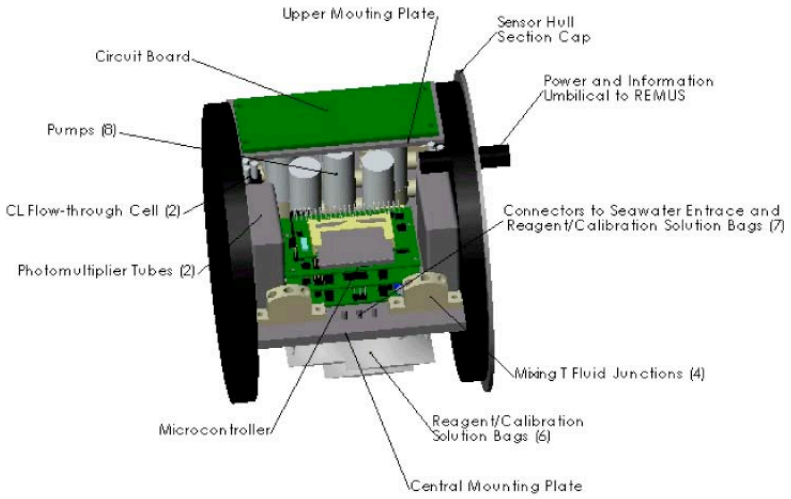

Figure 5. This SolidWorks diagram depicts the sensor and all of its components, both electric and fluidic, as it might fit into a six-inch REMUS hull section. The top half of this sensor contains the electronics and fluidics and is dry. The bottom half contains the reagent bags and is flooded.

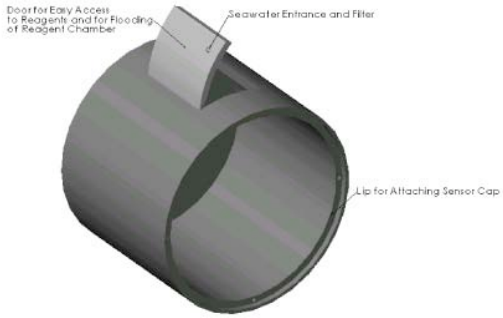

Figure 6. This SolidWorks diagram depicts the sensor housing, a six-inch REMUS hull section. This hull section is equipped with a door for access to the reagent bags and a filter for the intake of samples.

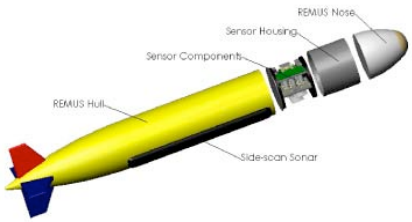

Figure 7. This SolidWorks diagram depicts the REMUS and the iron and copper sensor as they would fit together.

Figure 8. This SolidWorks diagram depicts the assembled REMUS.

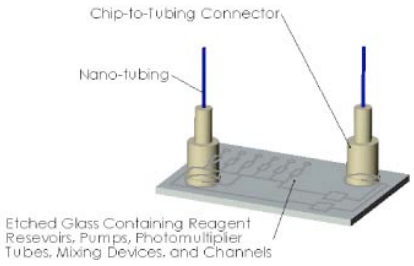

Figure 9. This SolidWorks diagram depicts a lab-on-a-chip, a fluidics MEMs device. In the future the sensor proposed in this paper could be created using MEMs technology and significantly smaller than the proposed design.

sediment could lead to the loss of archaeological information. Beyond searching for archaeological sites, such a device could also be used to chemically analyze previously found archaeological sites or even search around sites to look forhidden artifacts. Therefore, a copper and iron sensor has several archaeological applications.

5.2. Where to go From Here

The next steps in this project include performing a bench top experiment of the proposed sensor in order to determine if, as designed, it has the accuracy and time resolution needed. Then, it will be necessary to order the parts for the in situ sensor and build it. After this we will integrate this sensor into REMUS and field-test it. Finally, it should be tested on known underwater archaeological sites and then to look for new ones.

5.3. Other Benefits of a Copper and Iron Sensor

This research also benefits other marine-related fields. For instance, an underwater chemical sensor could be used for environmental purposes. Since copper is hazardous to life, a copper sensor would be useful in detecting the sources of copper pollution in the sea. There are also industrial benefits to building a chemical sensor. For instance, it could be used to search for and inspect underwater piping, oil platforms, and other underwater structures. Lastly, it could be used for military purposes such as the detection of mines and submarines, and the inspection of underwater military structures.

6 Conclusions

In conclusion this paper has included an analysis of the usefulness of underwater chemical sensors in underwater archaeology. An underwater chemical sensor used on an AUV equipped with side-scan sonar should be able to provide scientists with important information about the potential location of archaeological sites in the sea. This should be a cost effective and efficient way to conduct an underwater archaeological survey.

References

Boyd, W. K. and F. W. Fink. Corrosion of Metals in Marine Environments. Metals and Ceramics Information Center, Columbus, OH, 1978.

Brown, Richard. *Corrosion and Corrosion Control: Class Notes*. University of Rhode Island, Chemical Engineering, Course 534, 2002.

Buffle J. and G. Horvai. In situ Monitoring of Aquatic Systems: Chemical Analysis and Speciation. John Wiley & Sons, LTD, Chichester, 2000.

Fox, G. L. *Cupreous Metal Corrosion at a Bronze Age Coastal Marine Archaeological Site: A Study of Site Processes at Tel Nami, Israel*. The International Journal of Nautical Archaeology. V23n1, p41-47, 1994.

Hamilton, D. L. *Methods of Conserving Underwater Archaeological Material Culture*. Conservation Files: ANTH 605, Conservation of Cultural Resources I. Nautical Archaeology Program, Texas A&M University, WWW: http://nautarch.tamu.edu/class/ANTH605, 1998.

Hanson, A. K. and P. L. Donaghay. Mirco- to Fine- Scale Chemical Gradients and Layers in Stratified Coastal Waters. Oceanography. V11n1, p10-17, 1998.

Mindell, D.A. and B. Bingham, *New Archaeological Uses of Autonomous Undersea Vehicles*. IEEE "Oceans" Engineering Conference, 2001.

O'Sullivan, D. et al. *Stopped Flow Luminol Chemiluminescence Determination of Fe(II) and Reducible Iron in Seawater at Subnanomolar Levels*. Marine Chemistry, V49, p65-77, 1995.

Pedersen, R. K. *Bronze Age Shipwreck Excavation at Cape Gelidonya*. Institute of Nautical Archaeology. WWW: http://ina.tamu.edu/capegelidonya.htm, 2002a.

Pedersen, R. K. *Bronze Age Shipwreck Excavation at Uluburun*. Institute of Nautical Archaeology. WWW: http://ina.tamu.edu/ub_main.htm, 2002b.

Pilson, M. E. Q. An Introduction to the Chemistry of the Sea. Prentice Hall, Upper Saddle River, NJ, 1998.

Pulak, C. *Shipwreck! Recovering 3,000 Year Old Cargo.* Archaeological Odyssey. Sept/Oct 1999.

Riley, J. P. and R. Chester, eds. Chemical Oceanography: 2nd Edition, Volume 6. Academic Press, London, 1976.

Sunda, W. G. and S. A. Huntsman. *The Use of Chemiluminescence and Ligand Competition with EDTA to Measure Copper Concentration and Speciation in Seawater.* Marine Chemistry, V36, p137-163, 1991.

Aknowledgements. A special thanks to Ian MacLeod and Vicki Richards at the Western Australia Maritime Museum; Brendan Foley, Richard Camilli, and Dave Mindell at MIT; and Donny Hamilton at Texas A&M for their helpful correspondence. Also, thanks to SubChem Systems Inc. including Al Hanson, Jeff Barnes, Billy DeLeo, Pete Egli, Richard Sweetman, Heather Saffert and Peter Obuchowski. And finally thanks to Rob Pockalny, Dwight Coleman, Sarah Weinstein, and Art Spivak at URI. This Research Experience for Undergraduates was funded through a National Science Foundation Grant.

J. L. Mathieu and A. K. Hanson, Graduate School of Oceanography, University of Rhode Island, Narragansett, RI 02882. (jmathieu@mit.edu, akhanson@gso.uri.edu)

Pulse-to-Pulse Coherent Doppler Measurements of Near Surface Turbulence

B. Patrick Sullivan[1], and Tetsu Hara

Graduate School of Oceanography, University of Rhode Island, Narragansett, Rhode Island

Abstract. This paper presents field-testing of a pulse-to-pulse coherent acoustic Doppler profiler for the measurement of near-surface oceanic turbulence. It has yet to be determined to what degree turbulence in the near surface layer can be enhanced by wave breaking and/or wave-current interactions, causing the turbulent dissipation rates to be higher than those predicted by analogy to wall-layer behavior. Instrumentation consisted of three pulse-to pulse coherent acoustic Doppler profilers mounted in orthogonal directions. Data from the three profilers were used to estimate the turbulent dissipation rates. The results were then compared with simultaneous measurements from a sounder, and a CTD profiler. Data were collected in the surface wave zone under a variety of conditions. Both stratified and well-mixed conditions were observed, and some interesting questions were raised concerning the possibility of anisotropy in the turbulence of the near-surface layer. This study demonstrates the capability of a pulse-to-pulse coherent acoustic Doppler velocimeter to measure the dissipation rate and other relevant turbulence parameters in the near-surface layer.

1. Introduction

The near surface layer, or surface-wave zone, is that uppermost layer of the ocean, which is directly affected by surface forcing phenomena such as breaking waves, heat flux, and wind shear. Although the near surface layer plays a central role in atmosphere-ocean interaction, a detailed and accurate understanding of the physics governing this layer has continued to elude us. For example, no consensus has been reached concerning the relationship between the turbulent dissipation rate, ε, and depth (Drennan et al. 1996). The classical wall-layer theory predicts $\varepsilon \propto z^{-1}$, where z is the depth from the surface, whereas recent studies have shown $\varepsilon \propto z^{-2}$ to $\varepsilon \propto z^{-4}$ (Gargett 1989; Drennan et al. 1992), and even $\varepsilon \propto e^{-z}$ (Anis and Moum 1995).

As a result of such discrepancies, turbulence in the surface-wave zone has been explored extensively in the last several years. Whereas in the past, the classical "law-of-the-wall" description of the surface layer had been considered accurate, observational studies in recent years have brought to light that wave breaking (Thorpe 1993; Melville 1994; Anis and Moum 1995), and other surface processes such as Langmuir circulations (Skyllingstad and Denbo 1995; McWilliams et al. 1997; Melville et al. 1998) may produce enhanced turbulence and mixing, causing higher than expected dissipation rates in the surface-wave zone (Agrawal et al. 1992; Craig and Banner 1994; Terray et al. 1996; Veron and Melville 1999).

One encounters several major obstacles when seeking an understanding of the processes that take place in the surface-wave zone. Paramount among these obstacles is the scarcity of reliable and accurate measurements. Measurements of turbulence in the near surface layer are complicated by the difficulty in securing a stable platform from which to make the desired observations, the relatively small thickness of the layer itself, and the intermittency of relevant surface forcing events such as wave breaking. Most previous turbulence measurements were performed using instruments that yield time series of velocity at a singe point, whether deployed from a moving profiler or from a stationary platform. One typically then encounters the complicated (if not impossible) task of transforming from a temporal signal to a spatial one through some variation of Taylor's hypothesis (Veron and Melville 1999) in order to estimate the turbulent dissipation rate. Further complicating measurement in the surface zone is the fact that turbulent velocity fluctuations are typically two to three orders of magnitude less energetic than background wave motions (Trowbridge and Elgar 2001). The low energy level of these fluctuations can complicate the analysis, in which motion from turbulent fluctuations must be separated from motion due to the mean flow.

The following observational study was performed to determine the suitability of a pulse-to pulse coherent Doppler profiler in analyzing the turbulence structures and dissipation rates in an estuarine environment. The advantage of this instrument is that it yields instantaneous spatial velocity measurements, which may be used to estimate the turbulent dissipation rate without relying on Taylor's hypothesis. This paper describes the field-testing of that instrument in the Victoria Sound, British Columbia.

2. Instrumentation

Coherent Doppler sonar is distinguished form the standard incoherent variety of Doppler sonar in that rather than sending out a single pulse and determining velocity from a frequency shift in the backscatter, it transmits a packet of two or more identical, equally spaced pulses, and the velocity is then determined by comparing the separation between pulses in the backscatter with the separation between pulses in the original pulse packet. Coherent Doppler has better

[1] Now at Westminster College in New Wilmington, PA.

sensitivity to weakly scattered sound than the traditional incoherent type of sonar.

Three pulse-to-pulse coherent Doppler instruments (Dopbeam, Sontek, San Diego) were mounted orthogonally on a metal frame, as pictured in Figure 1. Each Dopbeam unit is 40 cm long and 6 cm in diameter, with a 2.5 cm circular transducer in the center of one end. Dopbeam simultaneously measures velocity at 119 points in space along the direction of the beam. Those 119 points are spaced .006 m apart. The Fresnel zone boundary is located 0.18 m from the transducer. So the Dopbeam is measures velocity over a distance of 119 x .006 = .714 m starting from .18 m in front of the transducer. The sampling rate is 20 Hz for all three Dopbeams.

The frame assembly, which carried the Dopbeams, also carried a centrally mounted CTD sensor. So, salinity, temperature, and depth information, as well as three-dimensional velocity profiles could be obtained simultaneously for a particular location. The frame was lowered slowly with a winch from a crane arm structure, which was mounted on a Zodiac (see Figure 2). Also mounted on the Zodiac, a sounding instrument provided a backscatter image, which showed bubbles, as well as an image of the instrumentation, and sea floor when they were in range.

Figure 1: The three Dopbeams and a CTD unit mounted on the cage for deployment.

3. Field Measurements

Measurements were taken on two different days to obtain information about turbulence under different wind and wave conditions. The first day (June 25, 2002) was relatively calm, with almost no wind. As a result, the water remained rather stratified, and exhibited a noticeable temperature gradient with depth. The second day (June 26, 2002) was windy with white caps and small breakers. Because of the wind forcing, and wave breaking, the surface-wave zone was very well mixed, exhibiting strikingly little variation in temperature or salinity with depth.

On the first day, the Dopbeams were lowered slowly, a meter at a time, from one to eight meters deep. The instruments were held at each depth for approximately two minutes. On the second day, the instruments were lowered continuously from one to eight meters and returned to the surface, before lowering again. Each continuous lowering took place over approximately eight minutes, for an average continuous lowering speed of approximately $.016 ms^{-1}$. These different techniques employed in lowering the instruments can clearly be seen and compared in the pressure plots of Figures 3-5.

4. Analysis

Dopbeam signals consisted of a 20 Hz time series for each of the 119 spatial points. Each record was approximately eight minutes long, or about 9,600 records. Data from the first day was separated into two minute time periods for which the instrument assembly

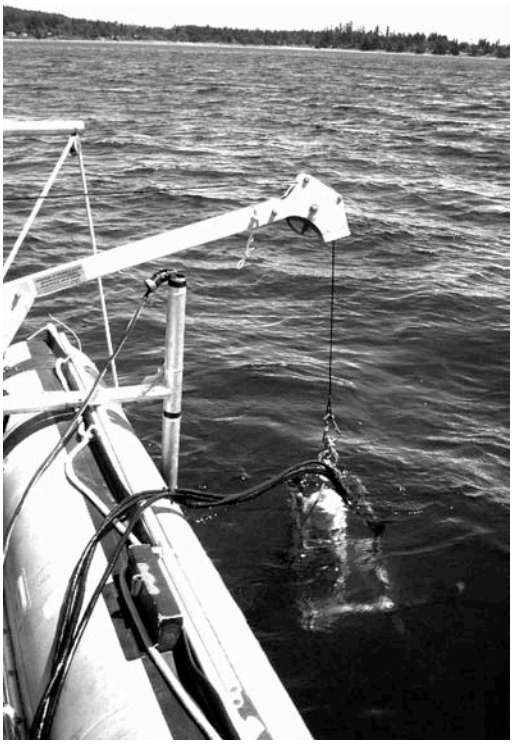

Figure 2: The instrument cage being lowered from a crane, which was mounted on the Zodiac.

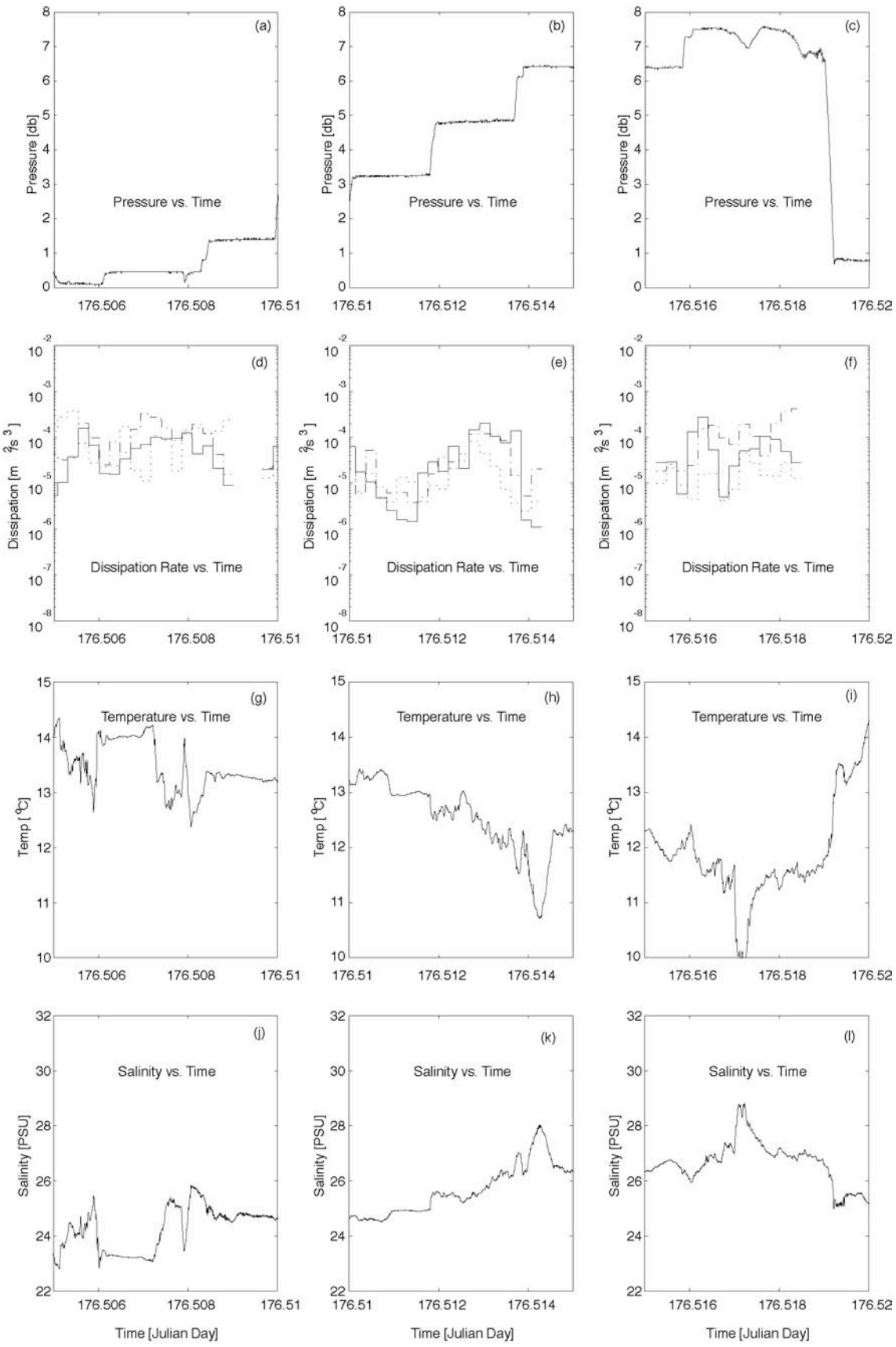

Figure 3. Various parameters measured with DOPBEAM during a lowering with three depth-maintained stations

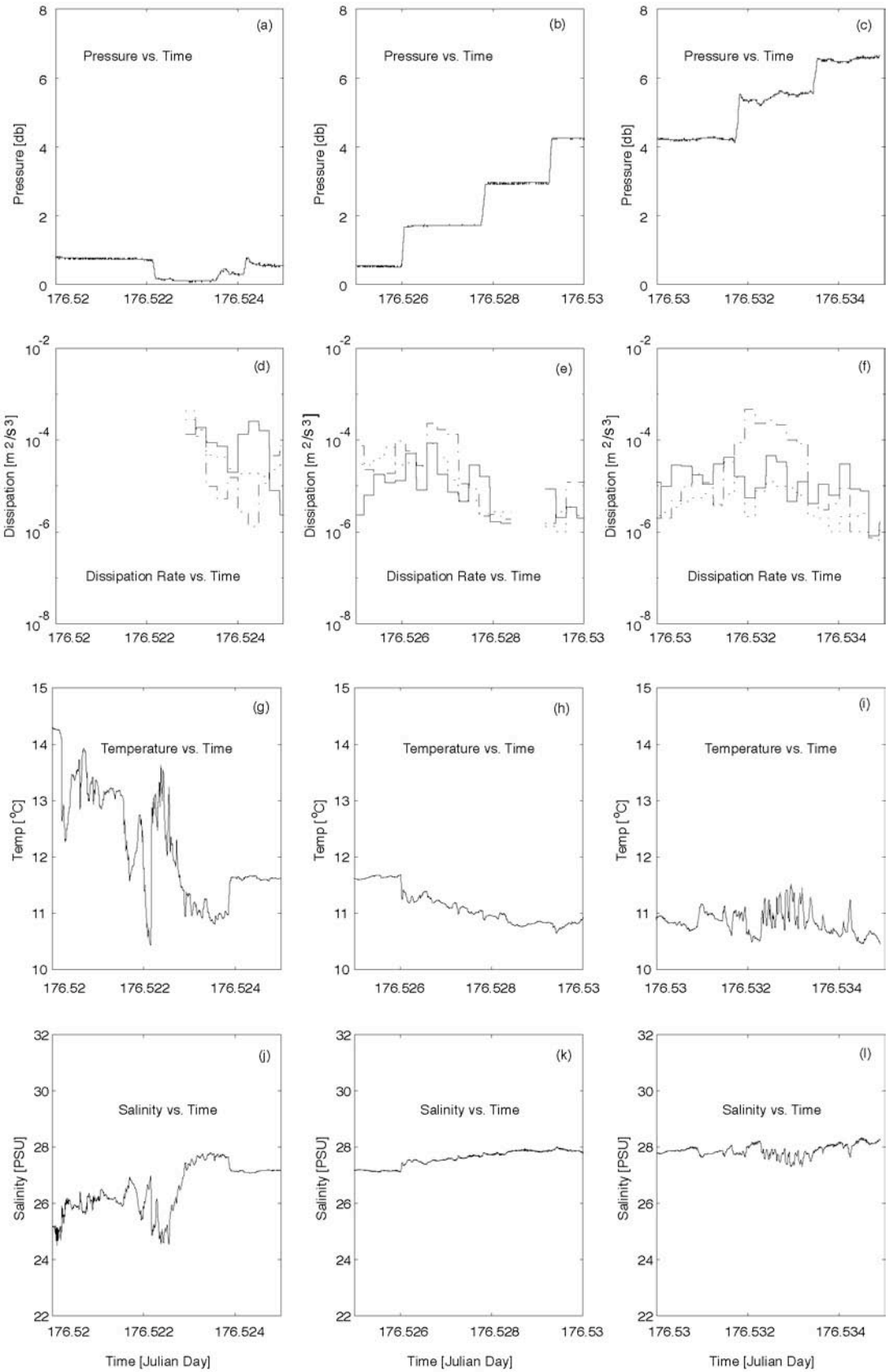

Figure 4. Various parameters measured with DOPBEAM during a lowering with four depth-maintained stations

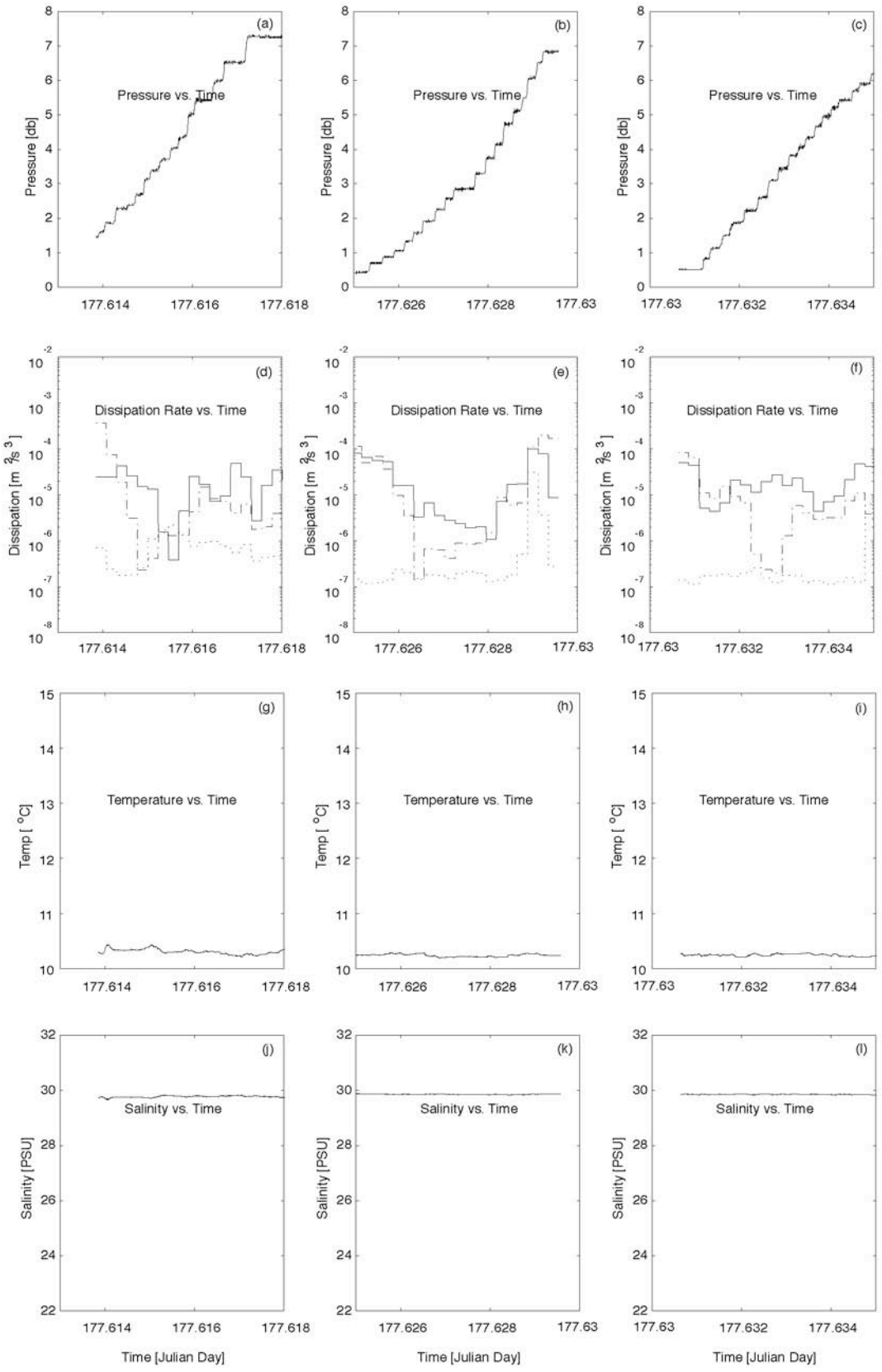

Figure 5. Various parameters measured with DOPBEAM during a lowering with twenty depth-maintained stations

remained a fixed depth. Each of these fixed depth records were analyzed separately. On the second day, because the instruments were continuously dropped at a relatively slow vertical velocity, data from that day were not binned into sections of equal depth. Rather, dissipation was simply averaged over every 25.6 seconds for the duration of each continuous sounding.

Because the Dopbeam was able to collect precise velocity information at a relatively high sampling rate, and at densely spaced locations simultaneously, (i.e. data points are densely spaced in both space and time), both frequency and wave number spectra can be directly determined from the signal. Ensemble averages of frequency and wavenumber spectra were made over every 512 records at a time, i.e. 25.6 seconds worth of 20 Hz data.

Veron and Melville (1999) have used some common statistical tools (Tennekes and Lumley 1972) to analyze turbulence signals obtained with a Dopbeam. This study makes use of the same tools.

We will use the one-dimensional wavenumber spectrum defined as,

$$\Phi(k,t) = \frac{1}{2\pi}\int_{-\infty}^{\infty} R(r,t)e^{-ikr}\,dr, \qquad (1)$$

where $R(r,t)$ is the longitudinal spatial correlation,

$$R(r,t) = \overline{u_1(x_1,t)u_1(x_1+r,t)}. \qquad (2)$$

The overbar here denotes spatial averaging, and $u_1(x_1,t)$ is the velocity component in the direction of the beam.

Also calculated, was the one-dimensional frequency spectrum defined as,

$$S(\omega,t) = \frac{1}{2\pi}\int_{-\infty}^{\infty} R(\tau,t)e^{-i\omega\tau}\,d\tau, \qquad (3)$$

where $R(\tau,t)$ is the temporal autocorrelation given by;

$$R(\tau,t) = \overline{u_1(x_1,t)u_1(x_1,t+\tau)}. \qquad (4)$$

The overbar in this case, of course, denotes time averaging, and $u_1(x_1,t)$ is again the component of velocity in the direction of the beam. Plots of the wavenumber spectra, like those seen in Figures 6 and 7, were examined for the presence of an inertial subrange. Figures 6 and 7 depict the

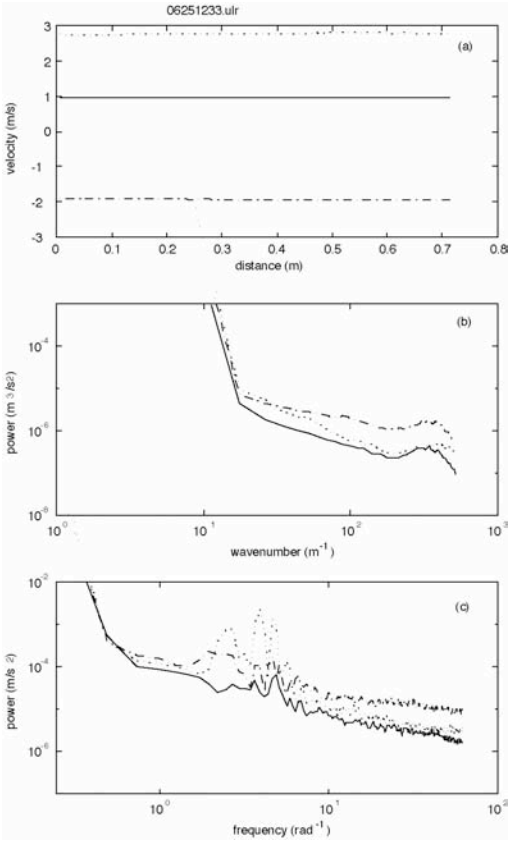

Figure 6. Wave form spectra of DOPBEAM at 12:37:20

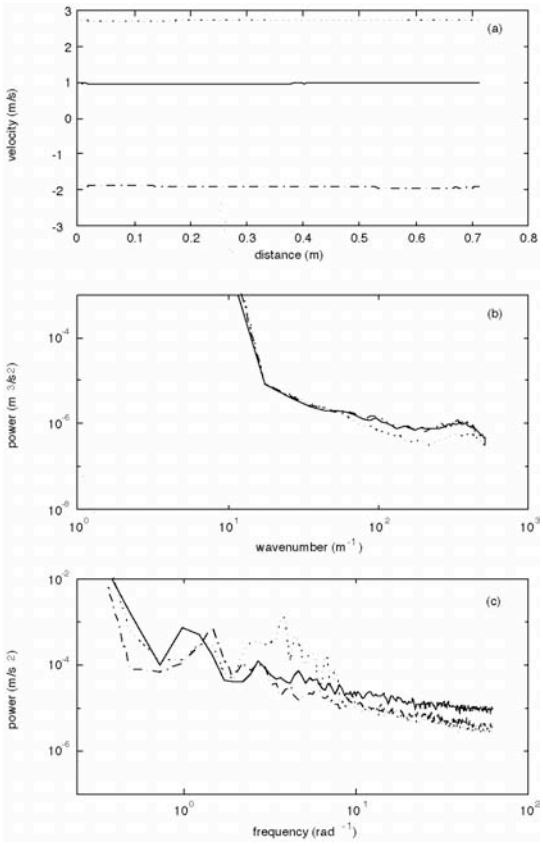

Figure 7. Wave form spectra of DOPBEAM at 12:37:40

average velocity, wavenumber spectrum, and frequency spectrum at 12:37:20 and 12:37:40, respectively.

In general, the spectra exhibited a constant, negative slope in the range of wavenumbers between approximately 26 and 132 rad/m. This area of constant slope in the spectrum is the inertial subrange theorized by Komolgorov.

For the inertial subrange, the one dimensional wavenumber spectrum assumes the form (Hinze 1975),

$$\Phi(k) = \frac{18}{55}\left(\frac{8\alpha}{9}\right)^{2/3} k^{-5/3}, \qquad (5)$$

where α is Heisenberg's constant ($\alpha \approx 0.4$ for high Reynolds number flows). Knowing this simple function, which relates wavenumber, k, to dissipation rate, ε, we can fairly easily fit a $k^{-5/3}$ curve of constant slope to the inertial subrange, and thereby determine a value for ε.

Only about half of the time was the slope of the inertial subrange reasonably close to the –5/3 predicted by Komolgorov's theory. However, in all cases which deviated from Komolgorov's prediction, the slope was less steep than expected, i.e. smaller eddies exhibited higher energies than one would expect. Although some of the wave number spectra did not have the expected slope, a "line of best fit" with the predetermined slope of –5/3 was fitted to the data points between wave numbers 26 and 132 rad/m. This least-squares type fitting simply determined the intercept, or level, of the regression line, whose slope had been forced. Equation 5 was then used to estimate the kinetic energy dissipation rates.

A time series of the dissipation rate (ε) was plotted next to data from the CTD (see Figures 3-5). The same timescale was used for all time series to facilitate comparison between CTD data and dissipation rate.

5. Results and Discussion

Results from the two days of observation were consistent in some ways, but to a large extent were strikingly different. However, those differences are not too surprising given the differing environmental conditions on the two days. On the first day, the surface-wave zone was relatively stratified, and undisturbed by the influence of wind. Temperature and salinity varied noticeably with depth. Temperature dropped from 14 °C near the surface to 10 °C at depth of almost eight meters.

Measurements on the first day were taken not far from the edge of a narrow channel between two islands. Because of the tidal forcing, a strong current existed in the channel, which emptied into the sound and caused strong turbulent mixing. Furthermore, the temperature and salinity of the water in the channel were different from those in the sound. As a result, there was a noticeable vertical temperature and salinity gradient.

Salinity increased from around 24 PSU at the surface to between 26 and 28 PSU at a depth of eight meters. Conditions being as they were, most turbulence measured on the first day was the result of internal mixing.

Based on observations by Agrawal et al. (1992) and modeling by Melville (1994), Veron and Melville (1999) have estimated some conservative bounds for the maximum and minimum dissipation rates for the upper ten meters of the ocean. According to these observations, dissipation rate (ε) in the surface-wave zone ranges from 9 x 10^{-7} m^2s^{-3} to 10^{-3} m^2s^{-3}. These dissipation rate estimates correspond to an inertial sub-range on the order of .01 m to 1 m (Veron and Melville 1999). Kinetic energy dissipation rates on the first day ranged from to 9 x 10^{-7} m^2s^{-3} to 3 x 10^{-4} m^2s^{-3}. These dissipation rates are certainly within the range predicted by Veron and Melville. A plot of the time series of ε values from the first day can be seen in subplots **d**, **e**, and **f** of Figures 3-5. Comparing these figures to subplots **a**, **b**, and **c** of Figures 3-5, it is clear that there does not appear to be any significant trend toward lower dissipation rates at greater depths. Also, dissipation rates seem to be within a similar range for each of the three Dopbeams; the turbulence appears to be basically isotropic.

In contrast, the second day exhibited winds in the range of 5-6m/s, and small breakers were observed. As a result of surface forcing, the surface-wave zone was relatively well mixed compared to the first day. As opposed to the 4 °C temperature drop observed in the first 7.5 meters on the first day, the second day exhibited almost no temperature gradient at all. Temperature remained around 10.3 °C for all depths observed, never varying more than 0.2 °C. Salinity, at around 29.9 PSU, also remained basically constant for all observed depths (see Figure 5).

For the two horizontal Dopbeams, Dissipation rates are again in agreement with the estimates of Veron and Melville (1999), varying between 2 x 10^{-4} m^2s^{-3} and 2 x 10^{-7} m^2s^{-3}. Dissipation seems to be noticeably enhanced in the first half meter of depth, typically in the neighborhood of 10^{-4} m^2s^{-3}, although below that depth ε does not appear to consistently decrease as depth increases.

By far the most striking feature of the second day's data is the difference between vertical and horizontal ε values. Dissipation rates calculated from the vertically mounted Dopbeam generally hovered around 10^{-7} m^2s^{-3}, with only two notable exceptions: there was a dramatic increase in ε near the bottom of the second and third soundings on the second day (see Figure 5 **e**,**f**). But in general, vertical dissipation was between one and three orders of magnitude lower than the horizontal dissipation for all measured depths.

The strong anisotropy on the second day may be a product of instrument malfunction. The reliability of data from each Dopbeam may be verified by referring to the correlation coefficient associated with each velocity measurement. This coefficient represents the correlation between two successive, coherent pings, and as such is a measure of the quality of the velocity estimate based on that pair of pings. The correlation

coefficient assumes values between zero and one, and is given by (Veron and Melville 1999),

$$C = \frac{|X(\Box)|}{|S(t)||S(t+\Box)|}, \qquad (6)$$

where S(t) is the complex received signal, X(□) the complex signal autocorrelation, and the vertical bars signify that the modulus of the value is kept.

On the first day, the mean values of the correlation coefficients for the two horizontal Dopbeams are C_1 = 0.6731 and C_2 = 0.6450 while the mean value of the correlation coefficient for the vertical Dopbeam was C_3 = 0.8228. These mean values represent averages over the entire period of data collection for the first day. Similarly, the correlation coefficients for the three instruments for the second day are C_1 = 0.5715, C_2 = 0.6434, and C_3 = 0.8227. Figures 8 and 9 show time series of the correlation coefficients for the three Dopbeams for 500 seconds of data from each day.

Although the average value of the correlation coefficient for the vertical instrument in noticeably higher on both days, the strong anisotropy only appears to be present in the second day's data (refer to Figure 5). So, it appears that the apparent anisotropy is real, or at least that it is a product of something more complex than a weak signal from one or more of the instruments. However, in the second day's data, the variance in the correlation coefficient of the two horizontal Dopbeams appears to be significantly higher than that of the vertical. It may be that wide fluctuations in data quality of the two horizontal Dopbeams caused turbulent dissipation rates calculated from those instruments to be significantly higher than dissipation calculated from the vertical signal. Further investigation is warranted.

6. Conclusions

This paper has presented the field-testing of three 1.72 MHz, pulse-to-pulse coherent acoustic Doppler profilers (Dopbeams). The strength of the Dopbeam as compared to conventional single point velocimeters is that Dopbeam can obtain simultaneous velocity measurements at a series of densely spaced locations and at a high sampling rate. Because Dopbeams velocity measurements are a function of both range and time, wavenumber spectra can be calculated directly. There is no need to invoke any form of Taylor's hypothesis. About half the time, wavenumber spectra exhibited an area of -5/3 constant spectral slope, indicating the presence of an inertial subrange. Once determined, the inertial subrange was used to estimate dissipation rate (□). A time series of □ values was then compared to CTD data to investigate the relationship between kinetic energy dissipation, salinity, temperature, and depth.

This study has confirmed Veron and Melville's conclusion (1999) that this instrument can measure wavenumber spectra, and can resolve an inertial

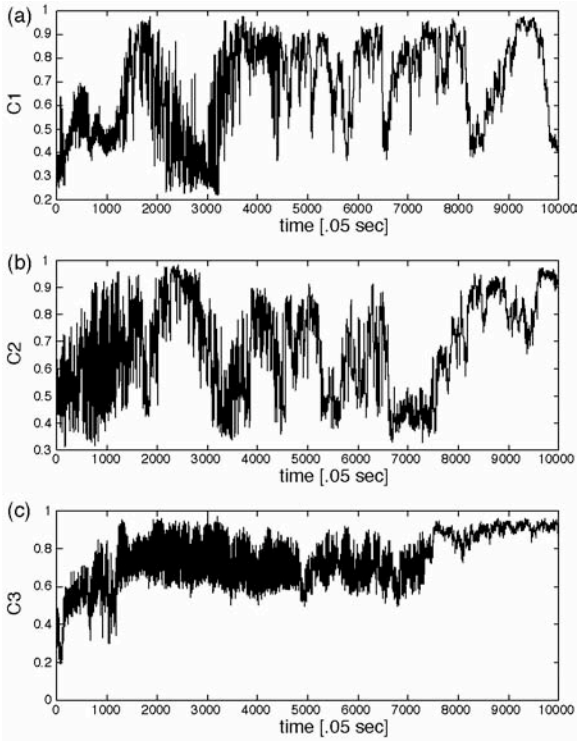

Figure 8. Time series of the correlation coefficients for the three Dopbeams for 500 seconds of data.

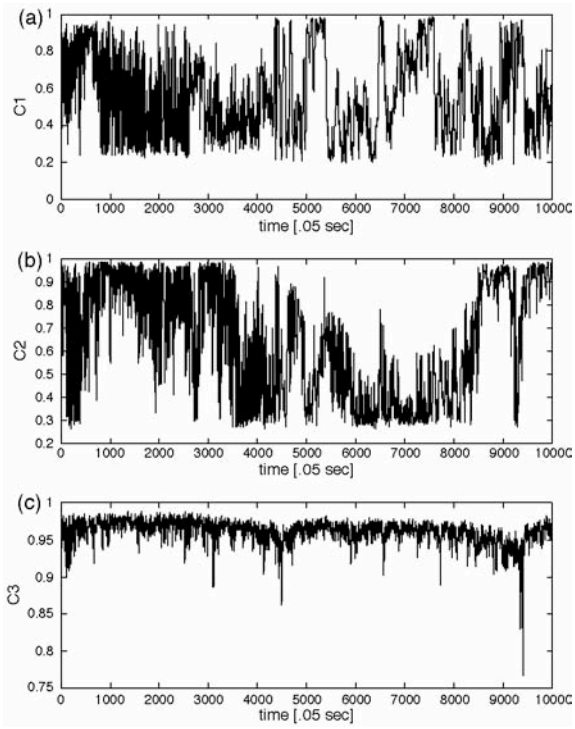

Figure 9. Time series of the correlation coefficients for the three Dopbeams for 500 seconds of data.

subrange in the range O(0.01m-1m).Further study is needed to determine whether any significant directionality is present in the turbulence of a well-mixed, near-surface layer, as well as what the relationship is between dissipation rate and depth.

We conclude that these instruments are effective at measuring turbulent wavenumber spectra in the near-surface layer of an estuarine environment.

Acknowledgments. I would like to thank Dr. Tetsu Hara for numerous enlightening discussions regarding turbulence, signal processing, fluid mechanics, and oceanographic study in general, as well as for giving me the opportunity to take part in this line of research. I would also like to extend special thanks to Dr. Rob Pockalny, the National Science Foundation, and the other organizers and underwriters of the SURFO program for making this research opportunity available to me, and to Qing Tao Song and Nick Scott for their technical support. Finally, I would like to thank Dr. Svein Vagle and staff at Institute of Ocean Sciences, Sidney, BC Canada, for providing the experimental data.

References

Agrawal, Y.C., E. A. Terray, M. A. Donelan, P.A. Hwang, A.J. Williams III, W. M. Drennan, K.K. Kahma, and S. A. Kitaigorodskii, 1992: Enhanced Dissipation of Kinetic energy beneath surface waves. *Nature*, **359**, 219-220.

Anis, A., and J.N. Moum, 1995:Surface wave-turbulence interactions: Scaling e(z) near the sea surface. *J. Phys. Oceanogr*., **25**, 346-366.

Craig, P. D. and M. L. Banner, 1994: Modeling wave-enhanced turbulence in the ocean surface layer. *J. Phys. Oceanogr*., **24**, 2546-2559.

Drennan, W.M., K.K. Kahma, E. A. Terray, M. A. Donelan, and S. A. Kitaigorodskii, 1992: Obervations of the enhancement of kinetic energy dissipation beneath breaking wind waves. *Breaking waves*: IUTAM *Symposium Sydney, Australia 1991,* M. L. Banner and R. H. L. Grimshaw, Eds., Springer-Verlag, 95-102.

Drennan, W.M., M. A. Donelan, E. A. Terray, and K. B. Katsaros, 1996: Oceanic turbulence dissipation measurements in SWADE. *J. Phys. Oceanogr*., **26**, 808-815.

Gargett, A. E., 1989: Ocean turbulence. *Annu. Rev.Fluid Mech.,* **21**, 419-451.

Hinze, J. O., 1975: *Turbulence*. McGraw-Hill, 790 pp.

McWilliams, J. C., P. P. Sullivan, and C.H. Moeng, 1997: Langmuir turbulence in the ocean. *J. Fluid Mech*. **334**, 1-30.

Melville, W. K., 1994: Energy dissipation by breaking waves. *J. Phys. Oceanogr*., **24**, 2041-2049.

Melville, W. K., R. Shear, and F. Veron, 1998: Laboratory measurements of the generation and evolution of Langmuir circulations. *J. Fluid Mech*., **364**, 31-58.

Skyllingstad, E. D. and D. W. Denbo, 1995: An ocean large-eddy simulation of Langmuir circulations and convection in the surface mixed layer. *J. Geophys. Res.*, **100**, 8501-8522.

Tennekes, H., and J.L. Lumley, 1972: *A First Course in Turbulence.* The MIT Press, 300 pp.

Terray, E. A., M. A. Donelan, Y. C. Agrawal, W. M. Drennan, K. K. Kahma, A. J. Williams III, P.A. Hwang, and S. A. Kitaigorodskii, 1996: Estimates of kinetic energy dissipation under breaking waves. *J. Phys. Oceanogr.*, **26**, 792-807.

Thorpe, S. A., 1993: Energy loss by breaking waves. *J. Phys. Oceanogr.*, **23**, 2498-2502.

Trowbridge, J., and S. Elgar, 2001: Turbulence measurements in the surf zone. Woods Hole Oceanographic Institution, Tech. Rep., WHOOI-2001-02, Woods Hole, MA, 14 pp.

Veron, F. and W. K. Melville, 1999: Pulse-to pulse coherent Doppler measurements of waves and turbulence. *J. Atmos. Oceanic Technol.,* **16**, 1580-1597.

Corresponding author address: Brian P. Sullivan and Tetsu Hara, Graduate School of Oceanography, Univeristy of Rhode Island, Narragansett, RI 02882. (sullivbp@westminster.edu, thara@gso.uri.edu)